2023

Artificial Intelligence Algorithms for Eye Banking

Ranit Karmakar
Michigan Technological University, rkarmaka@mtu.edu

ARTIFICIAL INTELLIGENCE ALGORITHMS FOR EYE BANKING

By

Ranit Karmakar

A DISSERTATION

Submitted in partial fulfillment of the requirements for the degree of

DOCTOR OF PHILOSOPHY

In Computer Engineering

MICHIGAN TECHNOLOGICAL UNIVERSITY

2023

This dissertation has been approved in partial fulfillment of the requirements for the Degree of DOCTOR OF PHILOSOPHY in Computer Engineering.

Department of Electrical and Computer Engineering

Dissertation Advisor:	*Dr. Sean J. Kirkpatrick*
Committee Member:	*Dr. Allen O. Eghrari*
Committee Member:	*Dr. Daniel R. Fuhrmann*
Committee Member:	*Dr. Glen E. Archer*
Department Chair:	*Dr. Jin W. Choi*

Dedication

This dissertation is dedicated to the most important people in my life: my family and friends. Without their love, support, and encouragement, I would not have been able to achieve this milestone.

To my parents, who instilled in me a love of learning and a sense of curiosity from a young age. Your sacrifices and unwavering belief in me have been the driving force behind my academic pursuits. Thank you for always being my biggest cheerleaders and for instilling in me the values of hard work, perseverance, and resilience.

To my brother, who have always been my closest ally and confidant. Your unwavering support and encouragement have helped me overcome countless obstacles and have made this journey more enjoyable. Your care and support for the family when I was thousands of miles away in the opposite side of the world let me focus on my education.

To my nephew, who have taught me the true meaning of determination and perseverance. Your love and enthusiasm for life have reminded me of the importance of staying grounded and focused on what truly matters.

To my extended family, my friends, who have always been there for me, offering their

support and encouragement. Your words of wisdom, comfort, and motivation have been instrumental in helping me overcome the challenges of this journey.

This dissertation is a testament to your love, support, and unwavering belief in me. I am forever grateful for your presence in my life and for the countless ways in which you have helped me become the person I am today. Thank you for always being my biggest supporters and for believing in me even when I didn't believe in myself. This accomplishment is as much yours as it is mine.

Contents

List of Figures

List of Tables

Author Contribution Statement

This dissertation was partially advised by Dr. Saeid V. Nooshabadi.

Acknowledgments

I would like to express my sincere gratitude to everyone who has supported me throughout my dissertation journey.

I would like to extend my heartfelt appreciation to my mentor, Dr. Allen Eghrari, for his support, encouragement, and guidance. His expertise, insights, and constructive feedback have been invaluable throughout the entire process, and I am deeply grateful for his mentorship.

I would also like to acknowledge and thank our collaborators, John Lohmeier and Staci Terrin from Rocky Mountain Lions Eye Bank, Florida; Elizabeth Fout and William Buras from Florida Lions Eye Bank, and Dr. Ellen Koo from University of Miami. Their contributions to this research have been instrumental in advancing my understanding of the subject matter. Their willingness to share their knowledge, expertise, and resources has been an inspiration to me, and I am grateful for the opportunity to have worked with such talented and dedicated individuals.

I would like to express my gratitude to my family and friends for their unwavering support, encouragement, and understanding throughout this journey. Their love, encouragement, and unwavering support have been a constant source of inspiration and motivation, and I am forever grateful for their presence in my life.

I would like to thank Michigan Tech and the Graduate School for providing me with the resources and support that made this research possible. The university's commitment to academic excellence has been instrumental in shaping my research interests and guiding my intellectual pursuits.

Lastly, I would like to thank everyone that I met along the way and who helped me by sharing their knowledge, experiences and resources with me that helped me to move forward with my research.

Thank you all from the bottom of my heart. This research would not have been possible without your support and encouragement, and I am deeply grateful for the role you have played in this journey.

Abstract

Eye banking plays a critical role in modern medicine by providing cornea tissues for transplantation to restore vision for millions of people worldwide. The evaluation of corneal endothelium is done by measuring the corneal endothelial cell density (ECD). Unfortunately, the current system to measure ECD is manual, time-consuming, and error-prone. Furthermore, the impact of social behaviors and biological conditions on corneal endothelium and corneal transplant success is largely unexplored. To overcome these challenges, this dissertation aims to develop tools for corneal endothelial image and data analysis that enhance the efficiency and quality of cornea transplants.

In the first study, an image processing algorithm is developed to analyze corneal endothelial images captured by a Konan CellChek specular microscope. The algorithm successfully identifies the region of interest, filters the image, and employs stochastic watershed segmentation to determine cell boundaries and evaluate endothelial cell density (ECD). The proposed algorithm achieves a high correlation with manual counts ($R^2 = 0.98$) and has an average analysis time of 2.5 seconds.

In the second study, a deep learning-based cell segmentation algorithm called Mobile-CellNet is proposed to estimate ECD. This technique addresses the limitations of classical algorithms and creates a more robust and highly efficient algorithm. The

approach achieves a mean absolute error of 4.06% for ECD on the test set, similar to U-Net but with significantly fewer floating-point operations and parameters.

The third study explores the correlation between alcohol abuse and corneal endothelial morphology in a donor pool of 5,624 individuals. Multivariable regression analysis shows that alcohol abuse is associated with a reduction in endothelial cell density, an increase in the coefficient of variation, and a decrease in percent hexagonality.

These studies highlight the potential of big data and artificial algorithms in accurately and efficiently analyzing corneal images and donor medical data to improve the efficiency of eye banking and patient outcomes. By automating the analysis of corneal images and exploring the impact of social behaviors and biological conditions on corneal endothelial morphology, we can enhance the quality and availability of cornea transplants and ultimately improve the lives of millions of people worldwide.

Chapter 1

Introduction

Artificial intelligence (AI) is being increasingly used in ophthalmology [3]. Recently Food and Drug Administration (FDA) [4] and National Eye Institute (NEI) [5] has also showed its interest and priority towards AI enabled devices and research. Similar applications also applies in eye banking to improve efficiency, accuracy, and speed in various aspects of the process [6, 7].

One way in which AI can be used in eye banking is to improve the accuracy and efficiency of tissue processing and preservation. For example, AI-based systems can analyze images of eye tissue to identify abnormalities or damage [8, 9, 10] that may affect its suitability for transplantation. This can help to ensure that only high-quality tissue is made available for transplantation, improving patient outcomes.

AI can also be used in research and development efforts in eye banking. For example, AI-based systems can analyze large amounts of data to identify patterns and trends that may help to advance our understanding of eye disease and the potential for new treatments and therapies [11, 12, 13].

In addition, AI can be used in the identification and selection of potential donors. Traditional methods [14] of identifying potential donors rely on manual review of medical records and corneal health, which can be time-consuming and prone to errors. AI-based systems can quickly and accurately analyze large amounts of data to identify potential donors who meet the eligibility criteria for eye donation.

AI can also be used to optimize the distribution of donated eye tissue to ensure that it reaches its destination as quickly and efficiently as possible. This includes the use of AI-based algorithms to predict demand and optimize the allocation of tissue to meet the needs of transplant surgeons and researchers.

Overall, the use of AI in eye banking can help to improve the efficiency, accuracy, and speed of various aspects of the process, from donor identification and tissue processing to distribution and research. It helps to ensure that donated eye tissue is used to its full potential to restore sight and improve the lives of those suffering from vision loss or blindness.

It is important to note that the use of AI in eye banking, as with any application of

AI [15, 16, 17], should be carefully regulated and monitored to ensure that it is used ethically and appropriately. This includes ensuring that AI systems are trained on diverse and representative data sets and that their outputs are subject to appropriate oversight and accountability.

In this research, we focused on analyzing a large amount of diverse data collected at two eye banks over five years to automate accurate analysis of corneal tissues and to identify the effects of social behaviors and medical conditions on the corneal endothelium.

1.1 Eye Banking

Eye banking in the United States is a vital part of the healthcare system, providing donated eye tissue for transplantation and research [14, 18]. The demand for donated eye tissue is high [19, 20], as there are many conditions that can result in vision loss or blindness, including glaucoma, cataracts, and age-related macular degeneration. Eye banking plays a critical role in helping to restore sight and improve the lives of those suffering from these conditions.

There are several organizations that operate eye banks in the United States, including

the Eye Bank Association of America (EBAA) and the National Eye Bank Association (NEBA). These organizations are responsible for coordinating the procurement, processing, and distribution of donated eye tissue.

The process of eye banking begins with the identification of potential donors. This includes individuals who have indicated their desire to donate their eyes upon their death and those who have died unexpectedly and may be suitable for donation. Once a potential donor has been identified, the eye bank works with the donor's family to obtain their consent for donation [14].

The next step in the process is the procurement of the donated eye tissue. This involves the removal of the eye tissue from the donor's body by trained professionals in a sterile environment. The tissue is then transported to the eye bank, where it is carefully processed and prepared for transplantation or research [14].

Once the eye tissue has been processed, it is made available for transplantation or research [14]. The EBAA and NEBA maintain a registry of available eye tissue and work with transplant surgeons and researchers to match the tissue with recipients or research projects.

Eye banking plays a critical role in the healthcare system, helping to restore sight and improve the lives of those suffering from vision loss or blindness. It is an important part of the organ donation process [21], and those who wish to donate their eyes upon

their death can do so by registering as organ donors and indicating their desire to donate their eyes.

In addition to providing donated eye tissue for transplantation, eye banking also plays a crucial role in advancing scientific research. Researchers use donated eye tissue to study the effects of various diseases and conditions on the eye, as well as to develop new treatments and therapies.

Despite the important role that eye banking plays in the healthcare system, there is still a significant shortage of donated eye tissue [19, 20]. This is often due to a lack of awareness about the importance of eye donation and the need for registered organ donors.

To address this shortage, eye banks and other organizations are working to increase awareness about the importance of eye donation and the need for registered organ donors. This includes educational campaigns, partnerships with healthcare providers, and efforts to increase the number of registered organ donors.

In conclusion, eye banking in the United States is a vital part of the healthcare system, providing donated eye tissue for transplantation and research. It plays a critical role in helping to restore sight and improve the lives of those suffering from vision loss or blindness. While there is still a shortage of donated eye tissue, efforts are underway to increase awareness about the importance of eye donation and the need for registered

organ donors.

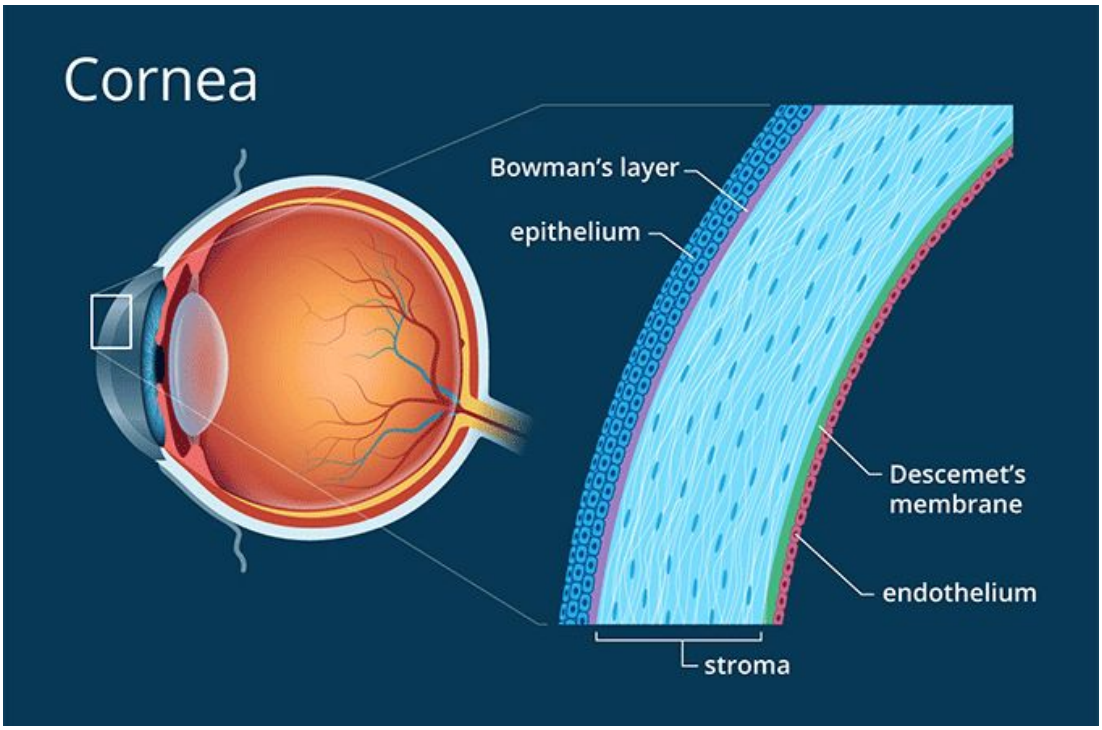

Figure 1.1: Anatomy of the human eye, position of the cornea, and different layers of the human cornea. [source: https://www.allaboutvision.com/resources/cornea.htm]

1.2 Corneal Endothelium

The corneal endothelium is a single layer of cells that lines the inner surface of the cornea, the clear, outermost layer of the eye (Figure 1.1). Located at the back of the cornea, the endothelium is responsible for maintaining the cornea's transparency and clarity by pumping excess fluid out of the cornea and regulating the exchange of nutrients and waste products between the cornea and the surrounding tissues [22].

The corneal endothelium is made up of hexagonal-shaped cells called endothelial cells, which are connected by tight junctions and are surrounded by a basement membrane. These cells are essential for maintaining the cornea's transparency because they are responsible for removing excess fluid from the cornea. They do this by actively pumping sodium and chloride ions out of the cornea and into the surrounding tissues, which helps to regulate the cornea's hydration level.

The corneal endothelium is also important for regulating the exchange of nutrients and waste products between the cornea and the surrounding tissues. It does this by transporting small molecules such as glucose and amino acids from the surrounding tissues into the cornea, and by transporting waste products such as lactic acid and carbon dioxide out of the cornea.

One of the most important functions of the corneal endothelium is to maintain the cornea's transparency. This is because the cornea is a highly avascular tissue, meaning it does not have its own blood supply. Instead, it relies on the diffusion of nutrients and waste products from the surrounding tissues to maintain its health and function. If the corneal endothelium is damaged or diseased, it can result in a loss of transparency and clarity, leading to vision problems.

There are several conditions that can affect the corneal endothelium and lead to a loss of transparency and clarity [23, 24]. One of the most common is Fuchs' endothelial dystrophy [25, 26], a genetic condition that results in the gradual loss of endothelial

cells over time. This can lead to corneal edema, or swelling, which can cause vision problems. Other conditions that can affect the corneal endothelium include corneal endothelial degeneration, which is often associated with aging, and corneal endothelial trauma, which can be caused by injury or surgery [24].

In cases where the corneal endothelium is damaged or diseased, treatment may be necessary to restore transparency and clarity to the cornea. One treatment option is a corneal transplant [27, 28], also known as a keratoplasty, in which the damaged cornea is replaced with a healthy donor cornea. Another option is a procedure called Descemet's stripping automated endothelial keratoplasty (DSAEK) [29], in which only the damaged endothelial layer is replaced with a healthy donor endothelial layer [30].

In conclusion, the corneal endothelium is a vital layer of cells that lines the inner surface of the cornea and plays a crucial role in maintaining the cornea's transparency and clarity. It is responsible for pumping excess fluid out of the cornea and regulating the exchange of nutrients and waste products between the cornea and the surrounding tissues. If the corneal endothelium is damaged or diseased, it can lead to vision problems, and treatment may be necessary to restore transparency and clarity to the cornea.

1.3 Literature

1.3.1 Endothelial image analysis

Counting the cell density of the corneal endothelium is an important task in ophthalmology for the diagnosis and monitoring of corneal diseases [31, 32]. Several algorithms have been proposed in the literature for this purpose, each with its own advantages and limitations.

One of the earliest algorithms proposed for cell counting was the manual counting method, where a researcher manually counts the number of cells in a selected area of the corneal endothelial image [33, 34]. This method is considered to be the gold standard but is time-consuming and subject to observer variability. Three main techniques of measuring corneal endothelial cell density are corner method, cell-center method and flex-center method [35, 36].

Automatic cell counting algorithms have been proposed as an alternative to manual counting. These algorithms can be divided into two main categories: classical image processing algorithms and AI-based algorithms.

Classical image processing based algorithms can further be categorized into

thresholding-based algorithms, morphology-based algorithms, and frequency domain-based algorithms. In recent times we see more machine learning based algorithms which uses feature extraction and machine learning classifier models as well as deep learning models such as neural networks.

1.3.1.1 Classical image processing algorithms

One of the very first methods proposed for automatic analysis of the corneal endothelial images was published in 1992 by Vincent et.al [37]. In this paper, the authors have used a morphological dome extractor with watershed algorithm.

The use of morphological image processing is extremely common in corneal endothelial image analysis. In [38], Fabijańska et.al proposed a method that uses neural network along with morphological image processing. In [39], Selig et.al. used stochastic watershed and combined it with skeletonization. Similar use of watershed was proposed by Charłampowicz et al. [40] and Dagher et. al. [41] as well.

In 2002, Forracchia et.al. [42] proposed a Discrete Fourier Transform (DFT) based algorithm. Authors showed that the spatial frequency analysis using 2D DFT creates a ring. The size of the ring changes with different images and it is directly correlated with the cell density. Other frequency based algorithms uses DFT methods to determine the cell size and estimate the parameters for the spatial filters. In another set

of papers [43] [44], authors have proposed statistical models using the cell shape as *a priori* information.

Some other methods proposed for the analysis of the corneal endothelial images include level-set method proposed by Zhuo et.al. [45], skeletonization and watershed based algorithm by Gavet et.al. [46], binarization and thresholding by Piorkowski et.al. [47], and genetic algorithm by Scarapa et.al. [48].

One of the main limitations of these classical image processing based methods is the lack of robustness. Hence, in recent times, we have seen the use of AI in corneal endothelial image analysis.

1.3.1.2 Artifical Intelligence algorithms

In recent times, different AI-based algorithm are proposed in the literature. AI-based algorithms include both convolution neural networks (CNN) and feature based machine learning algorithms.

One of the very first CNN-based algorithm was proposed by Salerno et.al. in 1998 [49]. Later more sophisticated algorithms using neural network and morphology [38], pre-trained AlexNet [50], and U-Net[51] were proposed. In [38], authors have used U-Net to create the initial edge probability map. This map was later binarized and

skeletonized to create a single pixel thick cell border. Kolluru et.al [51], used U-Net and SegNet [52] both to segment the corneal endothelial images. Their comparison over 130 images showed that U-Net performed better compared to SegNet. In another paper, [53] authors have proposed a dense U-Net where a first network was trained to detect the edges. Later the edge map was used to train another network to detect the region of interest. Later, these two maps were combined and post-processed to create the final segmentation.

While these networks produce significantly better results compared to the classical methods, a major critique of them is that these networks were trained with a handful of good quality images. Hence, in [54], authors have used U-Net on 'real-world' corneal endohtelial images. In another work [55], authors have trained a U-Net with a set of images affected by guttata. Another work in [56] used U-Net along with watershed for the segmentation of the corneal endothelium in the patients with Fuchs dystrophy.

Authors have also proposed machine learning algorithms that uses features extractors along with K-means [57].

1.3.2 Data analysis

Multiple studies have been performed on analyzing the effects of diabetes mellitus on corneal endothelial thickness and cell density. One of the very first analysis was performed by Schultz et.al. in 1986 [58] where authors have used 46 corneas from 25 patients with type II diabetes. After analyzing, authors have found that there was no noticable difference in cell density, however, the coefficient of variance and hexagonality were significantly different. Other works [59, 60], however, have contradicted the findings. They have concluded that the corneal endothelial cell density decreases and corneal thickness increases for patients with diabetes mellitus.

Similar works [61, 62] were also done on tobacco usage and corneal endothelial health. In both the studies, findings were inconclusive. In our work, we focused on alcohol consumption with adjusting for tobacco usage and its effects on corneal endothelial health.

1.4 Chapter outline

Chapter 2: In this chapter, we propose a classical image processing based algorithm for corneal endothelial image analysis. We use a large dataset of 303 images pictured

using a Konan CellCheck specular microscope at clinical settings. We use edge detection and morphological image processing to first segment the cells and then count the number of cells to determine the density. The proposed algorithm is compared against the manual analysis and automatic analysis by AutoTracer.

Chapter 3: In this chapter, we propose an efficient deep learning-based algorithm to analyze corneal endothelial images. We use inverse residual blocks on the U-Net backbone to develop our network. We use two parallel networks along with some image post-processing to determine our final segmentation.

Chapter 4: In this chapter, we evaluate the effects of alcohol consumption on the human corneal endothelium. We evaluate 10,322 images from 5624 donors to understand the correlation between alcohol consumption and corneal endothelial cell density. We develop a multivariate regression model and use age, sex, tobacco use, history of cataract and diabetes mellitus along with alcohol consumption.

Final chapter: This chapter summarizes the work presented in this dissertation, addresses the limitations and discusses future scope of work.

Chapter 2

An Automatic Approach for Cell Detection and Segmentation of Corneal Endothelium Using Specular Microscope

Authors: *Ranit Karmakar, Saeid Nooshabadi, Allen Eghrari* [1]

[1]Karmakar, R., Nooshabadi, S. and Eghrari, A., 2022. An automatic approach for cell detection and segmentation of corneal endothelium in specular microscope. Graefe's Archive for Clinical and Experimental Ophthalmology, 260(4), pp.1215-1224.

2.1 Abstract

2.1.1 Purpose

Specular microscopy is an indispensable tool for clinicians seeking to monitor the corneal endothelium. Automated methods of determining endothelial cell density (ECD) are limited in their ability to analyze images of poor quality. We describe and assess an image processing algorithm to analyze corneal endothelial images.

2.1.2 Methods

A set of corneal endothelial images acquired with a Konan CellChek specular microscope was analyzed using three methods: flex-center, Konan Auto Tracer, and the proposed method. In this technique, the algorithm determines the region of interest, filters the image to differentiate cell boundaries from their interiors, and utilizes stochastic watershed segmentation to draw cell boundaries and assess ECD based on the masked region. We compared ECD measured by the algorithm with manual and automated results from the specular microscope.

2.1.3 Results

We analyzed a total of 303 images manually, using the Auto Tracer, and with the proposed image processing method. Relative to manual analysis across all images, the mean error was 0.04% in the proposed method ($p = 0.23$ for difference) whereas Auto Tracer demonstrated a bias towards overestimation, with a mean error of 5.7% ($p = 2.0610^{-8}$). The relative mean absolute errors were 6.9% and 7.8%, respectively, for the proposed and Auto Tracer. The average time for analysis of each image using the proposed method was 2.5 s.

2.1.4 Conclusion

We demonstrate a computationally efficient algorithm to analyze corneal endothelial cell density that can be implemented on devices for clinical and research use.

2.2 Introduction

The corneal endothelium is a cellular monolayer with predominantly hexagonal morphology. During the human lifespan, endothelial cell density (ECD) begins with its

highest values at approximately 3500 to 4000 cells/mm^2 [63]. The ECD reduces with the natural process of aging over time [64] to approximately 2000 cells/mm^2 at older age, resulting in an increase in cell size [65]. Hereditary diseases, trauma, infection or surgical procedures can also contribute to a decrease in ECD [66]

Cell density is only one metric of overall corneal health; polymegethism and pleomorphism are two other important factors that reflect the well-being of the corneal endothelium,[66] [67] features that are affected by cell size and shape, respectively.

To capture and analyze these features of the corneal endothelium, confocal and specular microscopy are both widely used by clinicians and researchers. Specular microscopy, introduced by Maurice [68] in 1968, has improved across multiple iterations [69] [70] and is widely used across the globe for endothelial imaging in clinical settings. While contact-based confocal imaging with a coupling gel is advantageous in image quality [33, 71, 72], especially in the setting of corneal edema, specular microscopy is more frequently utilized in clinical settings because of its fast and non-contact nature [73].

The Konan CellChek microscope is designed for specular imaging in clinical settings and includes software that can analyze captured images with either automatic, semi-automatic or manual techniques. Data from multiple studies suggest that automatic

analyses produce significantly different results from manual analyses [33, 74, 75], leading many clinicians to use manual counts, although under certain circumstances, the results may be comparable [36]. Manual cell count, however, is a time-consuming procedure as a technician needs to go through each cell and mark its border and/or centers before the software can scan the marked image to obtain cell count and morphology. Moreover, manual techniques introduce bias, and based on the number of counted cells, different technicians may produce significantly different results. [76] These shortcomings provide a motivation for the development of a fully automatic technique to perform endothelial cell analysis.

Historically, while several algorithms for automatic segmentation and cell count of endothelial images have been proposed to date [37, 49], most work relies on small datasets that do not necessarily correspond to images from a real clinical setting, using images instead from eye banks [42, 44, 77] or from deceased animals [57, 78], that are pre-processed for better imaging.

More recent approaches include frequency domain analysis [39, 42]. Discrete Fourier Transform (DFT) is a widely used technique for cell size determination as well as parameter estimation for spatial filters. The DFT of an endothelial image produces a circular ring pattern around the center. The size and shape of this ring varies with the cell shape and density [79]. This information can be used to estimate ECD.

Other techniques involve K-means based image segmentation [57], genetic programming [80] and single cell model descriptor [44]. In recent past, we have observed the introduction of artificial neural network-based techniques [51, 53, 54, 81, 82, 83] , with U-net and Seg-Net models for cell segmentation being most widely used for biomedical imaging applications. Although the current neural network algorithms seem to work fairly well on the test images, the smaller size of the dataset makes them less suitable for deep learning models, as it may introduce bias in the network. Most reported techniques for cell count involve morphological operations [38, 77, 84, 85, 86]. Generally these techniques are divided into two steps. In the first step, endothelial images are segmented and a skeleton type structure is formed from the main image. In the second step, these skeleton structures are used to extract morphological information of the cells.

The existing techniques, unfortunately, cannot produce consistent results across a range of clinical settings where the quality of the acquired images is compromised. In typical clinical settings, the image quality varies widely due to uneven illumination, and movement of the patient. Further, the presence of Fuchs endothelial corneal dystrophy (FECD) creates dark cavities in the image. In most algorithms, these images are excluded from the dataset, or the dataset is manually preprocessed to demark the areas affected with disease, or uneven illumination [54]. In this work we propose an automatic exclusion of such areas, as the first step of an algorithm through a process of region of interest (RoI) demarcation.

In this paper, we propose an automatic technique to accurately determine cell density of the corneal endothelium. The technique uses the image information to detect the regions that are affected by uneven illumination and the FECD dark cavities in an image for exclusion from filtering and segmentation. We also use a dataset of 100 images with varying quality to validate the robustness of the proposed algorithm.

2.3 Methods and Materials

2.3.1 Materials

The images used in this study were collected during a previous study of specular microscopy using the Konan CellChek specular microscope, approved by the Institutional Research Board at the Johns Hopkins University School of Medicine. Informed consent was obtained from all participants and data were deidentifed at the time of initial collection.

The dataset contained a total of 303 images of fairly healthy eyes from 162 patients with 124 females and 38 males. We only selected images with more than 2000 cells as cell density and where a manual grader was able to count 30 contiguous cells. No images in this study were acquired from eyes that had previously undergone keratoplasty. The age and sex distribution of the patients are illustrated in Figure 2.1,

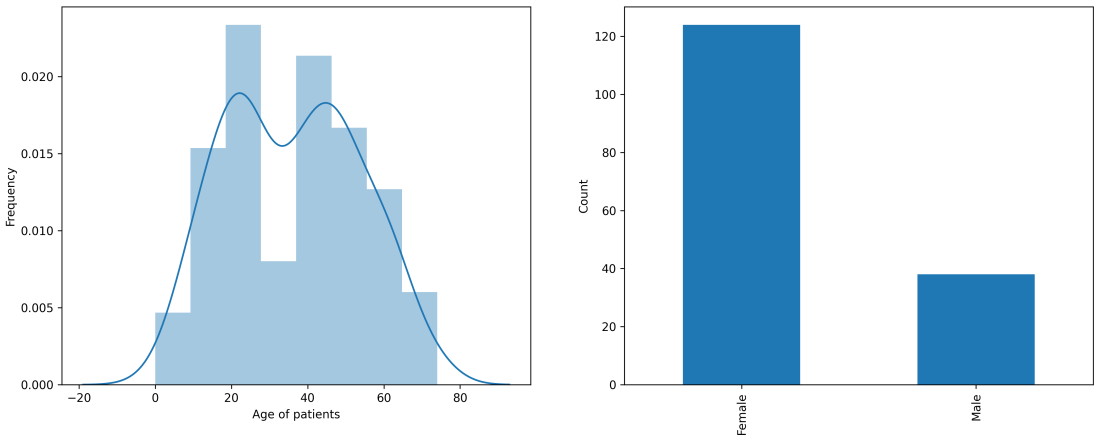

Figure 2.1: (From left) patients age distribution, and sex distribution

suggesting a normal distribution across all age groups with a mean of 36 years of age, and mode in the 40- to 50-year age group. Images were captured from both left and right eyes. In no case were two images from the same eye used in the analysis.

These images had been analyzed using the Konan CellChek software using the flex-center method. Each image had a dimension of 304×446 gray-color pixels, a standard output image dimension from CellChek. Graders employed a computer mouse to draw cell borders and cell centers on the captured images. We then repeated analyses with the CellChek Auto Tracer, to detect cell boundaries and calculate cell density using the commonly utilized automated method.

For the algorithm described below, we used MATLAB 2018b running on an Intel 2 GHz hexa-core CPU with an NVIDIA 1060Ti GPU. The per image processing time of 2.5 s was obtained by averaging over time to process 303 images.

2.3.2 Methods

To address variability of illumination and the presence of diseases such as FECD in the acquired image, we divided the development of the algorithm into three steps.

† **Region of interest demarcation:** First, the region of interest (RoI) is demarcated to remove the unwanted bright areas or dark patches on the image. This step also masks out the areas affected by FECD.

† **Cell border detection:** Second, the RoI is filtered to differentiate the cells boundaries from their interiors.

† **Cell count:**Third, stochastic watershed segmentation is utilized to draw cell boundaries and count cell density based on the masked region.

Figure 2.2 illustrates the outputs from blocks that represent the steps described, along with the final result. We use classical image filtering techniques along with morphological image processing tools to filter the image and obtain the cell boundaries. Later, we use the *a priori* criteria about the cell shape and size to filter out the over and under-segmented cells that do not match the criteria.

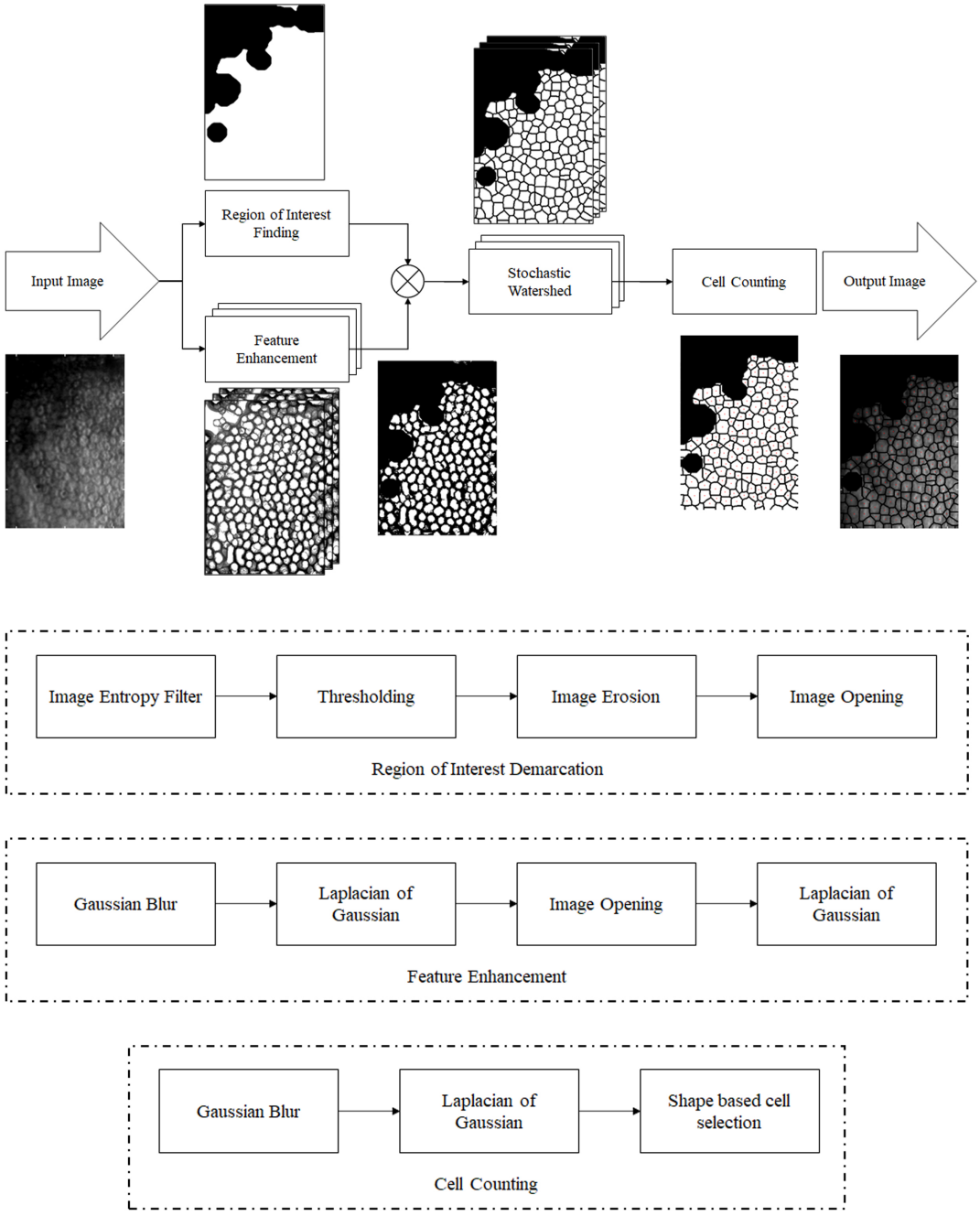

Figure 2.2: Proposed algorithm block diagram

2.3.2.1 Region of Interest Demarcation

The input image is passed through a local entropy filter to detect abnormalities. Entropy, defned by the Shannon's Entropy [87], is a statistical measure of randomness, and is represented as,

$$H = -\sum_{i=1}^{n} p_i log p_i \tag{2.1}$$

where n (= 256) is the number of gray levels and p_i is the probability associated with each gray level.

The entropy folter processes the image such that each output pixel contains the entropy value of a neighborhood window size of I × I (I = 9), around the corresponding pixel in the input image. If a section of the image is too bright or dark that no edge information could be obtained from that neighborhood, the value returned by the entropy filter is very low. In the constructed entropy map of an image, the affected areas look much darker than their nearby regions. We next threshold the image based on the entropy values to obtain a binary mask. The threshold value is chosen to be around 25% of the maximum entropy value. Masked out regions, unfortunately, do not fully cover the affected areas of the image and leaves some spurious links and small noise speckles on the image. Hence, we apply an image erosion operation first, and then follow it by an image opening. Image opening [88] is a morphological operation

that applies dilation over the eroded image.

$$(A \ominus B) \oplus B \tag{2.2}$$

Here A is the input image, and B is the structuring element. The operators $\ominus$ and $\oplus$, respectively, are the erosion and dilation.

The opening morphological operations create a mask with a wider area that completely masks out the unevenly illuminated areas of the image. The binary mask is then used with the main input image to mark RoI.

2.3.2.2 Feature enhancement

The feature enhancement block processes the image with different spatial domain filtering to detect the cell boundaries. The cell boundaries are generally darker than the cell interior, so edge detection techniques result in demarcation of the cell boundaries. However, due to poor image quality and illumination effects, direct application of normal edge detection techniques results in random edges that do not correspond to any cell boundaries. This causes cell oversegmentation. To reduce this problem, we apply the following filtering steps multiple times.

† **Gaussian blur:** We apply Gaussian blur to remove, from the input image, random spatial noise with a set standard deviation of σ

† **Laplacian of Gaussian edge detector:** Next the image is processed with Laplacian of Gaussian (LoG) [89] edge detector. As Laplacian is a second derivative operator, LoG filter works better in detecting cell boundaries than any first order derivative-based edge detectors like Sobel [89] or Canny [90].

† **Morphological operations:** We then apply morphological opening on the output of the edge detector. Because of uneven illumination, the cell borders are not always prominent. Thus, the edge detector does not always detect the cell borders clearly. Erosion helps in breaking small links between cells. To restore the cell size, reduced due to erosion, we perform a dilation operation with the same structuring element.

† **Cell count:** After the image opening, we again apply LoG filtering one more time to detect the cell boundaries in a more prominent manner.

We repeat these steps N number of times with increasing values of standard deviation of the Gaussian kernel, σ. These N filtered images are then averaged to produce the final output. In this work, we have chosen to be in the range between 0.25 and 10 at regular interval of 0.25 (N = 40). Figure 2.2 presents the output after the feature enhancement step.

Finally, we apply stochastic watershed segmentation on the image. Before performing this operation, we blur the image using Gaussian kernel with standard deviation σ, in the range between 0.25 and 11 in 25 equal steps. The binary outputs from all blurred images are then averaged to obtain the final cell borders.

2.3.2.3 Cell counting:

All the cells segmented and detected by the filtering process cannot be included in the cell density estimation. As corneal endothelial cells are predominantly hexagonal in shape [22, 89, 90], we only include the cells that meet this shape criterion in the cell density count. Symmetry in the hexagonal shape can be used in the circularity test of the cells to separate it from other shapes.

The circularity of an object is defined as,

$$C = \frac{4\pi A}{P^2} \tag{2.3}$$

where A is the area and P is the perimeter of the object. Based on this, the circularity of an ideal hexagon is 0.907. We only select cells with circularity estimates closer to this value. All other cells are rejected because they are highly likely to be result of over-segmentation than representation of a true cell. Empirically, we found that most of the cells can fall under the circularity threshold value of 0.75 and 1.6. Everything

outside this range is either under-segmented merged cells or over-segmented micro segments and they can be rejected. Furthermore, our observations show that the cell size variability itself is limited, allowing us to remove outliers from our observation. Using these two priors, we set a threshold that only includes the cells that satisfy these two criteria in the cell count.

2.3.3 Statistical analysis

Correlation coefficients were calculated between manual and automated methods of measurement of ECD. Paired *t-test* was conducted between the distribution ECD from manual count, and Auto Tracer and the proposed algorithm to determine the error performance of both techniques.

2.4 Results

Figure 2.3 demonstrates the cell segmentation and marking produced by the manually counted flex-center technique, Auto Tracer, and our proposed technique, using a typical image produced by the specular microscope. In this image, the left side is darker and no cellular information can be extracted. As a result, the Auto Tracer performed segmentation over the whole image, resulting in a higher cell count, and

affecting its measurements of cell morphology. The proposed technique masks these darker regions, allowing for ECD counts comparable to manual counts.

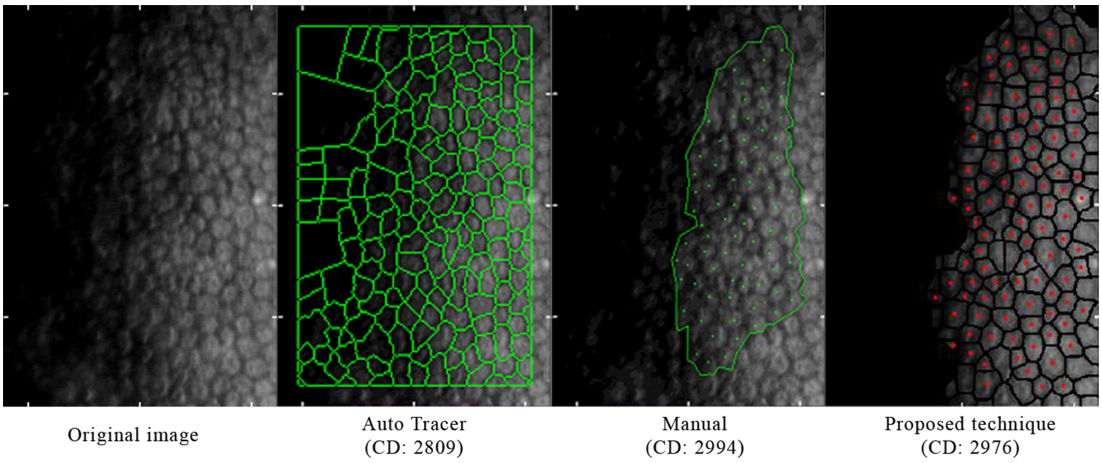

Figure 2.3: Segmentation results produced by the Auto Tracer, manual technique with flex-center, and the proposed technique, with their corresponding cell densities (CD)

The ECD values for the images counted manually ranged between 2004 and 3623 cells/mm^2, with a mean of 2706 cells/mm^2. The average manual cell count by technicians was 117 per image for these images, whereas our algorithm and Auto Tracer counted 167 and 151 cells respectively.

All images were also analyzed automatically by Auto Tracer, where the count ranged between 2392 and 3378 cells/mm^2, with a mean of 2834 cells/mm^2. Across the range of cell density values, Auto Tracer exhibits an overestimation bias relative to the manual counts by 5.7% on average ($p - value = 2.1 \times 10^{-8}$, paired t test for difference). The percentage mean absolute error (MAE) was 7.8% with a Pearson correlation coefficient (R^2) value of 0.85.

Figure 2.4 presents test results from an image using the proposed algorithm. Using this technique, the ECD values ranged from 2186 to 3754 cells/mm^2, with mean of 2679. Bias was minimal and is appreciated in the Bland-Altman Plot in Figure 2.6, an average of 0.04% of the manual cell count ($p - value = 0.24$, paired *t-test* for difference). The percentage MAE was 6.95% with a standard deviation of 9.14%. The R^2 value was 0.75 (Figure 2.5).

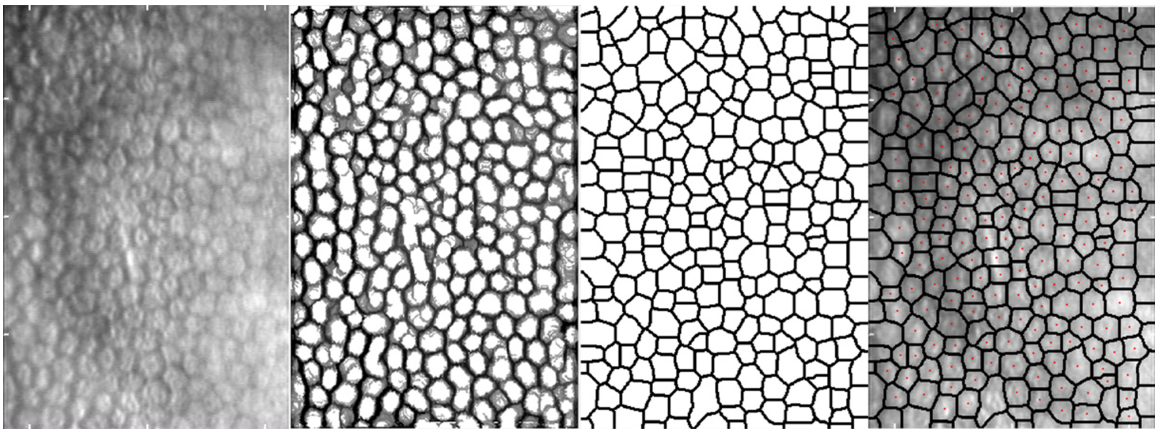

Figure 2.4: (From left) input image, feature-enhanced output, watershed segmented output, final segmented cells

While a difference existed in accuracy between groups, precision was comparable, with an MAE of 196 cells/mm^2 with the Auto Tracer technique versus 186 cells/mm^2 for the proposed algorithm.

We also evaluated the coefficient of variance (CV) and hexagonality (HEX) for all images. Compared to the manual technique across all images, the algorithm produced a median absolute error of 10.0% and 15.15% for the CV and HEX, respectively, while for Auto Tracer, these values were 17.14% and 20.00% respectively. For the Auto

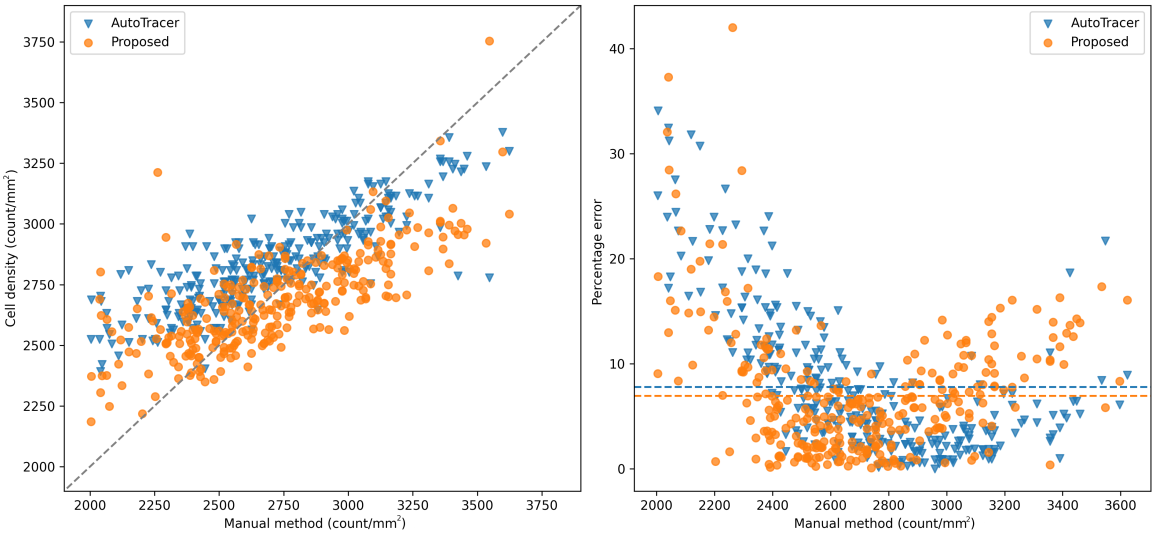

Figure 2.5: (Left) Scatter-plot comparison between the cell count density obtained from the proposed technique and CellCheck Auto Tracer with respect to the cell manual method. (Right) Scatter-plot of the percentage error values for the proposed technique and CellCheck Auto Tracer with respect to the manual count e proposed technique, with their corresponding cell densities (CD)

Figure 2.6: Bland-Altman plot comparing proposed algorithm and Auto Tracer

Tracer, we observed that the error was significantly higher than the proposed method for both CV ($p - value = 8.15 \times 10^{-22}$) and HEX ($p - value = 3.51 \times 10^{-71}$). We observed that the mean absolute error was high because of a few images producing high error values for HEX and CV. These images were poor in image quality.

The average processing time for the analysis of each image was 2.5 secs.

2.5 Discussion

In this study, we describe a proposed algorithm for analysis of specular microscopy images that are computationally efficient and demonstrate its ability to determine corneal ECD with a high degree of accuracy relative to manual counts using the flex-center method.

In clinical settings, technicians capturing images with specular microscopy often face a choice between efficiency and accuracy. The automated endothelial cell analysis provided by device manufacturers allows for rapid assessment of an image, but as described in this study, are prone to error when image quality is not ideal. The manual, flex-center approach optimizes the assessment of corneal endothelial health, but implementation demands huge time and human resources, as it requires an adequate number of cells to be identified in order to minimize error. The proposed algorithm

seeks to offer an approach that is both efficient and accurate.

We have compared the performance of this work with the set of state-of-the-art techniques in Table 2.1. Due to the absence of a publicly available dataset, we could not benchmark our algorithm on other datasets. However, Table 2.1 mentions the dataset used in the algorithm development for fair comparison. In performing this study, we have sought to build a robust algorithm by utilizing specular microscopy images acquired in a clinical setting, where the imaging quality may be limited, and there is a need to assess ECD with a relatively large set of data. We achieve an accuracy of 6.95% using 303 images. As a comparison, one technique that assessed confocal images in the clinical setting achieved an accuracy within 5% using 11 images [86]. Another study of 130 specular microscopy images from post-transplant corneas reports segmentation, but not the ECD [51].

A deep learning method was proposed in [53] where an MAE of 2.5% is reported. Although the performance of their algorithm was better for CV and HEX parameters, the method proposed here demonstrated a superior ability to determine ECD, the parameter most often sought by clinicians. Furthermore, the main problem with a typical deep learning method is data bias. Algorithms trained with a certain dataset do not always provide sufficient accuracy with a different dataset. The method proposed here does not rely on the training on any particular dataset and therefore would be free from data bias.

Table 2.1
Comparison of results between proposed algorithm and state-of-the-art methods

Approach	**Material**	**Dataset size**	**Mean absolute error**
U-Net	UT-DSAEK surgery patients	383	2.5%
U-Net	Specular images of the donor cornea	130	—
Neural net and morphology	Specular images from healthy diseased patients	30	6.78%
K-means and watershed	Porcine corneal tissue using Alizarine red dye	30	3.2%
Snake and particle swarm	Specular and confocal images from patients	11	5%
Cellular lattice	Inverse phase contrast microscope from deceased patients	21	5%
CellCheck Auto	Specular images from clinical patients	303	7.80%
Proposed algorithm (morphology)	Specular images from clinical patients	303	6.95%

In this study, analysis of each image required approximately 2.5 s, for the platform described in the "Methods and material" section. However, speed is dependent on both the complexity of the algorithm and the computing power of the imaging apparatus. Deployment for clinical use will require further experimentation with various algorithms and imaging apparatuses.

While this study demonstrates a technique that can identify ECD in specular microscopy images with opacities, a limitation is that it does not compare its ability to determine ECD in the setting of specific pathologies, such as Fuchs dystrophy or endothelial pigment. Future studies may be able to ascertain how well ECD can be

assessed in each of these settings. Additionally, all images in this study were acquired from a single specular microscope; future studies may be able to assess the extent to which this technique is valid across microscopes from various manufacturers.

In conclusion, we offer a method to estimate ECD in specular microscopy images with opacities of varying illumination and evidence of strong correlation with manual analysis.

Chapter 3

Mobile-CellNet: Automatic Segmentation of Corneal Endothelium Using an Efficient Hybrid Deep Learning Model

Authors: *Ranit Karmakar, Saeid Nooshabadi, Allen Eghrari* [1]

[1]Karmakar, R., Nooshabadi, S.V. and Eghrari, A.O., 2022. Mobile-CellNet: Automatic Segmentation of Corneal Endothelium Using an Efficient Hybrid Deep Learning Model. Cornea, pp.10-1097.

3.1 Abstract

3.1.1 Purpose

The corneal endothelium, the innermost layer of the human cornea, exhibits a morphology of predominantly hexagonal cells. These endothelial cells are believed to have limited regeneration capacity, and their density decreases over time. Endothelial cell density (ECD) can therefore be used to measure the health of the corneal endothelium and the overall cornea. In clinical settings, specular microscopes are used to image this layer. Owing to the unavailability of reliable automatic tools, technicians often manually mark the cell centers and borders to measure ECD for such images, a process that is time and resource-consuming.

3.1.2 Methods

In this article, we propose Mobile-CellNet, a novel completely automatic, efficient deep learning–based cell segmentation algorithm to estimate ECD. This uses two similar image segmentation models working in parallel along with image postprocessing using classical image processing techniques. We also compare the proposed algorithm with widely used biomedical image segmentation networks U-Net and U-Net++.

3.1.3 Results

The proposed technique achieved a mean absolute error of 4.06% for the ECD on the test set, comparable with the error for U-Net of 3.80% ($p - value = 0.185$ for difference), but requiring almost 31 times fewer floating-point operations (FLOPs) and 34 times fewer parameters.

3.1.4 Conclusion

Mobile-CellNet accurately segments corneal endothelial cells and reports ECD and cell morphology efficiently. This can be used to develop tools to analyze specular corneal endothelial images in remote settings.

3.2 Introduction

The cornea is the transparent, avascular outer layer of the human eye that works as a windshield to protect the inner contents of the eye and to transmit light [91]. It consists of five layers: epithelium, Bowman's layer, stroma, Descemet's membrane, and endothelium. The innermost layer of the cornea, the corneal endothelium, is

approximately 5.0 microns thick with predominantly hexagonal cells [92]. Cells in the endothelial layer are not thought to regenerate, and so with the death of one cell, neighbouring cells expand in size to take its place. This is a common process and over time the cell density of the endothelium layer decreases [64]. For a newborn child, the cell density is around $5000 - 6000$ cells/mm^2 while for an adult the cell density may drop to 2000 cells/mm^2 [65]. The presence of diseases, trauma, or medical surgery may rapidly decrease cell density [66]. The corneal endothelium maintains stromal hydration [93]. Lower endothelial cell density (ECD) or diseases such as Fuchs dystrophy cause stromal edema and reduce corneal transparency [94]. Hence, clinicians use ECD as one measure of overall corneal health. Along with ECD, polymegethism, the variation in cell size, is measured by coefficient of variance (CV), and polymorphism, the variation of cell shape, is measured by hexagonality (HEX).

In clinical settings, specular microscopes are used to take detailed pictures of the corneal endothelium. These pictures are then analyzed by trained technicians to measure ECD, CV and HEX. The techniques used in clinical settings for analyzing corneal endothelium can be divided into three categories, 1) fully automatic where technicians use vendor provided software for the cell count estimation; 2) semi-automatic where the technician inputs the size of an average cell for the analysis by a software; 3) manual where the technicians manually mark the area and cell centers for the software. Manual methods can also be sub-divided into center method, flex-center method, and

corner method. While no significant difference is found between the manual methods [35], automatic methods fail to produce consistent accurate segmentation [33]. Hence, manual methods (center and flex-center) are the most accepted practices in clinical settings. However, due to time and resource constraints, automatic methods are frequently used which leads to inaccurate measurements.

To address this problem, different techniques to automate the process have been proposed. Most techniques to date are based on the classical image processing, such as frequency domain analysis [42] [79] [39] and morphological analysis [1] [38] [86] [85] [77] [84]. However, recent works focused on machine and deep learning techniques. Deep learning methods [53] [54] [51] [82] [83] have reported better results. These techniques suffer from the complication of the need for the availability of suitable data for the training, and need for deployment of fast processor hardware, thereby limiting their use in clinical settings. Additionally, there is a challenge in the evaluation deep learning techniques due to lack of publicly available, labelled datasets.

In this paper, we propose Mobile-CellNet, an efficient deep learning network that combines the power and robustness of deep learning with the efficiency of classical image processing. We also introduce a novel efficient deep learning based image segmentation network that is computationally efficient and still maintains the same level of accuracy as other widely used networks. Previous works in the area have relied on use of a small subset of high quality images for cell density estimation. The

biggest strength of this study is that we have used all the images available for the training and testing of our models. This allowed us to cover a wide variety of image quality, and imaging conditions resulting in a highly robust model. In addition to the models, we also propose a hybrid workflow that has proved to work better compared to using a single image segmentation networks proposed in the literature.

3.3 Materials and Methods

3.3.1 Materials:

The dataset used on this study was collected at the Johns Hopkins University School of Medicine [2]. A total of 612 images with varying image quality, cell size, cell density, and disease condition were collected using a Konan CellCheck XL specular microscope. Image have a size of 304×446. Out of these 612 images, clinical analysis using the flex-center method was available for 362 images. These 362 images were collected from 219 patients with a mean age of 38 years (Figure 3.1). 148 patients were female and 71 were male. 188 images were of the right eye and 174 images were of the left eye. In no case were multiple images from the same eye used in the training or testing.

[2]Data was collected for a different study approved by Johns Hopkins University School of Medicine Institutional Review Board *(IRB00039261)*

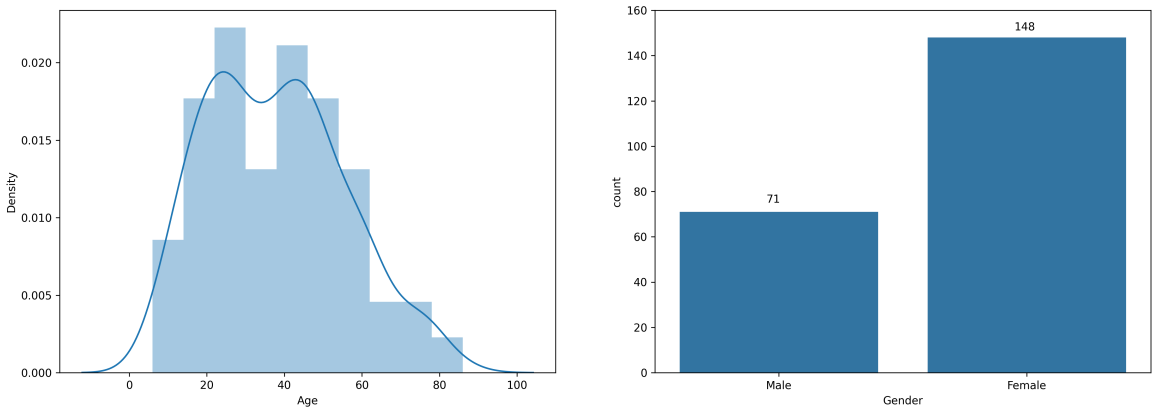

Figure 3.1: Age distribution of all the patients with a mean age of 38 years

To prepare the benchmark training set, we manually labeled all the images using Photoshop. Based on the manual labels, out of the 612 images 116 images were either poorly illuminated or were affected by diseases. The remaining 496 images had an average cell density of 2747 cells/mm^2 with an average of 107 cells counted per image. Figure 3.2 presents the histogram of the number of images for several cell count bins. Any image with less than 10 adjacent countable cells were not used to measure the cell density. In the dataset 26 images were affected by Fuchs dystrophy.

For testing, we used a holdout set of 125 images (20.4% of the entire dataset). One of these images had a CV over 100 which was removed, an outlier as by definition CV cannot have a value larger than 100. We suspect that this was due to an error. So, our final test set had a total of 124 images. Test images were randomly selected from the 362 images for which clinical flex-center analysis was present. The remaining 487 images were used for training.

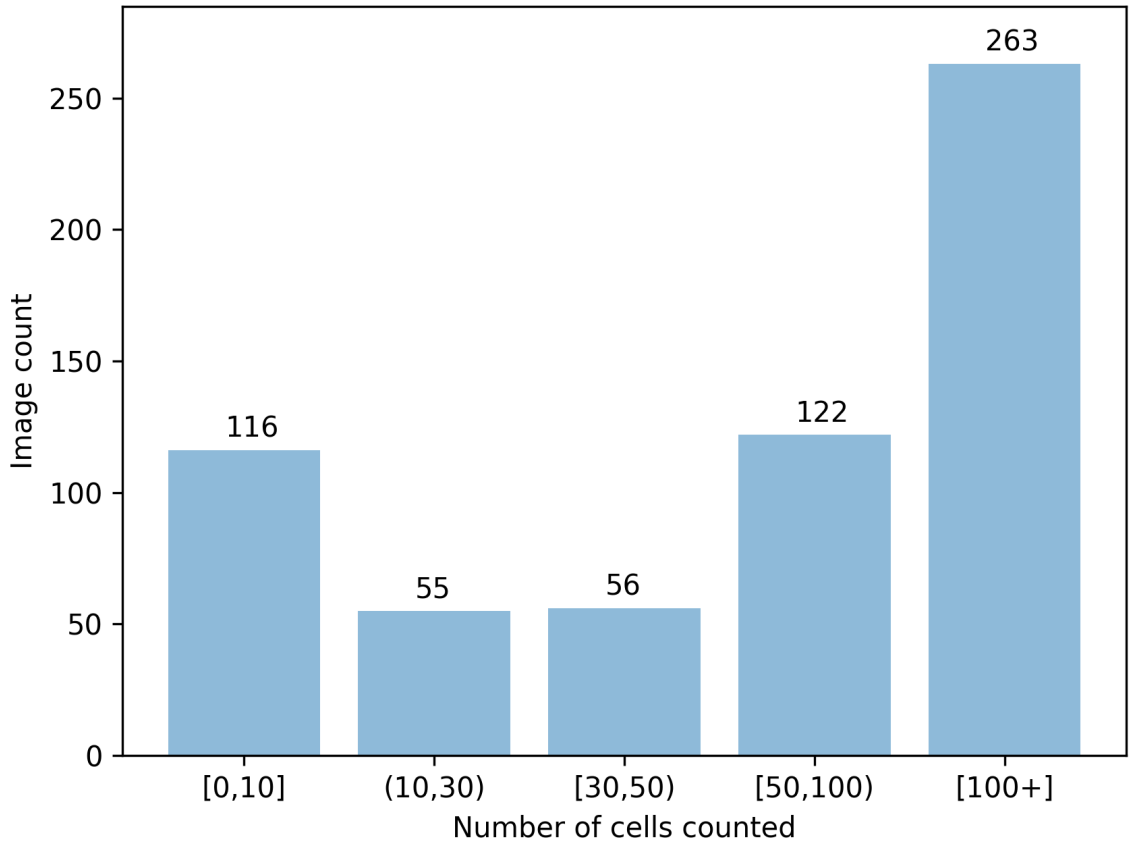

Figure 3.2: Histogram of the number of cells counted for 612 images in manual analysis

3.3.2 Methods:

The technique proposed in this work can be divided into three steps shown in Figure 3.3 (a); cell segmentation, region of interest (RoI) extraction, and post-processing. At the core of cell segmentation and RoI extraction steps are two identical deep learning network trained separately. The post-processing step, on the other hand, is classical image processing technique. Details of each processing step is given below.

3.3.2.1 Image labeling and data preparation

We created two different types of labels as shown in Figure 3.4. Cell segmentation label delineates the cell borders. The RoI label, on the other hand, only identified the areas where the cells are clearly visible. We also used the RoI label to mask images for training.

To artificially increase the size of the training set, we extracted 5 random patches of dimension 224×224 from all 487 training images. This increased our final training set size to 2435 images.

3.3.2.2 Cell segmentation

The purpose of this block, as the name suggests, is to produce a fine segmentation of the cells from the corneal endothelial images. To train this network, specular images were masked, using the RoI labels in Figure 3.4 to hide the areas without visible cell information. Figure 3.5 presents the process of image preparation for the training set for the cell segmentation. The masking allows the model to focus more on learning the difference between the cells and cell boundaries. It should be noted that the masking was only used during the network training and not the inference.

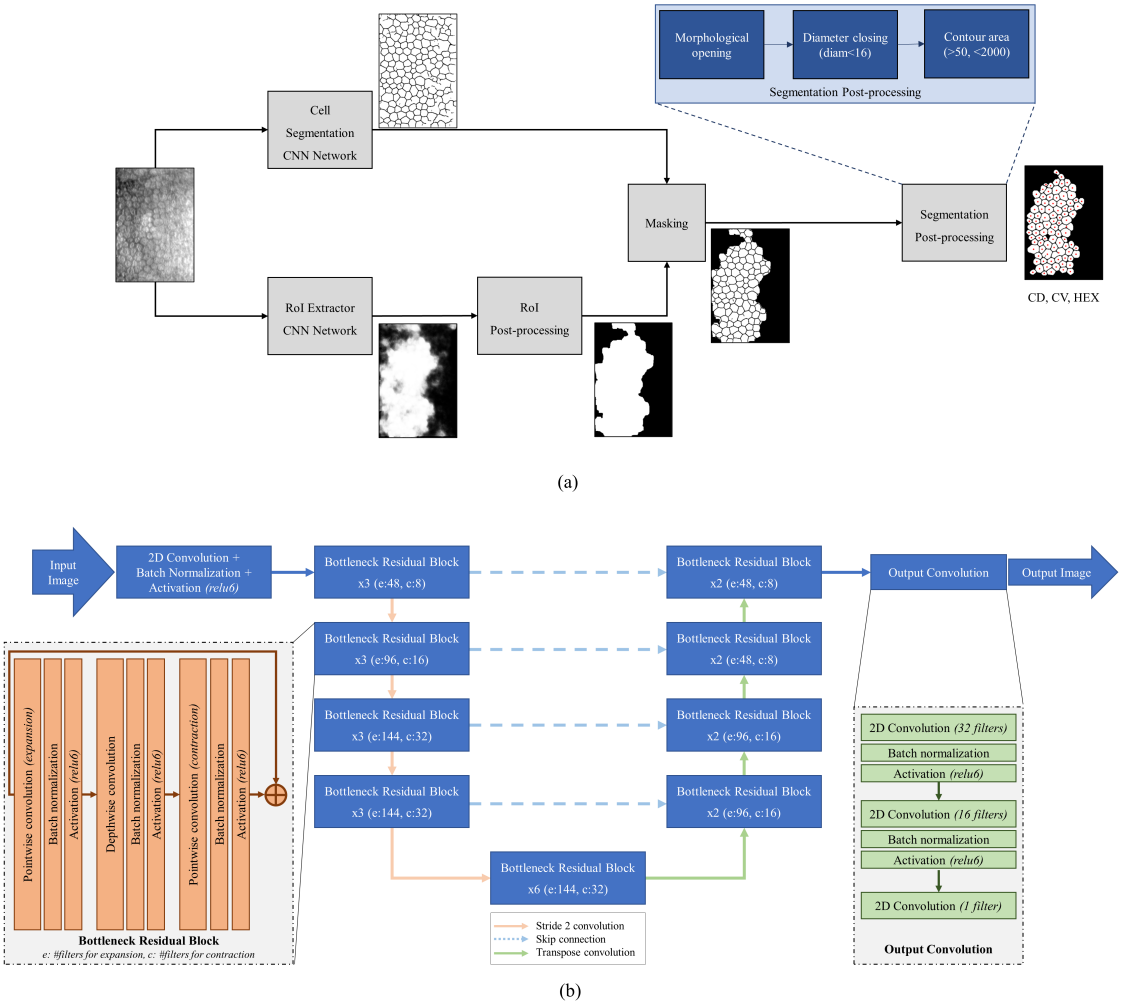

Figure 3.3: Mobile-CellNet architecture and block diagram

3.3.2.3 RoI Extraction

RoI extractor network produces a much coarser segmentation output to identify areas in the image with clearly visible cells. Original specular image (Figure 3.5 (a)) manually prepared RoI labels (Figure 3.5 (b)) was used to train the models. The output of the RoI extractor is processed using morphological opening operation to remove any

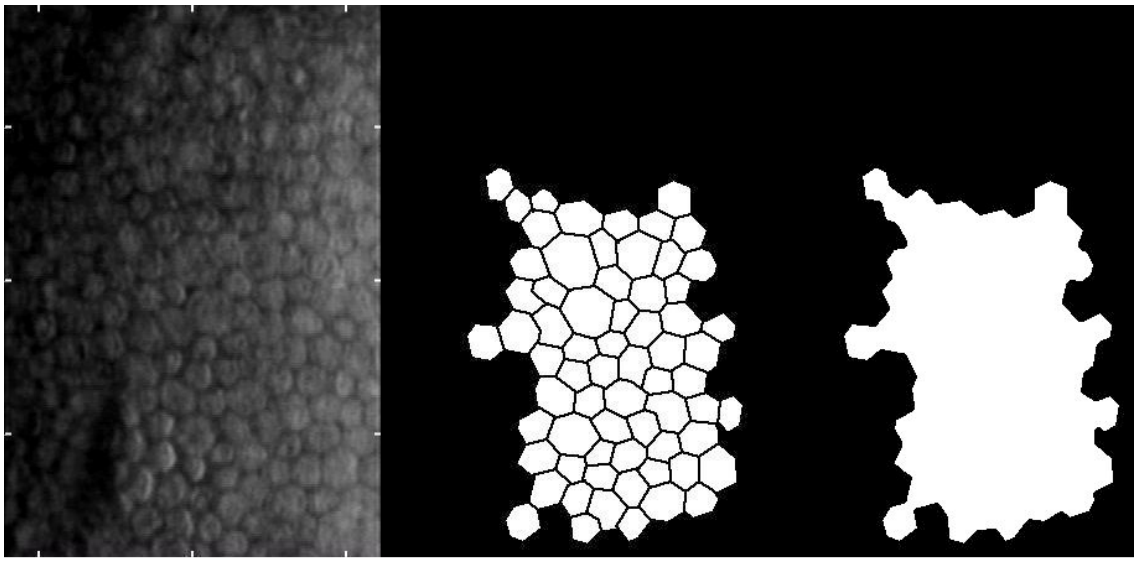

Figure 3.4: Sample training image and labels. (a) original specular image, (b) manual cell segmentation label, (c) manual RoI label

micro pixels. It was observed that in presence of disease, all the areas with enough visible cells may not be adjacent to each other, resulting in RoI extractor to identify multiple disconnected areas. However, for accurate analysis, only the adjacent cells should be counted. So, if multiple areas with visible cells are identified, the one with the largest area is selected. This ensures that only the adjacent cells are counted for the measurement.

The output from the ROI extractor step is then used as a mask on the output of the cell segmentation step to produce the final cell segmentation output.

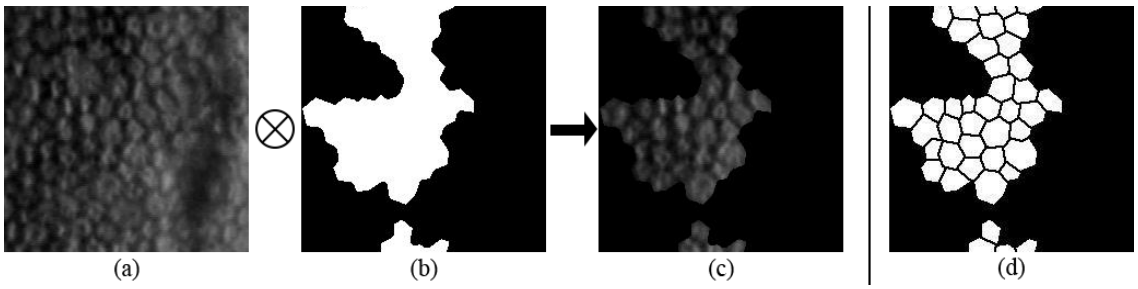

Figure 3.5: Steps of preparing the training images for the Cell Segmentation network model. (a) original specular image, (b) manual RoI label, (c) original image masked using the RoI label to create the masked image for the training, (d) output label

3.3.2.4 Segmentation post processing

Finally, the masked cell segmentation output is processed with a series of morphological operations to produce the final output. First, we use morphological opening followed by a closing to fill gaps that has smaller than 16 pixels in diameter. Next, we measure the area of each cell and only select the ones that contain between 50 pixels and 2000 pixels. From the training-set, we empirically found that 99.86% of the cells have sizes within those limits. Hence, any segment with area outside that range has a higher possibility of being the result of an over or under-segmentation. Finally, we measure the ECD, CV, and HEX.

Cell density was measured by calculating the number of cells counted in the area. CV was measured as the ratio between the mean and the standard deviation of the area of the cells in an image. To measure the HEX, we used the circularity C , defined as,

$$C = \frac{4\pi A}{P^2} \tag{3.1}$$

where A is the area, and P is the perimeter of each cell. A perfect hexagon has a circularity of 0.907. Hence, if a cell has a circularity between 0.85 and 0.91, we consider that as a hexagon.

3.3.2.5 Mobile-CellNet Architecture

For networks in cell segmentation and ROI extraction processing we designed Mobile-CellNet depicted in Figure 3.3 (b). This architecture uses U-Net [95], backbone with the bottleneck residual block for encoder and decoder. Each bottleneck residual block consists of a depthwise convolution layer stacked between two pointwise convolutions layers. Each convolution layer is followed by a batch normalization and a *relu6* activation except the last layer where a *sigmoid* activation was used for the final output. While the original U-Net had four resolution layers, Mobile-CellNet goes one level deeper with five resolution levels.

We start with the input image that is first convolved using a regular 2D convolution with 32 filters, followed by a batch normalization and *ReLu6* activation. This is then processed using bottleneck residual blocks in four levels. In each level feature maps are convolved by the level bottleneck residual three times ($\times 3$) with the last being

a stride two convolution to reduce the image resolution. Four level residual blocks, employ, respectively 8, 16, 32, and 32 numbers of filters. Similar to MobileNetv2 [96], we used an expansion factor of six resulting in 48, 96, 144, and 144 filters for the residual blocks. Finally, a encoder-decoder bridge bottleneck residual block is applied six times before increasing the image resolution through a transpose convolution layer for presentation to the decoder.

On decoder side, there are four levels with each applying the bottleneck residual block twice. The number of contraction filters on each level were, respectively, 16, 16, 8, and 8, and the number of expansion filters were 96, 96 ,48, and 48. The output of the last top level bottleneck residual block was processed using the three regular convolution layers with, respectively, 32, 16 and one filters.

3.3.3 Training hyperparameters

Our models were trained with the binary cross-entropy loss and Adam optimizer [97] with a learning rate of 0.0001. Validation dice coefficient was monitored to track the model's performance. The training was terminated if the validation dice coefficient did not improve after 50 epochs. Out of the 2435 training images, 20% was held out for validation to guard against overfitting. We used a batch size of eight based on the availability of the resources on the training platform. The models were trained and

tested on a computer with 6GB NVIDIA GTX 1060 GPU and 2GHz hexa-core Intel core i7 8^{th} generation processor.

3.3.4 Statistical analysis

In this paper we used one-way ANOVA and t-test for statistical comparisons. Since both the ANOVA and t-test assume that the sample distribution is normal, a sample size larger than 20 is ideal. As our testset had a total of 125 images, 107 of which had measurable cell density, ANOVA and t-test were appropriate to use.

3.4 Results

Figure 3.6 shows the output of various techniques and their corresponding cell densities for a randomly selected sample test image. As can be observed, manual and the deep learning methods produce similar results. On the other hand, the classical image processing method fails to produce similar segmentation results, and accurate cell density. As the last three images in Figure 3.6 shows, the results for three deep learning techniques being almost identical, with Mobile-CellNet being most consistent. It should be noted that both manual and UNet++ [98] have missed some cells from the middle of the image. On the other hand, UNet and Mobile-CellNet were

able to mark those cells.

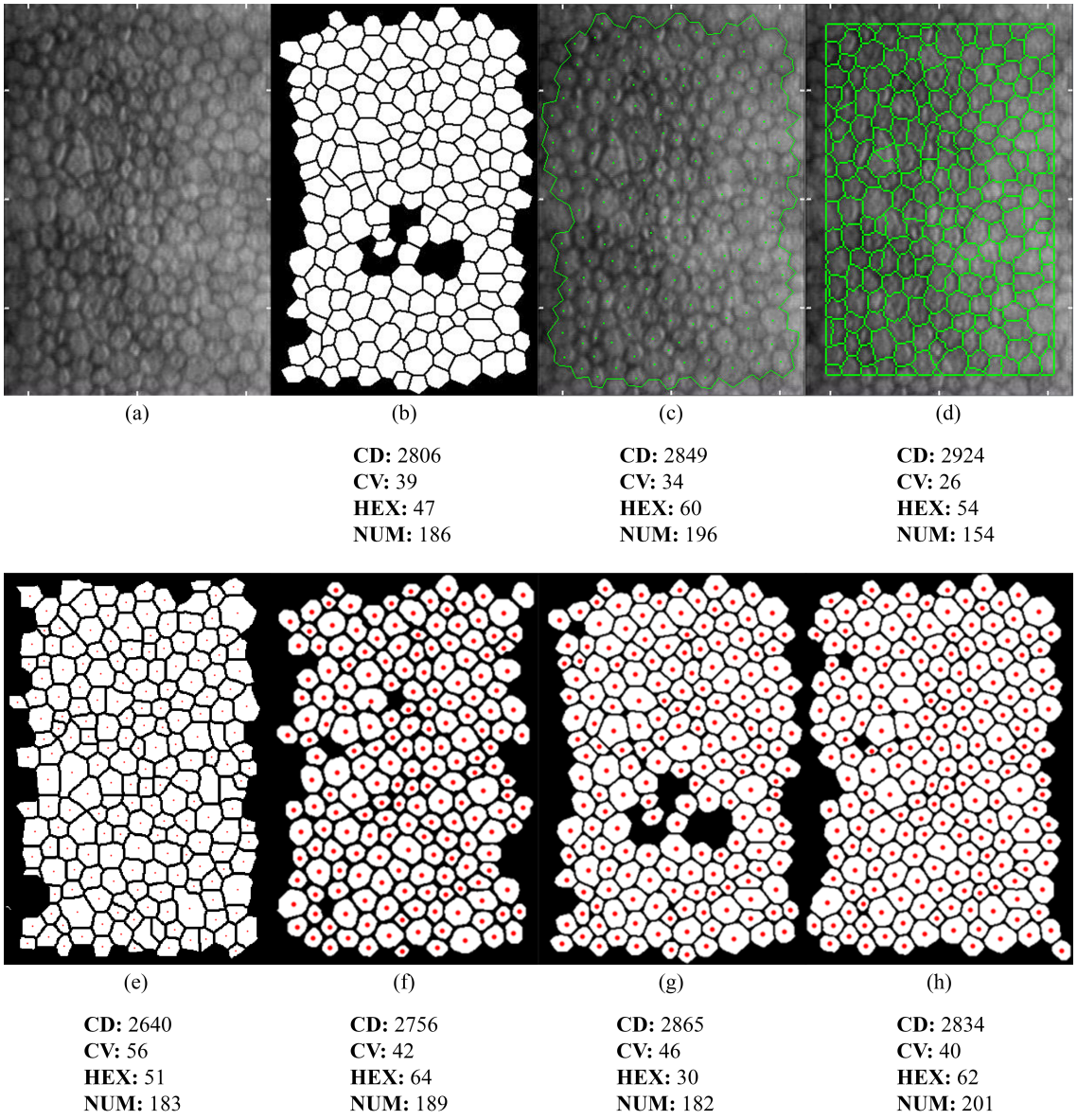

Figure 3.6: Output of a randomly selected sample image using different methods and cell statistics. (a) original image, (b) manual analysis, (c) clinical flex-center method, (d) AutoTracer, (e) classical analysis, (f) UNet, (g) UNet++, (h) Mobile-CellNet

Figure 3.7 shows the output of the Mobile-CellNet after each operation where (b) through (g) represents output of the cell segmentation processing step, output of the

RoI extractor, post-processed output of the RoI, masked cell segmentation image, post-processed cell segmentation, and the final output with cell centers marked in red. This figure shows the importance of each step and the use of post-processing to improve the outcome.

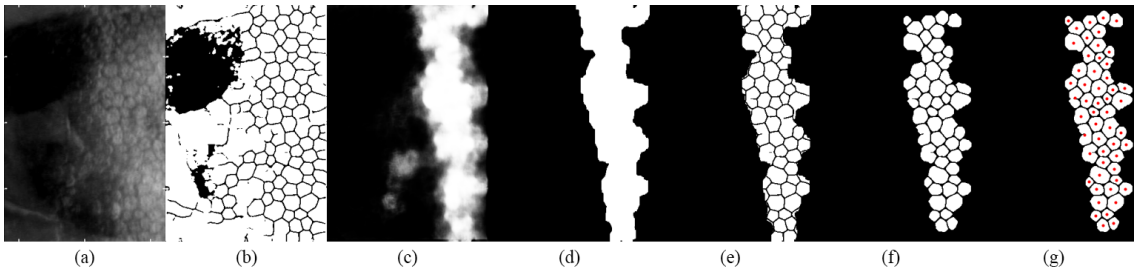

Figure 3.7: Output for each layer of a randomly selected sample image using the Mobile-CellNet. (a) original image, (b) output of the cell segmentation block, (c) output of the RoI extractor block, (d) post-processed RoI extractor, (e) Masked cell segmentation, (f) filtered and post-processed segmentation, (g) final output with cell centers marked in red.

Our test set had a total of 124 images with 18 images having the zero cell density due to the poor image quality. Table 3.1 presents the the summary of the results. Using the manual analysis, the mean cell density of the test set was 2805 cells/mm^2 with a range of 2036 and 3847 cells/mm^2. The average number of cells count per image was 119. Clinical analysis using the flex-center method had an average cell density of 2717 cells/mm^2 with the range of 2064 and 3390 cells/mm^2. The mean absolute difference between the two manual method is 4.59% with a Pearson correlation coefficient of 0.89.

Also from Table 3.1 we observe that UNet/UNet++ the mean cell density is

2766/2831 cells/mm^2 with a range between 1964/2010 and 4096/3993 cells/mm^2 and with an average of 112 cells count per image. The mean absolute error was 3.80%/4.38% and a Pearson correlation coefficient of 0.94/0.91.

For Mobile-CellNet we observe that the mean cell density is 2699 cells/mm^2 with a range between 2015 and 3560 cells/mm^2 and with an average of 156 cells count per image. The mean absolute error was 4.08% and a Pearson correlation coefficient of 0.94.

The two classical methods, AutoTracer and classical image processing reported in our previous work [1] performed least accurately with a mean absolute error of 7.20% and 8.37%, respectively.

We have also measured CV and the hexagonality. UNet and the classical methods had the smallest mean absolute error respectively, for CV and hexagonality. However, performance of Mobile-CellNet was comparable with mean absolute error of 15.81% and 31.90% respectively for these parameters.

Having comparable accuracy with the other deep learning techniques, Mobile-CellNet outperforms the others in terms of efficiency. It required a total of only 7.78 GFLOPs per inference and only 0.25 million parameters (Table 3.2). UNet on the other hand requires 237.59 GFLOPs with 8.56 million parameters. UNet++ was the least efficient model with 696.31 GFLOPs and 11.80 million parameters. The average times required

to run 125 images were, respectively, 1.55, 1.98 and 1.31 seconds for UNet, UNet++, and Mobile-CellNet on the chosen platfrom.

Table 3.1
Accuracy comparison table between different techniques

	Manual (benchmark)	**Clinical (flex-center)**		**Auto Tracer**		**Classical**	
	CD	**CD**	**MAE%**	**CD**	**MAE%**	**CD**	**MAE%**
Mean	2805	2717	4.59	2841	7.20	2678	8.37
SD	392	324	3.98	191	5.66	177	5.36
Min.	2036	2064	0.04	2283	0.16	2289	0.34
Max.	3847	3390	19.98	3356	23.44	3133	25.54
	CV	**CV**	**MAE%**	**CV**	**MAE%**	**CV**	**MAE%**
Mean	32	35	18.03	30	16.77	34	**13.39**
SD	6	6	22.68	7	16.49	3	11.17
Min.	22	21	0	19	0	26	0
Max.	48	58	145.45	90	157.14	40	63.64
	HEX	**HEX**	**MAE%**	**HEX**	**MAE%**	**HEX**	**MAE%**
Mean	60	62	11.70	49	19.36	62	19.97
SD	9	8	12.30	10	14.12	9	14.99
Min.	39	44	0	0	0	32	0
Max.	80	88	76	75	100	79	70.73
		UNet		**UNet++**		**Mobile-CellNet**	
		CD	**MAE%**	**CD**	**MAE%**	**CD**	**MAE%**
Mean	—	2766	**3.80**	2831	4.38	2699	4.06
SD	—	392	3.08	409	4.45	349	3.94
Min.	—	1964	0.10	2010	0	2015	0.08
Max.	—	4096	14.99	3993	23.79	3560	19.25
		CV	**MAE%**	**CV**	**MAE%**	**CV**	**MAE%**
Mean	—	35	14.05	38	22.57	41	31.90
SD	—	6	10.45	7	20.59	8	29.52
Min.	—	24	0	24	0	28	0
Max.	—	50	58.33	66	164	63	148
		HEX	**MAE%**	**HEX**	**MAE%**	**HEX**	**MAE%**
Mean	—	61	**14.69**	35	40.81	55	15.81
SD	—	8	14.30	10	16.73	8	11.51
Min.	—	35	0	18	0	35	0
Max.	—	88	69.23	62	75.34	74	52.70

Table 3.2
Performance comparison for different models

	FLOPs *(Giga)*	**Parameters** *(Millions)*	**Time/Image** *(seconds)*	**MAE%**
Clinical *(Flex-center)*	—	—	—	4.59%
Auto Tracer	—	—	—	7.20%
Classical	—	—	2.50	8.37%
UNet	237.59	8.56	1.55	**3.80%**
UNet++	696.31	11.80	1.98	4.38%
Mobile-CellNet	**7.78**	**0.25**	**1.31**	4.06%

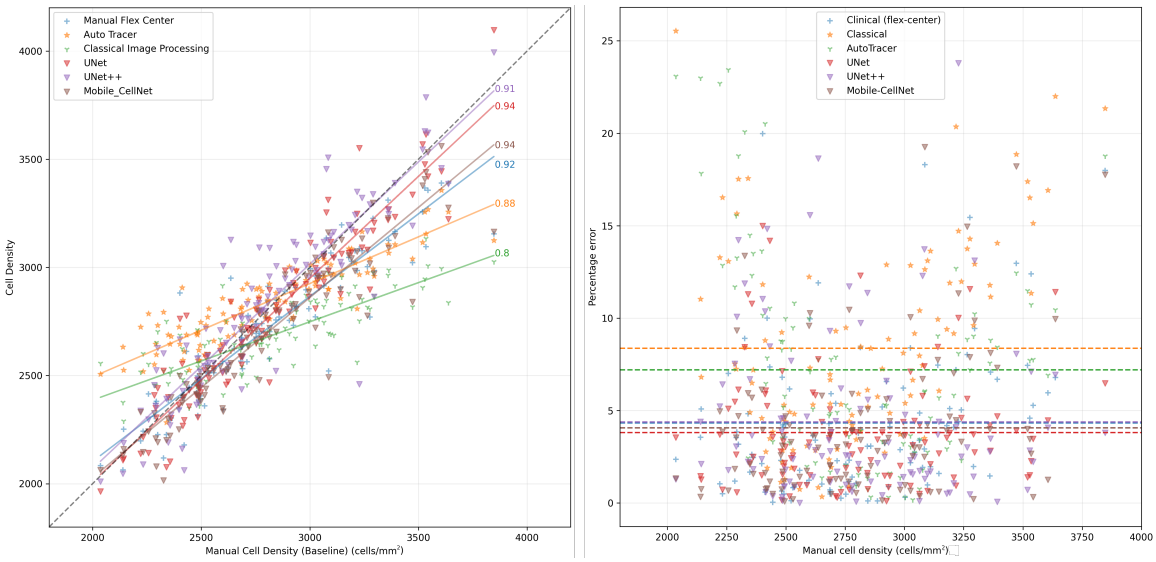

Figure 3.8: Scatter plot comparing the accuracy of different models with respect to the benchmark manual analysis.

3.5 Discussion

One-way ANOVA between our benchmark manual analysis, clinical analysis using flex-center, UNet, and the proposed Mobile-CellNet showed no significant difference with a $p-value$ of 0.11 in the cell count. This indicates time, and resource-consuming

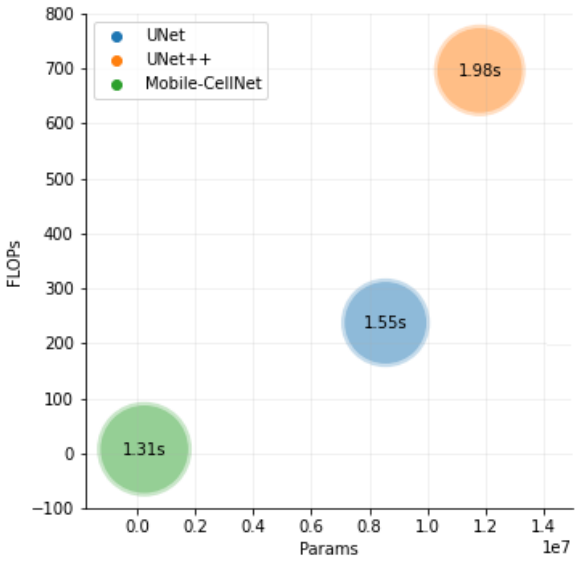

Figure 3.9: Scatter plot of the performance of the three deep learning models with respect to FLOPs count, number of parameters and inference time. While X and Y axis represents the number of parameters and FLOPs respectively, the size of the markers are determined by the inference time.

manual count can be automated through a deep learning technique. Among the deep learning techniques, however, Mobile-CellNet requires 30.5 times fewer floating-point operations (FLOPs) and 34.2 times fewer parameters compared with UNet, a desirable feature for low-resource embedded computing devices. One study shows [34] that manual inter-rater technicians' reliability for 2 different centers could be ±10%, while for the same technician, the error could be between ±2% and ±5%. Deep learning techniques produced a mean error below the acceptable threshold.

To measure and identify the effectiveness of the RoI extractor, we only used the Cell Segmentation processing step in Figure 3.3. We observed that for the Mobile-CellNet, the MAE increased from 4.06% to 7.20% with a CV of 0.87. This is a significant (P

value = 0.0001) reduction in accuracy compared with the manual analysis. On the other hand, the model inference time was only reduced by 50 milliseconds to 1.26 seconds. This minor difference comes with a significant ($p - value = 0.045$) 3.40% reduction in accuracy.

Figure 3.8 shows a strong correlation between the benchmark data and UNet with a correlation coefficient of 0.94. Mobile-CellNet achieved the same correlation of 0.94 followed by UNet++ with a CV of 0.91. Auto Tracer and the classical method could not perform as accurately, and the correlation is much lower.

Figure 3.9 compares the efficiency of 3 deep learning models where the x-axis represents the number of parameters used and y-axis represents the number of FLOPs required by the model to process a single image. The closer the marker to the origin, the more efficient the model is. In addition, the marker size was determined by the MAE of the model. As can be observed, Mobile-CellNet is closest to the origin with the lowest inference time. It can also be observed that while the size of the marker is the smallest for the UNet, the difference is minimal.

In [53], a similar RoI extraction step was used. However, the work used a more complex DenseNet model. The key difference between that model and Mobile-CellNet is that the work in Ref. 20 used the RoI extractor on the segmentation map to identify the RoI before applying it as a mask and performing postprocessing to produce the cell statistics. In the case of Mobile-CellNet, 2 parallel networks were used to detect

the RoI and perform the cell segmentation simultaneously. The work [53] reported a 2.5% error for ECD compared with the 4.08% that we estimated using Mobile-CellNet; the difference is a major part because of the use of the Topcon specular microscope that produces higher quality images. The work collected images from the Descemet stripping automated endothelial keratoplasty (DSAEK) patients over a year; for each patient, at least 4 images of the same eye were taken over the course of a year. It is unclear from [53] how the data set was divided for training and testing; however, if the images of the same patient were used both for training and testing, that accounts for the model's boosted performance.

Figure 3.10 compares the performance between classical image processing [1] and the deep learning method. Although the similar use of RoI demarcation helped the classical technique to eliminate darker areas from the measurement, the cell segmentation was not as consistent as the deep learning method as we can observe from the side-by-side comparison. Classical image processing suffered more from over-segmentation compared with Mobile-CellNet. This ultimately led to a higher MAE. We can also observe from Table 3.1 that the range for both classical methods, Auto Tracer, and the technique in reference [1], was smaller compared with the deep learning methods and manual techniques. Previous classical image processing methods [77, 86] and a hybrid technique [38] also reported higher errors compared with the proposed model in this article.

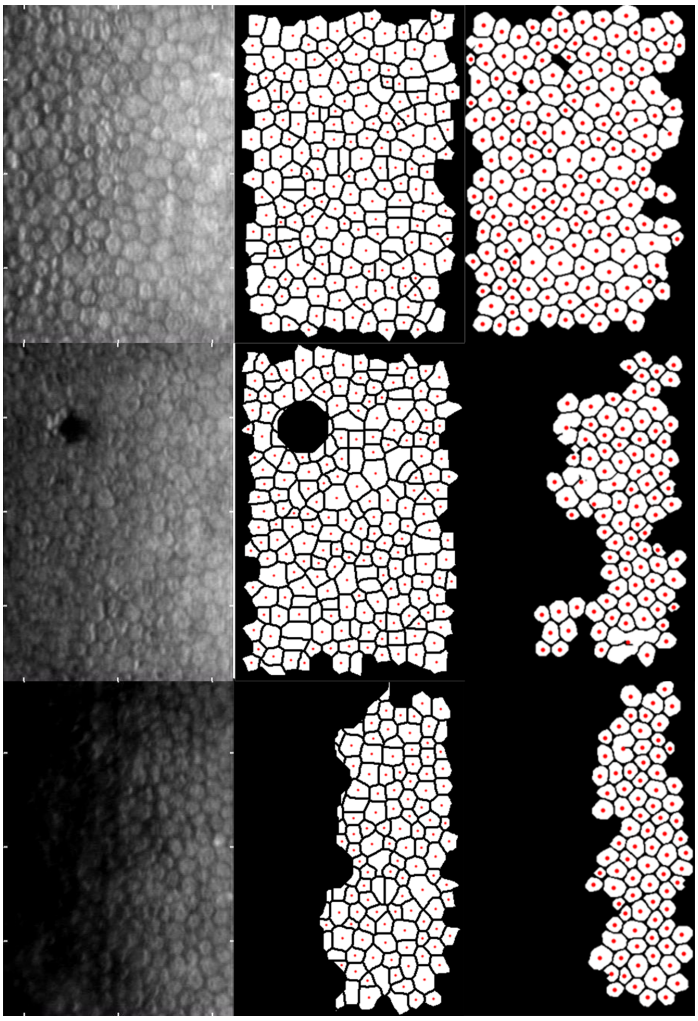

Figure 3.10: Three sample images comparing the output of classical image processing [1] and Mobile-CellNet. From left, column 1 is the original image, column 2 is the output of the classical image processing, and column 3 is the output of the Mobile-CellNet using the method proposed in this paper.

Although all 3 deep learning methods produced the most consistent results and an acceptable MAE, a closer look at the outputs showed that they suffer from minor under segmentation. Figure 3.11 shows 2 erroneous segmentation results from 2 randomly selected sample images using the Mobile-CellNet model. Although these errors did not significantly affect the overall ECD estimation, they affected HEX and

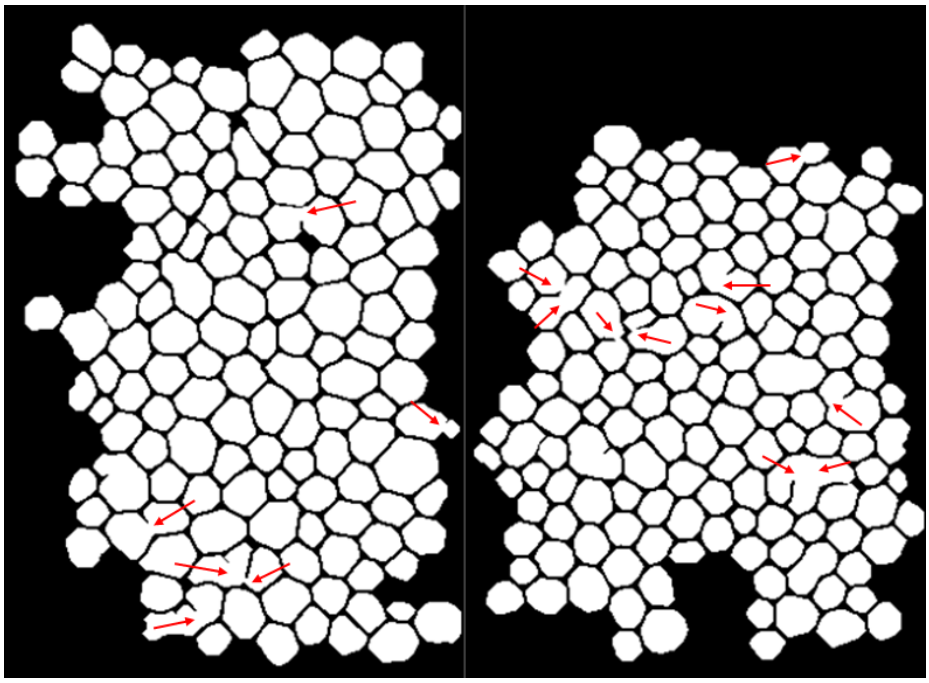

Figure 3.11: Sample outputs of the proposed method using Mobile-CellNet showing the limitation of this model to produce under segmented results.

CV measurements leading to a higher error. This limitation needs to be addressed in the future work

3.6 Conclusion

In this article, we proposed a corneal endothelial cell segmentation technique that uses a hybrid approach with deep learning and classical image processing. We also proposed a novel efficient cell segmentation architecture that produces similar results as other state-of-the-art techniques but requires significantly fewer parameters and FLOPs for a single segmentation task.

Chapter 4

Alcohol Abuse Is Associated With Alterations in Corneal Endothelial Cell Morphology

Authors: *Ranit Karmakar, Saeid Nooshabadi, John Lohmeier, Staci Terrin, Allen O. Eghrari* [1]

[1]Karmakar, R., Nooshabadi, S., Lohmeier, J., Terrin, S. and Eghrari, A.O., 2022. Alcohol Abuse Is Associated With Alterations in Corneal Endothelial Cell Morphology. Cornea, pp.10-1097.

4.1 Abstract

4.1.1 Background

Alcohol consumption is highly prevalent throughout the world. We sought to detect, in a large sample of cornea donors, whether alcohol abuse is associated with changes in corneal endothelial morphology after accounting for other comorbidities including tobacco use.

4.1.2 Methods

At a single eye bank, 10,322 eyes from a total of 5,624 unique donors underwent imaging with a Konan CellChek D specular microscope. Demographic information and medical history was associated with each tissue. Images were analyzed using a standardized protocol for assessment of endothelial cell density, hexagonality, and variation. In this retrospective analysis, a multivariable regression was conducted to assess for an association between alcohol abuse and corneal endothelial metrics. Measurements were averaged across eyes for each donor. Bonferroni corrections were applied to account for multiple comparisons.

4.1.3 Results

Among 5,624 donors, the mean (standard deviation) endothelial cell density was 2,785 (383.0) cells/mm^2. Indicators of alcohol abuse were present in 1,382 donors (24.5%). In a multivariable regression model that included age, sex, tobacco use, history of cataract surgery and diabetes mellitus, alcohol abuse was associated with a decrease of 60.9 cells/mm^2 (95% confidence interval (CI), -83.0 to -38.7 cells/mm^2, p=7.6×10^{-8}), an increase in the coefficient of variation by 0.0048 (95% CI, 0.17 to 0.79, p=0.002), and a decrease in percent hexagonality by 0.93% (95% CI, -1.3 to -0.6, p=4.5×10^{-7}).

4.1.4 Conclusions

Alcohol abuse is associated with significant alterations to corneal endothelial density and morphology.

4.2 Introduction

Alcohol abuse is one of the most prevalent substance use disorders in the world, affecting approximately 283 million people in 2018 [99]. Heavy alcohol consumption contributes to damage at both cellular and structural levels throughout the central nervous system [100]. Within the eye, a well-established association exists between alcohol abuse and optic nerve, retinal, and lens pathology [101]. Nevertheless, more research is needed to understand the clinical effects of alcohol on the corneal endothelium.

Comorbidities and use of additional substances among heavy users of alcohol create a challenge in conducting clinical research into the effects of alcohol use or abuse. For example, a strong association exists between use of alcohol and use of cigarettes [102], and tobacco is associated with decreased corneal endothelial function [103]. Although a direct comparison of individuals affected and unaffected by alcohol dependence suggests a deleterious impact on corneal endothelial cell density (ECD) [104], no study to date to the best of our knowledge has examined an association between heavy alcohol use and corneal endothelial characteristics in the context of comorbidities. Analyses with a large data set and adjusting for additional variables would be helpful to address potential confounders.

Data from eye banks, which conduct specular microscopy and collect clinical data for every cornea received, offer a unique opportunity to assess the impact of environmental factors on the corneal endothelium. Large studies from eye banks have successfully identified the effects of diabetes, cataract surgery, and smoking on the corneal endothelium [102, 103], but heavy alcohol use has yet to be considered among such factors.

In this study of over 10,000 corneal endothelial images and associated medical history analyzed from an eye bank, we examined the effect of heavy alcohol use on the corneal endothelium in the setting of additional factors, such as smoking and diabetes, to better ascertain the specific contribution of this risk factor for corneal endothelial cell loss.

4.3 Methods

During routine evaluation, all donor corneas that were processed at the Rocky Mountain Lions Eye Bank (RMLEB) in Colorado, United States underwent specular microscopy for quantitative and qualitative analysis of the corneal endothelium, analyzed manually using a single Konan CellChek D. Medical history and demographic information was associated with each image. Corneal endothelial density (CD), coefficient of variation (CV), and percent hexagonality (HEX) were calculated and documented

for each image at the time of tissue processing.

All images from September 15, 2016 to August 3, 2020 were acquired for analysis. For statistical analyses, values were averaged across eyes and duplicates were removed. Three eyes were excluded from analysis as the CV value was recorded as greater than 100, which is a statistical impossiblity and suggests that data entry may have been compromised for these individuals. These represent less than a tenth of one percent of total donors.

To determine the quality of analysis, we assessed the total number of cells counted per image, applying a standardized grading system for eye bank images.6 In this system, we applied a grade of 4 if 100 or more cells were analyzed, 3 if 50–99 cells were analyzed, 2 if 15–49 cells were analyzed, or grade of 1 if less than 15 or no cells were analyzed.

Medical history for each patient was acquired by RMLEB from hospital medical records and included whether alcohol dependence or its sequelae were present. To apply a conservative estimate for the association and prevent selecting for only the most well-documented severe cases of alcohol abuse, which would artificially inflate the effect of alcohol consumption, we performed a search in the medical history of donors for the term “alcohol” or “EtOH”. Once a list of all medical histories with these terms were acquired, the list was manually curated to exclude non-alcohol related terms, such as “non-alcoholic hepatitis” that would appear in the search. Cases

of secondary organ failure, such as cirrhosis, specifically mentioned as being due to alcohol ("alcoholic cirrhosis") were included. Similarly, for tobacco use, medical histories were searched for the terms "tobacco" or "smoking". For diabetes, we included the terms "diabetes," "diabetic," "DM1" and "DM2" and then excluded cases with terms such as "pre-diabetes." For lens status, we searched for the terms "pseudophakic," "pseudophakia" and "cataract surgery".

We first conducted a descriptive analysis and assessed differences in values between donors with each factor compared to donors without any of these factors. To do so, we conducted a multivariable regression including age and sex as variables. Second, we utilized a multivariable regression to account for the combined effect of age, sex, cataract surgery status, diabetes, history of heavy alcohol use, and history of tobacco use on corneal endothelial characteristics. Given these six factors considered, we applied Bonferroni corrections and α was reduced from 0.05 to to 0.0083.

4.4 Results

The dataset included 10,322 images from a total of 5,624 unique donors. The average analysis included 99 cells per image. The distribution plot of the cells analyzed is included in the Supplemental Data. More than 100 cells were counted on average from 2,564 donors (Grade 4 of 4), between 50-99 cells from 3,055 donors (Grade 3

of 4), between 15-49 cells from 5 donors (Grade 2 of 4), and no donors contributed tissues with a mean of less than 15 cells counted (Grade 1/4).

Of these donors, the median age was 58, with an interquartile range (IQR) of 47 (25th percentile) to 65 years old (75th percentile). A total of 2357 donors (41.9%) were female. Indicators of alcohol use were present in 1382 donors (24.5%), tobacco use in 1113 donors (19.8%), diabetes mellitus in 1271 donors (22.6%), and pseudophakia in 585 donors (10.4%). The remaining 2423 individuals (43.1%) had none of these risk factors for endothelial cell loss.

Table 4.1

Common terms associated with alcohol in the medical history of 5624 donors to a single eye bank over a four-year period. The terms below represent those included in the medical history of at least 30 donors. Of 350 total alcohol-related terms identified in the dataset, "Alcohol Abuse" was the most common, while 265 terms were used only once. Terms not associated with alcohol abuse, such as "non-alcoholic steatohepatitis" were excluded from the dataset.

Most Common Exact Terms in Donor Medical History Associated with Alcohol ($n > 30$)	
Medical History Term	**Number of Entries**
Alcohol Abuse	958
Alcoholic Cirrhosis	109
Alcoholism	88
Alcoholic hepatitis	68
Alcohol withdrawal	58
Alcohol abuse with alcoholic cirrhosis	41
Alcohol abuse in the past	31

A total of 350 alcohol-related medical history phrases were identified in the dataset, of which seven appeared more than 30 times each. Of these, "Alcohol Abuse" (n=958), "Alcoholic Cirrhosis" (n=109), and "Alcoholism" (n=88) were by far the three most

common descriptors. The majority of terms were only used once (265/350, 75.7%). Many of these terms were variations or additions to simple terms, such as "history of alcohol abuse chronically" (n=1) or "former alcohol abuse with recent relapse" (n=1). Table 4.1 includes the most common exact terms associated with heavy alcohol use in the medical history of donors. All alcohol-associated terms and their frequency are included in the Supplemental Data.

Table 4.2
Corneal endothelial characteristics in eyes of 5624 cornea donors to Rocky Mountain Lions Eye Bank. For each risk factor, a multivariable regression was conducted including age and sex as variables. Assessments for age included sex and the risk factor in question as variables. ECD: Endothelial Cell Density. HEX: Hexagonality. CV: Coefficient of Variation.

	All (n=5624)		**Alcohol Abuse (n=1382)**				**Pseudophakia (n=585)**			
	Mean (SD)	**Median (IQR)**	**Mean (SD)**	**Median (IQR)**	**Effect Estimate (95% CI)**	**p-value**	**Mean (SD)**	**Median (IQR)**	**Effect Estimate (95% CI)**	**p-value**
Age (years)	54.2 (-14)	58 (47-65)	52.4 (12.5)	55 (43 - 62)	**-2.4 (-3.3 - -1.6)**	3.6×10^{-8}	63.4 (-7.6)	65.0 (60-68)	**10.1 (9.0 - 11.3)**	3.9×10^{-63}
ECD (cells/mm^2)	2785 (-383)	2780 (2548 - 3027)	2756 (-343.5)	2756 (2538 - 2977)	**-60.9 (-83.0 - -38.7)**	7.6×10^{-8}	2631.7 (408.7)	2630.5 (2392 - 2884)	**-88.1258 (-120.0 - -56.3)**	6.0×10^{-8}
HEX (%)	56 (-6.2)	56 (52 - 60)	56 (-6.1)	56 (52 - 60)	**-0.93 (-1.3 - -0.57)**	6.6×10^{-7}	55.7 (5.6)	55.5 (52.0 - 59.0)	0.44 (-0.085 - 0.97)	0.1
CV (×100)	36.5 (-5.2)	36 (33 - 39)	37 (-4.9)	36 (34 - 39)	**0.48 (0.17 - 0.79)**	**0.002**	37.0 (5.4)	36.0 (34.0 - 40.0)	-0.23 (-0.68 - 0.21)	0.31
	Unaffected by selected risk factors (n=2423)		**Diabetes Mellitus (n=1271)**				**Tobacco Abuse (n=1113)**			
	Mean (SD)	**Median (IQR)**	**Mean (SD)**	**Median (IQR)**	**Effect Estimate (95% CI)**	**p-value**	**Mean (SD)**	**Median (IQR)**	**Effect Estimate (95% CI)**	**p-value**
Age (years)	51.9 (15.9)	57 (43 - 64)	59.1 (9.4)	61.0 (54.0-66.0)	**6.2 (5.4 - 7.1)**	4.4×10^{-45}	55.7 (12.7)	60.0 (48.0-65.0)	**1.9 (1.0 - 2.8)**	4.2×10^{-5}
ECD (cells/mm^2)	2838 (-386)	2825 (3595.5 - 3075.3)	2731.8 (396.4)	2735.0 (2492.0-2976.0)	-15.8 (-38.9 - 7.3)	0.18	2737.7 (367.5)	2732.0 (2500.0-2985.0)	**-42.9 (-66.7 - -19.0)**	4.3×10^{-4}
HEX (%)	56.8 (-6.5)	56.5 (52.5 - 56.5)	55.7 (5.6)	56.0 (52.0-60.0)	-0.092 (-0.48 - 0.29)	0.64	56.0 (5.8)	56.0 (52.0-60.0)	-0.16 (-0.56 - 0.24)	0.42
CV (×100)	36.1 (-5.3)	35.5 (33 - 38.5)	37.1 (5.2)	36.5 (34.0-40.0)	0.31 (-0.011 - 0.64)	0.058	36.8 (5.1)	36.0 (34.0-40.0)	0.18 (-0.150 - 0.52)	0.28

The median endothelial cell density in the dataset was 2780 (IQR 2548 to 3027). Table 4.2 summarizes demographic and endothelial (CD, CV and HEX) values. Including age and sex as additional variables, alcohol abuse, tobacco abuse, diabetes mellitus, and pseudophakia were all associated with significantly different values relative to controls without any such factors.

Table 4.3

Multivariable linear regression of risk factors for corneal endothelial damage in a set of specular microscopy images from 5624 unique donors. Even after adjusting for additional risk factors, alcohol abuse is strongly associated with changes in endothelial cell density, coefficient of variation, and hexagonality. Numbers in bold are those that reached the threshold for statistical significance after adjusting for multiple comparisons.

	Endothelial Cell Density		Coefficient of Variation		Hexagonality	
Factor	Coefficient (cells/mm^2)	p-value	Coefficient (x100)	p-value	Coefficient (%)	p-value
Intercept	3263.7	—	32.4	—	62.2	—
Age	-8.2	6.8×10^{-111}	0.07	2.2×10^{-43}	-0.1	2.5×10^{-63}
Female Sex	-0.67	0.95	0.28	0.044	-0.39	0.016
Alcohol Abuse	-60.7	9.8×10^{-8}	0.49	0.002	-0.94	4.8×10^{-7}
Tobacco Use	-35.8	0.003	0.15	0.39	-0.07	0.729
Diabetes	-12.8	0.28	0.42	0.011	-0.21	0.285
Pseudophakia	-87.7	8.7×10^{-8}	-0.3	0.19	0.45	0.099

In the multivariable regression model of multiple factors (Table 4.3), alcohol abuse was significantly associated with changes to each of the endothelial characteristics studied. The data demonstrated a decrease of approximately $60.9 cells/mm^2$ relative to donors without history of alcohol abuse (95% confidence interval (CI), -83.0 to

-38.7 cells/mm^2, $p - value = 7.6 \times 10^{-8}$). A small increase in the coefficient of variation (+0.0048, 95% CI, 0.17 to 0.79, $p - value = 0.002$), and a decrease in hexagonality of approximately one percentage point (-0.93%, 95% CI, -1.3% to -0.6%, $p - value = 4.5 \times 10^{-7}$) was appreciated in donors with a history of alcohol abuse. In this model, tobacco use and cataract surgery also each contributed to decreased endothelial cell count, with an estimated decrease of 36 ($p - value = 0.003$) and $88 cells/mm^2$ ($p - value = 8.7 \times 10^{-8}$) respectively, among those harboring these risk factors.

4.5 Discussion

This study contributes a large dataset to explore the effect of heavy alcohol use on the corneal endothelium. Quantitative and qualitative changes in endothelial morphology appeared even after adjusting for additional factors.

Drawing on eye bank data offers unique insights into disease associations in a region, and selects from a patient population broader than a specific hospital. Previous work drawing on such data has assessed the effects of hypertension, glaucoma, depression, dementia and neurodegenerative diseases, thyroid dysfunction, and tobacco use [105]. Here, we confirm heavy alcohol use among known deleterious factors to the corneal endothelium and identify a strong association with ECD loss. Replication of this

finding by eye banks in additional regions of the world would be helpful to confirm that this finding is generalizable across populations. Given the strength of this association, it may be helpful to consider alcohol abuse as a potential comorbidity when studying the effects of other clinical variables on corneal endothelial health.

Further research is needed to understand the specific pathological changes that take place in the setting of heavy alcohol use. It has been postulated that conversion of alcohol to acetaldehyde may result in direct cytotoxicity to the corneal endothelium [106], which offers one possible pathway, but the physical, social and behavioral aspects of alcohol abuse, which can include malnutrition and metabolic alterations, offer alternative mechanisms worthy of study.

By including all medical histories specifically mentioning alcohol use, we sought to identify a conservative estimate; the true association of alcohol abuse with endothelial cell loss may be even greater than what was described in this study. Further research into a dose-response curve between light and heavy alcohol use would offer additional insights into the alcohol-associated risks to the endothelium. In this study, we did not distinguish between former and recent alcohol abuse, as endothelial cell loss is sustained over time and corneal endothelial cells do not replicate. Therefore, any endothelial cell loss would be expected to sustain over the lifespan. However, whether there is a difference in endothelial cell morphology between patients with varying histories of alcohol dependence could be an area of additional future research.

This study suggests that, in addition to decreased endothelial cell density, changes occur in hexagonality and the coefficient of variation with heavy alcohol use. While a previous clinical study that assessed alcohol dependence did not identify a difference in these characteristics [103], these patterns may be more discernible in this larger dataset, and particularly when adjusting for confounding variables. Variability in the shape and size of cells is of particular importance as it is associated with cell stress and has been associated with a higher likelihood of corneal decompensation after intraocular surgery [107] [108].

The estimated effect of alcohol abuse on ECD was modest at 60.9 cells/mm^2, a small percentage of the median ECD in this study. This suggests that the findings, while statistically significant, may not reach the threshold for clinical significance for most donors. Nevertheless, the strength of the association was particularly notable, and this knowledge may be of particular interest for people with compromised corneal endothelium, for whom cell density is under 1000 cells/mm^2, and who are seeking specific strategies to maintain as much clarity of the cornea as possible. Further research will be needed to determine if certain individuals are more susceptible to alcohol-associated ECD loss.

Given the multiple comparisons made, we applied a strict threshold for statistical significance. While this more conservative estimate allows the observer to have confidence in the associations identified, it reduces statistical power and increases the

likelihood of type II error. Therefore, it is possible that some true associations may not be recognized. Several associations demonstrated a p-value between 0.0083 and 0.05; we interpret these as trends worthy of investigation with additional datasets. Moreover, we were unable to quantify tobacco use and future work could investigate this phenomenon.

In this study, the proportion of specular microscopy images analyzed by counting at least 100 cells was less than half, with the majority of images analyzed by counting 50-99 cells. To rule out the possibility that the findings in the study were affected by the number of cells counted, we conducted two post-hoc analyses of ECD, one analysis adjusting for the cells counted and a second analysis stratified for those donors whose images averaged 100 cells counted per image across both eyes. The results appear in Supplemental Data 3 and demonstrate the persistent association with alcohol in both analyses.

In summary, data from this large set of corneal endothelial images from an eye bank point to significant changes in endothelial cell density and morphology associated with heavy alcohol use, a strong association maintained even when comorbidities are taken into account.

Chapter 5

Conclusion

In this dissertation, we addressed some of the challenges faced by the eye banking professionals and proposed solutions to mitigate them. Chapter 1 introduced human cornea, importance of corneal evaluation, and eye banking in general. In addition to that, chapter 1 surveyed the literature. Corneal evaluation plays a major role in eye banking. Due to the current unavailability of reliable automatic software, technicians still use manual method to evaluate the corneal endothelium health.

Chapter 2 proposed a classical image processing based algorithm for analysis of specular microscopy images that is both efficient and accurate. The algorithm was tested on a dataset of 303 images and achieved an accuracy of 6.95%, which was compared to other state-of-the-art techniques. The algorithm was found to be superior in its ability to determine ECD, the parameter most often sought by clinicians, and was not biased by training on a specific dataset. However, the study did not compare the algorithm's ability to determine ECD in the setting of specific pathologies. Another limitation of this algorithm was poor performance on the morphological parameters such as CV and HEX.

Overall, the proposed algorithm offers a promising method to estimate ECD in specular microscopy images with opacities of varying illumination and evidence of strong correlation with manual analysis. The algorithm's ability to balance efficiency and accuracy makes it a potentially useful tool in clinical settings, where technicians often face a tradeoff between the two. However, further experimentation and testing will

be needed to determine the extent to which the algorithm is valid across different microscopes and in different pathological settings.

Chapter 3 extends the work from Chapter 2 and presented a deep learning-based corneal endothelial cell segmentation technique that utilizes a hybrid approach combining classical image processing with deep learning. The proposed Mobile-CellNet architecture was compared with benchmark manual analysis, clinical analysis using Flex-Center, and two other deep learning techniques, UNet and UNet++. While U-Net had the highest accuracy, one-way ANOVA test showed that there was no significant difference in cell density between U-Net and Mobile-CellNet. However, Mobile-CellNet was found to be more efficient as it required significantly fewer parameters and FLOPs than UNet and UNet++. Furthermore, the proposed technique produced mean errors below the acceptable threshold compared to manual inter-rater technicians' reliability.

The study also measured and identified the effectiveness of the RoI extractor and found that Mobile-CellNet produced an acceptable MAE of 4.08% with a correlation coefficient of 0.94. However, it was observed that the technique suffered from minor under-segmentation, which needs to be addressed in future work.

Overall, the proposed technique significantly reduced the time and resource-consuming manual count by automating the cell segmentation and counting process.

The Mobile-CellNet architecture, with its lower computational requirements and efficient segmentation, could be utilized in low-resource embedded computing devices. The study's findings suggest that this technique has potential for wider adoption in the clinical setting and could aid in more accurate diagnosis and treatment planning for other medical segmentation problems as well. We explore them in Chapter 5 and Chapter 6.

In addition to corneal endothelial cell density, medical history of the donors play a crucial role in determining whether a tissue can be used for transplant or not. Chapter 4 provided valuable insights into the effect of heavy alcohol use on the corneal endothelium, with quantitative and qualitative changes observed even after adjusting for additional factors. The study confirms the association between heavy alcohol use and endothelial cell density loss and highlights the importance of considering alcohol abuse as a potential comorbidity when studying the effects of other clinical variables on corneal endothelial health. The study also suggests that changes occur in hexagonality and the coefficient of variation with heavy alcohol use, which are of particular importance as they are associated with cell stress and corneal decompensation.

Further research is needed to understand the specific pathological changes that take place in the setting of heavy alcohol use, and whether there is a difference in endothelial cell morphology between patients with varying histories of alcohol dependence. The study's estimated effect of alcohol abuse on ECD was modest, but the strength

of the association was particularly notable, and this knowledge may be of particular interest for people with compromised corneal endothelium.

However, the study's multiple comparisons and conservative threshold for statistical significance may reduce statistical power and increase the likelihood of type II error. The study also has limitations in terms of the number of cells counted, and future work could investigate the effects of tobacco use.

5.1 Future Scope

The proposed algorithm offers a promising method for estimating ECD in specular microscopy images with varying illumination. However, the algorithm's ability to determine ECD in the setting of specific pathologies was not assessed, and future studies may be needed to assess this. While Mobile-CellNet architecture does a better job in terms of accuracy and robustness, future work could include images with varying pathologies. Additionally, the efficiency of the model, Mobile-CellNet needs to be tested on ARM processors in absence of GPU to test its run-time and efficiency. Finally, all the images used in this research were collected at clinical settings from live patients. Images of the donor cornea, while looks similar, uses different imaging techniques that makes the images look different. Future work needs to be performed in training the models on eye bank images to test the performance.

While this paper provides valuable insights into the effect of heavy alcohol use on the corneal endothelium, there are many other factors that may have effects on the corneal endothelial cell density. Some of these were tested on the available dataset (see Appendix). Future work will require further analysis. In addition to that, running the same experiments using the dataset from other eye banks across the country will solidify the findings of this study.

Finally, while this research focuses on developing AI tools to improve the eye banking system, it only analyzes specular endothelial images. Eye banking involves multiple imaging modalities such as slit-lamp imaging and optical coherence tomography (OCT). Multi-modal image analysis, along with a patient's medical history, can provide better understanding and help make the eye banking system more efficient. Therefore, future research should focus on developing AI tools that can analyze different imaging modalities and patient information to improve the eye banking system's efficacy.

References

[1] Karmakar, R.; Nooshabadi, S.; Eghrari, A. *Graefe's Archive for Clinical and Experimental Ophthalmology* **2021**, pages 1–10.

[2] Fan, D.-P.; Ji, G.-P.; Zhou, T.; Chen, G.; Fu, H.; Shen, J.; Shao, L. In *International Conference on Medical Image Computing and Computer-Assisted Intervention*, pages 263–273. Springer, 2020.

[3] Artificial intelligence: The big questions. November **2021**.

[4] Artificial intelligence and machine learning (ai/ml)-enabled medical devices. October **2022**.

[5] Sherif, N. A.; Chew, E. Y.; Chiang, M. F.; Hribar, M.; Gao, J.; Goetz, K. E. *Current opinion in ophthalmology* **2022**, *33*(6), 579–584.

[6] Safi, T.; Daas, L.; Kiefer, G.-L.; Nadig, M.; Sharma, M.; Sakha, M. M.; Ndiaye, A.; Deru, M.; Alexandersson, J.; Seitz, B. *Investigative Ophthalmology & Visual Science* **2022**, *63*(7), 2756–A0245.

[7] Ali, M.; Glasser, D.; Jeng, B. H.; Lass, J. H.; Philippy, B.; Srikumaran, D. *Ophthalmology Science* **2022**, *2*(3).

[8] Ting, D. S. W.; Pasquale, L. R.; Peng, L.; Campbell, J. P.; Lee, A. Y.; Raman, R.; Tan, G. S. W.; Schmetterer, L.; Keane, P. A.; Wong, T. Y. *British Journal of Ophthalmology* **2019**, *103*(2), 167–175.

[9] Honavar, S. G. *Indian Journal of Ophthalmology* **2022**, *70*(4), 1075.

[10] Schmidt-Erfurth, U.; Sadeghipour, A.; Gerendas, B. S.; Waldstein, S. M.; Bogunović, H. *Progress in retinal and eye research* **2018**, *67*, 1–29.

[11] Han, J.-H. *Diagnostics* **2022**, *12*(8), 1927.

[12] Nuzzi, R.; Boscia, G.; Marolo, P.; Ricardi, F. *Frontiers in Medicine* **2021**, *8*, 710329.

[13] Bellemo, V.; Lim, G.; Rim, T. H.; Tan, G. S.; Cheung, C. Y.; Sadda, S.; He, M.-g.; Tufail, A.; Lee, M. L.; Hsu, W.; others. *Current Diabetes Reports* **2019**, *19*, 1–12.

[14] Lambert, N. G.; Chamberlain, W. D. *J Biorepository Sci App Med* **2017**, *5*, 23–40.

[15] Naik, N.; Hameed, B.; Shetty, D. K.; Swain, D.; Shah, M.; Paul, R.; Aggarwal, K.; Ibrahim, S.; Patil, V.; Smriti, K.; others. *Frontiers in surgery* **2022**, page 266.

[16] Gerke, S.; Minssen, T.; Cohen, G. In *Artificial intelligence in healthcare;* Elsevier, 2020; pages 295–336.

[17] Abdullah, Y. I.; Schuman, J. S.; Shabsigh, R.; Caplan, A.; Al-Aswad, L. A. *Asia-Pacific journal of ophthalmology (Philadelphia, Pa.)* **2021**, *10*(3), 289.

[18] Rao, G. N.; Gopinathan, U. *Community eye health* **2009**, *22*(71), 46.

[19] 2020 eye banking statistical report. of America, E. B. A. **2021**.

[20] 2021 eye banking statistical report. of America, E. B. A. **2022**.

[21] Milliman research report 2020 us organ and tissue transplants: Cost estimates, discussion, and emerging issues. January **2020**.

[22] Tuft, S.; Coster, D. *Eye* **1990**, *4*(3), 389–424.

[23] Bourne, W. *Eye* **2003**, *17*(8), 912–918.

[24] Jeang, L. J.; Margo, C. E.; Espana, E. M. *Experimental eye research* **2021**, *205*, 108495.

[25] Dystrophia epithelialis corneae. Fuchs, E. **1910**.

[26] Adamis, A. P.; Filatov, V.; Tripathi, B. J.; others. *Survey of ophthalmology* **1993**, *38*(2), 149–168.

[27] Maghsoudlou, P.; Sood, G.; Akhondi, H. **2019**.

[28] Tan, D. T.; Dart, J. K.; Holland, E. J.; Kinoshita, S. *The Lancet* **2012**, *379*(9827), 1749–1761.

[29] Gorovoy, M. S. *Cornea* **2006**, *25*(8), 886–889.

[30] Maier, P.; Reinhard, T.; Cursiefen, C. *Deutsches Ärzteblatt International* **2013**, *110*(21), 365.

[31] Avetisov, S.; Bubnova, I.; Antonov, A. *Vestnik oftalmologii* **2010**, *126*(6), 3–7.

[32] Ambrósio Jr, R.; Nogueira, L. P.; Caldas, D. L.; Fontes, B. M.; Luz, A.; Cazal, J. O.; Alves, M. R.; Belin, M. W. *International ophthalmology clinics* **2011**, *51*(2), 11–38.

[33] Huang, J.; Maram, J.; Tepelus, T. C.; Sadda, S. R.; Chopra, V.; Lee, O. L. *Eye & contact lens* **2018**, *44*, S144–S150.

[34] McCarey, B. E.; Edelhauser, H. F.; Lynn, M. J. *Cornea* **2008**, *27*(1), 1.

[35] Patel, S. V.; McLaren, J. W.; Bachman, L. A.; Bourne, W. M. *Cornea* **2010**, *29*(9), 1042–1047.

[36] Villalba, R.; Jiménez, A.; Fornes, G.; Eisman, M.; Villagran, J. *Cell and tissue banking* **2014**, *15*(4), 507–512.

[37] Vincent, L. M.; Masters, B. R. In *Image Algebra and Morphological Image Processing III*, Vol. 1769, pages 212–226. SPIE, 1992.

[38] Fabijańska, A. *Biomedical Signal Processing and Control* **2019**, *47*, 145–158.

[39] Selig, B.; Vermeer, K. A.; Rieger, B.; Hillenaar, T.; Luengo Hendriks, C. L. *BMC medical imaging* **2015**, *15*(1), 1–15.

[40] Charłampowicz, K.; Reska, D.; Bołdak, C. *Advances In Computer Science Research* **2014**, (11), 47–60.

[41] Dagher, I.; El Tom, K. *Image and Vision Computing* **2008**, *26*(7), 905–912.

[42] Foracchia, M.; Ruggeri, A. In *Proceedings of the Second Joint 24th Annual Conference and the Annual Fall Meeting of the Biomedical Engineering Society][Engineering in Medicine and Biology*, Vol. 2, pages 1097–1098. IEEE, 2002.

[43] Foracchia, M.; Ruggeri, A. In *Proceedings of the 25th Annual International Conference of the IEEE Engineering in Medicine and Biology Society (IEEE Cat. No.03CH37439)*, Vol. 1, pages 794–797 Vol.1, 2003.

[44] Foracchia, M.; Ruggeri, A. In *2007 29th Annual International Conference of the IEEE Engineering in Medicine and Biology Society*, pages 6035–6038. IEEE, 2007.

[45] Zhou, Y.; Heise, B. 2007.

[46] Gavet, Y.; Pinoli, J.-C. *Image Analysis & Stereology* **2008**, *27*(1), 53–61.

[47] Piórkowski, A.; Gronkowska-Serafin, J. In *International Conference on Bioinformatics and Biomedical Engineering*, pages 240–249. Springer, 2015.

[48] Scarpa, F.; Ruggeri, A. In *Ophthalmic Medical Image Analysis International Workshop*, Vol. 2. University of Iowa, 2015.

[49] Salerno, M.; Sargeni, F.; Bonaiuto, V.; Amerini, P.; Cerulli, L.; Ricci, F. In *1998 Fifth IEEE International Workshop on Cellular Neural Networks and their Applications. Proceedings (Cat. No. 98TH8359)*, pages 169–174. IEEE, 1998.

[50] Nurzynska, K. In *International Conference: Beyond Databases, Architectures and Structures*, pages 323–333. Springer, 2018.

[51] Kolluru, C.; Benetz, B. A.; Joseph, N.; Menegay, H. J.; Lass, J. H.; Wilson, D. In *Medical Imaging 2019: Computer-Aided Diagnosis*, Vol. 10950, pages 1126–1135. SPIE, 2019.

[52] Badrinarayanan, V.; Kendall, A.; Cipolla, R. *IEEE transactions on pattern analysis and machine intelligence* **2017**, *39*(12), 2481–2495.

[53] Vigueras-Guillén, J. P.; van Rooij, J.; Engel, A.; Lemij, H. G.; van Vliet, L. J.; Vermeer, K. A. *Translational vision science & technology* **2020**, *9*(2), 49–49.

[54] Daniel, M. C.; Atzrodt, L.; Bucher, F.; Wacker, K.; Böhringer, S.; Reinhard, T.; Böhringer, D. *Scientific reports* **2019**, *9*(1), 1–7.

[55] Sierra, J. S.; Pineda, J.; Viteri, E.; Rueda, D.; Tibaduiza, B.; Berrospi, R. D.; Tello, A.; Galvis, V.; Volpe, G.; Millán, M. S.; others. In *Applications of Machine Learning 2020*, Vol. 11511, pages 59–64. SPIE, 2020.

[56] Shilpashree, P. S.; Suresh, K. V.; Sudhir, R. R.; Srinivas, S. P. *Translational Vision Science & Technology* **2021**, *10*(13), 27–27.

[57] Kumar, K. K.; Srinivasa, G. In *2018 Second International Conference on Advances in Electronics, Computers and Communications (ICAECC)*, pages 1–7. IEEE, 2018.

[58] Schultz, R. O.; Matsuda, M.; Yee, R. W.; Edelhauser, H. F.; Schultz, K. J. *American Journal of Ophthalmology* **1984**, *98*(4), 401–410.

[59] Lee, J.; Oum, B.; Choi, H.; Lee, J.; Cho, B. *Eye* **2006**, *20*(3), 315–318.

[60] Busted, N.; Olsen, T.; Schmitz, O. *British Journal of Ophthalmology* **1981**, *65*(10), 687–690.

[61] Ilhan, N.; Ilhan, O.; Coskun, M.; Daglioglu, M. C.; Ayhan Tuzcu, E.; Kahraman, H.; Keskin, U. *Eye & Contact Lens: Science & Clinical Practice* **2016**, *42*(5), 303–307.

[62] Frifelt, L. E. W.; Subhi, Y.; Holm, L. M.; Singh, A. *Acta Ophthalmologica* **2022**, *100*(1), 26–34.

[63] McCarey, B. E. *Ophthalmology* **1979**, *86*(10), 1848–1860.

[64] Bourne, W. M.; Nelson, L. R.; Hodge, D. O. *Investigative ophthalmology & visual science* **1997**, *38*(3), 779–782.

[65] Laing, R. A.; Sandstrom, M. M.; Berrospi, A. R.; Leibowitz, H. M. *Experimental eye research* **1976**, *22*(6), 587–594.

[66] Mohammad-Salih, P. *The Medical Journal of Malaysia* **2011**, *66*(4), 300–303.

[67] Rao, S. K.; Sen, P. R.; Fogla, R.; Gangadharan, S.; Padmanabhan, P.; Badrinath, S. *Cornea* **2000**, *19*(6), 820–823.

[68] Maurice, D. *Experientia* **1968**, *24*(11), 1094–1095.

[69] Laing, R. A.; Sandstrom, M. M.; Leibowitz, H. M. *Archives of Ophthalmology* **1975**, *93*(2), 143–145.

[70] Bourne, W. M.; Kaufman, H. E. *American journal of ophthalmology* **1976**, *81*(3), 319–323.

[71] Jalbert, I.; Stapleton, F.; Papas, E.; Sweeney, D.; Coroneo, M. *British Journal of Ophthalmology* **2003**, *87*(2), 225–236.

[72] Huang, J.; Maram, J.; Modak, C.; Sadda, S. R.; Chopra, V.; Lee, O. L. *Investigative Ophthalmology & Visual Science* **2014**, *55*(13), 999–999.

[73] Hara, M.; Morishige, N.; Chikama, T.-i.; Nishida, T. *Cornea* **2003**, *22*(6), 512–515.

[74] Price, M. O.; Fairchild, K. M.; Price Jr, F. W. *Cornea* **2013**, *32*(5), 567–573.

[75] Miyagi, H.; Stanley, A. A.; Chokshi, T. J.; Pasqualino, C. Y.; Hoehn, A. L.; Murphy, C. J.; Thomasy, S. M. *Veterinary ophthalmology* **2020**, *23*(1), 44–51.

[76] Thuret, G.; Manissolle, C.; Acquart, S.; Le Petit, J.; Maugery, J.; Campos-Guyotat, L.; Doughty, M.; Gain, P. *British journal of ophthalmology* **2003**, *87*(12), 1481–1486.

[77] Grisan, E.; Paviotti, A.; Laurenti, N.; Ruggeri, A. In *2005 IEEE Engineering in Medicine and Biology 27th Annual Conference*, pages 1700–1703. IEEE, 2006.

[78] Ruggeri, A.; Scarpa, F.; De Luca, M.; Meltendorf, C.; Schroeter, J. *British Journal of Ophthalmology* **2010**, *94*(5), 643–647.

[79] Ruggeri, A.; Grisan, E.; Jaroszewski, J. *British journal of ophthalmology* **2005**, *89*(3), 306–311.

[80] Hiroyasu, T.; Sekiya, S.; Nunokawa, S.; Koizumi, N.; Okumura, N.; Yamamoto, U. In *2013 IEEE International Conference on Systems, Man, and Cybernetics*, pages 1811–1816. IEEE, 2013.

[81] Foracchia, M.; Ruggeri, A. In *Proceedings of the 22nd Annual International Conference of the IEEE Engineering in Medicine and Biology Society (Cat. No. 00CH37143)*, Vol. 2, pages 1033–1035. IEEE, 2000.

[82] Nurzynska, K. *Symmetry* **2018**, *10*(3), 60.

[83] Vigueras-Guillén, J. P.; Sari, B.; Goes, S. F.; Lemij, H. G.; van Rooij, J.; Vermeer, K. A.; van Vliet, L. J. *BMC Biomedical Engineering* **2019**, *1*(1), 1–16.

[84] Imre, L.; Nagymihály, A. *Graefe's archive for clinical and experimental ophthalmology* **2001**, *239*(5), 356–360.

[85] Piorkowski, A.; Nurzynska, K.; Boldak, C.; Reska, D.; Gronkowska-Serafin, J. *Journal of Medical Informatics & Technologies* **2015**, *24*.

[86] Sharif, M. S.; Qahwaji, R.; Shahamatnia, E.; Alzubaidi, R.; Ipson, S.; Brahma, A. *Computer methods and programs in biomedicine* **2015**, *122*(3), 421–436.

[87] Berzins, V. *Computer Vision, Graphics, and Image Processing* **1984**, *27*(2), 195–210.

[88] Sobel, I.; Feldman, G.; others. *a talk at the Stanford Artificial Project in* **1968**, pages 271–272.

[89] Beucher, S. In *Mathematical morphology and its applications to image processing;* Springer, 1994; pages 69–76.

[90] Waring III, G. O.; Bourne, W. M.; Edelhauser, H. F.; Kenyon, K. R. *Ophthalmology* **1982**, *89*(6), 531–590.

[91] Sridhar, M. S. *Indian journal of ophthalmology* **2018**, *66*(2), 190.

[92] Whiteley, H. E.; Peiffer, R. L. In *Handbook of toxicologic pathology;* Elsevier, 2002; pages 539–584.

[93] Eghrari, A. O.; Riazuddin, S. A.; Gottsch, J. D. *Progress in molecular biology and translational science* **2015**, *134*, 7–23.

[94] Sugar, J.; Kapur, R. In *Roy and Fraunfelder's Current Ocular Therapy;* Elsevier, 2008; pages 362–363.

[95] Ronneberger, O.; Fischer, P.; Brox, T. In *International Conference on Medical image computing and computer-assisted intervention*, pages 234–241. Springer, 2015.

[96] Sandler, M.; Howard, A.; Zhu, M.; Zhmoginov, A.; Chen, L.-C. In *Proceedings of the IEEE conference on computer vision and pattern recognition*, pages 4510–4520, 2018.

[97] Kingma, D. P.; Ba, J. *arXiv preprint arXiv:1412.6980* **2014**.

[98] Zhou, Z.; Siddiquee, M.; Tajbakhsh, N.; Liang, J. U. *arXiv preprint arXiv:1807.10165*.

[99] Organization, W. H. *Global status report on alcohol and health 2018;* World Health Organization, 2019.

[100] Araujo, I.; Henriksen, A.; Gamsby, J.; Gulick, D. *Frontiers in Molecular Biosciences* **2021**, *8*, 643273.

[101] Karimi, S.; Arabi, A.; Shahraki, T. *Journal of Ophthalmic & Vision Research* **2021**, *16*(2), 260.

[102] Friedman, G. D.; Tekawa, I.; Klatsky, A. L.; Sidney, S.; Armstrong, M. A. *Drug and alcohol dependence* **1991**, *27*(3), 283–290.

[103] Sati, A.; Moulick, P.; Shankar, S.; Chatterjee, K.; Dwivedi, A. K.; Vazirani, J. *British Journal of Ophthalmology* **2018**, *102*(10), 1443–1447.

[104] Lužnik, Z.; Sun, Z.; Yin, J.; Benetz, B. A.; Lass, J. H.; Dana, R. *Journal of Biological Methods* **2019**, *6*(4).

[105] Kwon, J. W.; Cho, K. J.; Kim, H. K.; Lee, J. K.; Gore, P. K.; McCartney, M. D.; Chuck, R. S. *Cornea* **2016**, *35*(9), 1206–1210.

[106] Grütters, G.; Ritz-Timme, S.; Reichelt, J.; Nölle, B. *Der Ophthalmologe: Zeitschrift der Deutschen Ophthalmologischen Gesellschaft* **2002**, *99*(4), 266–269.

[107] Chen, Y.; Tsao, S. W.; Heo, M.; Gore, P. K.; McCarthy, M. D.; Chuck, R. S.; Channa, P. *Cornea* **2017**, *36*(3), 367.

[108] Yee, R. W.; Geroski, D. H.; Matsuda, M.; Champeau, E. J.; Meyer, L. A.; Edelhauser, H. F. *Investigative ophthalmology & visual science* **1985**, *26*(9), 1191–1201.

[109] Shannon, C. E. *The Bell system technical journal* **1948**, *27*(3), 379–423.

[110] Serra, J. *(No Title)* **1982**.

[111] Canny, J. *IEEE Transactions on pattern analysis and machine intelligence* **1986**, (6), 679–698.

[112] RINGVOLD, A.; DAVANGER, M.; OLSEN, E. G. *Acta Ophthalmologica* **1984**, *62*(6), 911–918.

[113] Zhou, Z.; Rahman Siddiquee, M. M.; Tajbakhsh, N.; Liang, J. In *Deep learning in medical image analysis and multimodal learning for clinical decision support;* Springer, 2018; pages 3–11.

[114] Karkanis, S. A.; Iakovidis, D. K.; Maroulis, D. E.; Karras, D. A.; Tzivras, M. *IEEE transactions on information technology in biomedicine* **2003**, *7*(3), 141–152.

[115] Alexandre, L. A.; Nobre, N.; Casteleiro, J. In *2008 International Conference on BioMedical Engineering and Informatics*, Vol. 2, pages 38–42. IEEE, 2008.

[116] Ameling, S.; Wirth, S.; Paulus, D.; Lacey, G.; Vilarino, F. In *Bildverarbeitung für die Medizin 2009;* Springer, 2009; pages 346–350.

[117] Cheng, D.-C.; Ting, W.-C.; Chen, Y.-F.; Jiang, X. *Biomedical Engineering: Applications, Basis and Communications* **2011**, *23*(05), 357–367.

[118] Iakovidis, D. K.; Maroulis, D. E.; Karkanis, S. A.; Brokos, A. In *18th IEEE Symposium on Computer-Based Medical Systems (CBMS'05)*, pages 575–580. IEEE, 2005.

[119] Hwang, S.; Oh, J.; Tavanapong, W.; Wong, J.; De Groen, P. C. In *2007 IEEE International Conference on Image Processing*, Vol. 2, pages II–465. IEEE, 2007.

[120] Zhu, H.; Fan, Y.; Liang, Z. In *International MICCAI Workshop on Computational Challenges and Clinical Opportunities in Virtual Colonoscopy and Abdominal Imaging*, pages 9–14. Springer, 2010.

[121] Van Wijk, C.; Van Ravesteijn, V. F.; Vos, F. M.; Van Vliet, L. J. *IEEE Transactions on Medical Imaging* **2010**, *29*(3), 688–698.

[122] Krishnan, S.; Yang, X.; Chan, K.; Kumar, S.; Goh, P. In *Proceedings of the 20th Annual International Conference of the IEEE Engineering in Medicine and Biology Society. Vol. 20 Biomedical Engineering Towards the Year 2000 and Beyond (Cat. No. 98CH36286)*, Vol. 2, pages 895–898. IEEE, 1998.

[123] Dhandra, B. V.; Hegadi, R.; Hangarge, M.; Malemath, V. S. In *18th International Conference on Pattern Recognition (ICPR'06)*, Vol. 4, pages 695–698. IEEE, 2006.

[124] Zhang, R.; Zheng, Y.; Poon, C. C.; Shen, D.; Lau, J. Y. *Pattern recognition* **2018**, *83*, 209–219.

[125] Tajbakhsh, N.; Gurudu, S. R.; Liang, J. In *2015 IEEE 12th International Symposium on Biomedical Imaging (ISBI)*, pages 79–83. IEEE, 2015.

[126] Yu, L.; Chen, H.; Dou, Q.; Qin, J.; Heng, P. A. *IEEE journal of biomedical and health informatics* **2016**, *21*(1), 65–75.

[127] Pogorelov, K.; Randel, K. R.; Griwodz, C.; Eskeland, S. L.; de Lange, T.; Johansen, D.; Spampinato, C.; Dang-Nguyen, D.-T.; Lux, M.; Schmidt, P. T.; Riegler, M.; Halvorsen, P. In *Proceedings of the 8th ACM on Multimedia Systems Conference*, MMSys'17, pages 164–169, New York, NY, USA, 2017. ACM.

[128] Vázquez, D.; Bernal, J.; Sánchez, F. J.; Fernández-Esparrach, G.; López, A. M.; Romero, A.; Drozdzal, M.; Courville, A. *Journal of healthcare engineering* **2017**, *2017*.

[129] Silva, J.; Histace, A.; Romain, O.; Dray, X.; Granado, B. *International journal of computer assisted radiology and surgery* **2014**, *9*(2), 283–293.

[130] Sun, X.; Zhang, P.; Wang, D.; Cao, Y.; Liu, B. In *2019 18th IEEE International Conference On Machine Learning And Applications (ICMLA)*, pages 851–858. IEEE, 2019.

[131] Zhou, Z.; Siddiquee, M. M. R.; Tajbakhsh, N.; Liang, J. *IEEE transactions on medical imaging* **2019**, *39*(6), 1856–1867.

[132] Li, D.; Dharmawan, D. A.; Ng, B. P.; Rahardja, S. In *2019 IEEE International Conference on Image Processing (ICIP)*, pages 1425–1429. IEEE, 2019.

[133] Khanna, A.; Londhe, N. D.; Gupta, S.; Semwal, A. *Biocybernetics and Biomedical Engineering* **2020**, *40*(3), 1314–1327.

[134] Fang, Y.; Chen, C.; Yuan, Y.; Tong, K.-y. In *International Conference on Medical Image Computing and Computer-Assisted Intervention*, pages 302–310. Springer, 2019.

[135] Huang, C.-H.; Wu, H.-Y.; Lin, Y.-L. *arXiv preprint arXiv:2101.07172* **2021**.

[136] Redmon, J.; Divvala, S.; Girshick, R.; Farhadi, A. In *Proceedings of the IEEE conference on computer vision and pattern recognition*, pages 779–788, 2016.

[137] Long, J.; Shelhamer, E.; Darrell, T. In *Proceedings of the IEEE conference on computer vision and pattern recognition*, pages 3431–3440, 2015.

[138] Dai, J.; Li, Y.; He, K.; Sun, J. *arXiv preprint arXiv:1605.06409* **2016**.

[139] Xiao, X.; Lian, S.; Luo, Z.; Li, S. In *2018 9th international conference on information technology in medicine and education (ITME)*, pages 327–331. IEEE, 2018.

[140] Seo, H.; Huang, C.; Bassenne, M.; Xiao, R.; Xing, L. *IEEE transactions on medical imaging* **2019**, *39*(5), 1316–1325.

[141] Ibtehaz, N.; Rahman, M. S. *Neural Networks* **2020**, *121*, 74–87.

[142] An update on cancer deaths in the united states. for Disease Control, C.; Prevention. **2020**.

[143] Fisher, R. A. *Annals of eugenics* **1936**, *7*(2), 179–188.

[144] Cristianini, N.; Shawe-Taylor, J.; others. *An introduction to support vector machines and other kernel-based learning methods;* Cambridge university press, 2000.

[145] TensorFlow: Large-scale machine learning on heterogeneous systems. Abadi, M.; Agarwal, A.; Barham, P.; Brevdo, E.; Chen, Z.; Citro, C.; Corrado, G. S.; Davis, A.; Dean, J.; Devin, M.; Ghemawat, S.; Goodfellow, I.; Harp, A.; Irving, G.; Isard, M.; Jia, Y.; Jozefowicz, R.; Kaiser, L.; Kudlur, M.; Levenberg, J.; Mané, D.; Monga, R.; Moore, S.; Murray, D.; Olah, C.; Schuster, M.; Shlens, J.; Steiner, B.; Sutskever, I.; Talwar, K.; Tucker, P.; Vanhoucke, V.; Vasudevan, V.; Viégas, F.; Vinyals, O.; Warden, P.; Wattenberg, M.; Wicke, M.; Yu, Y.; Zheng, X. **2015**.

[146] Howard, A. G.; Zhu, M.; Chen, B.; Kalenichenko, D.; Wang, W.; Weyand, T.; Andreetto, M.; Adam, H. *arXiv preprint arXiv:1704.04861* **2017**.

[147] He, K.; Zhang, X.; Ren, S.; Sun, J. In *Proceedings of the IEEE conference on computer vision and pattern recognition*, pages 770–778, 2016.

[148] Russakovsky, O.; Deng, J.; Su, H.; Krause, J.; Satheesh, S.; Ma, S.; Huang, Z.;

Karpathy, A.; Khosla, A.; Bernstein, M.; Berg, A. C.; Fei-Fei, L. *International Journal of Computer Vision (IJCV)* **2015**, *115*(3), 211–252.

[149] Rigamonti, R.; Sironi, A.; Lepetit, V.; Fua, P. In *Proceedings of the IEEE conference on computer vision and pattern recognition*, pages 2754–2761, 2013.

[150] Zhang, Y.; Liu, S.; Li, C.; Wang, J. *Journal of Shanghai Jiaotong University (Science)* **2021**, *26*(1), 93–102.

[151] Abadi, M.; Barham, P.; Chen, J.; Chen, Z.; Davis, A.; Dean, J.; Devin, M.; Ghemawat, S.; Irving, G.; Isard, M.; others. In *12th {USENIX} symposium on operating systems design and implementation ({OSDI} 16)*, pages 265–283, 2016.

[152] Key statistics for colorectal cancer. medical, T. A. C. S.; editorial content team. **2021**.

[153] Colorectal cancer early detection, diagnosis, and staging. medical, T. A. C. S.; editorial content team. **2020**.

[154] Jha, D.; Ali, S.; Tomar, N. K.; Johansen, H. D.; Johansen, D.; Rittscher, J.; Riegler, M. A.; Halvorsen, P. *Ieee Access* **2021**, *9*, 40496–40510.

[155] Springenberg, J. T.; Dosovitskiy, A.; Brox, T.; Riedmiller, M. *arXiv preprint arXiv:1412.6806* **2014**.

[156] Radford, A.; Metz, L.; Chintala, S. *arXiv preprint arXiv:1511.06434* **2015**.

[157] Liskowski, P.; Krawiec, K. *IEEE transactions on medical imaging* **2016**, *35*(11), 2369–2380.

[158] Orlando, J. I.; Prokofyeva, E.; Blaschko, M. B. *IEEE transactions on Biomedical Engineering* **2016**, *64*(1), 16–27.

[159] Yan, Z.; Yang, X.; Cheng, K.-T. *IEEE Transactions on Biomedical Engineering* **2018**, *65*(9), 1912–1923.

[160] Wu, Y.; Xia, Y.; Song, Y.; Zhang, Y.; Cai, W. In *International Conference on Medical Image Computing and Computer-Assisted Intervention*, pages 119–126. Springer, 2018.

[161] Wang, B.; Qiu, S.; He, H. In *International Conference on Medical Image Computing and Computer-Assisted Intervention*, pages 84–92. Springer, 2019.

[162] Wu, Y.; Xia, Y.; Song, Y.; Zhang, D.; Liu, D.; Zhang, C.; Cai, W. In *International Conference on Medical Image Computing and Computer-Assisted Intervention*, pages 264–272. Springer, 2019.

[163] Zhang, S.; Fu, H.; Yan, Y.; Zhang, Y.; Wu, Q.; Yang, M.; Tan, M.; Xu, Y. In *International Conference on Medical Image Computing and Computer-Assisted Intervention*, pages 797–805. Springer, 2019.

[164] Laibacher, T.; Weyde, T.; Jalali, S. In *Proceedings of the IEEE/CVF Conference on Computer Vision and Pattern Recognition Workshops*, pages 0–0, 2019.

[165] Niemeijer, M.; Staal, J.; Ginneken, B.; Loog, M.; Abramoff, M. *Methods for evaluating segmentation and indexing techniques dedicated to retinal ophthalmology* **2004**.

[166] Fraz, M. M.; Remagnino, P.; Hoppe, A.; Uyyanonvara, B.; Rudnicka, A. R.; Owen, C. G.; Barman, S. A. Sep. **2012**, *59*(9), 2538–2548.

[167] Guo, C.; Szemenyei, M.; Yi, Y.; Wang, W.; Chen, B.; Fan, C. *arXiv preprint arXiv:2004.03696* **2020**.

[168] Romera, E.; Alvarez, J. M.; Bergasa, L. M.; Arroyo, R. *IEEE Transactions on Intelligent Transportation Systems* **2017**, *19*(1), 263–272.

[169] Labib, B. A.; Gurwood, A. S.; Meagher, A. L. *Review of Optometry* **2017**, *154*(2), 78–84.

[170] Miri, M. S.; Mahloojifar, A. *IEEE Transactions on Biomedical Engineering* **2010**, *58*(5), 1183–1192.

[171] Mendonca, A. M.; Campilho, A. *IEEE transactions on medical imaging* **2006**, *25*(9), 1200–1213.

[172] Sun, K.; Chen, Z.; Jiang, S.; Wang, Y. *Journal of medical systems* **2011**, *35*(5), 811–824.

[173] Zhou, L.; Rzeszotarski, M. S.; Singerman, L. J.; Chokreff, J. M. *IEEE transactions on medical imaging* **1994**, *13*(4), 619–626.

[174] Quek, F. K.; Kirbas, C. *IEEE transactions on Medical Imaging* **2001**, *20*(2), 117–131.

[175] Chutatape, O.; Zheng, L.; Krishnan, S. M. In *Proceedings of the 20th Annual International Conference of the IEEE Engineering in Medicine and Biology Society. Vol. 20 Biomedical Engineering Towards the Year 2000 and Beyond (Cat. No. 98CH36286)*, Vol. 6, pages 3144–3149. IEEE, 1998.

[176] Soares, J.; Leandro, J.; Cesar, R.; Jelinek, H.; Cree, M. *IEEE Transactions on Medical Imaging* **2006**, *25*(9), 1214–1222.

[177] Sinthanayothin, C.; Boyce, J. F.; Cook, H. L.; Williamson, T. H. *British journal of ophthalmology* **1999**, *83*(8), 902–910.

[178] Lupascu, C. A.; Tegolo, D.; Trucco, E. *IEEE Transactions on Information Technology in Biomedicine* **2010**, *14*(5), 1267–1274.

[179] You, X.; Peng, Q.; Yuan, Y.; Cheung, Y.-m.; Lei, J. *Pattern recognition* **2011**, *44*(10-11), 2314–2324.

[180] OSAREH, A.; Shadgar, B. **2009**.

[181] Lv, Y.; Ma, H.; Li, J.; Liu, S. *IEEE Access* **2020**, *8*, 32826–32839.

[182] Keras. Chollet, F.; others. **2015**.

[183] Liu, S.; Silverman, M. *IT Professional* **2001**, *3*(1), 27–32.

[184] Zhang, Z.; Liu, Q.; Wang, Y. *IEEE Geoscience and Remote Sensing Letters* **2018**, *15*(5), 749–753.

[185] Alom, M. Z.; Hasan, M.; Yakopcic, C.; Taha, T. M.; Asari, V. K. *arXiv preprint arXiv:1802.06955* **2018**.

[186] Li, X.; Chen, H.; Qi, X.; Dou, Q.; Fu, C.-W.; Heng, P.-A. *IEEE transactions on medical imaging* **2018**, *37*(12), 2663–2674.

[187] Cai, S.; Tian, Y.; Lui, H.; Zeng, H.; Wu, Y.; Chen, G. *Quantitative imaging in medicine and surgery* **2020**, *10*(6), 1275.

[188] Pravitasari, A. A.; Iriawan, N.; Almuhayar, M.; Azmi, T.; Fithriasari, K.; Purnami, S. W.; Ferriastuti, W.; others. *Telkomnika* **2020**, *18*(3), 1310–1318.

[189] Woo, S.; Park, J.; Lee, J.-Y.; Kweon, I. S. In *Proceedings of the European conference on computer vision (ECCV)*, pages 3–19, 2018.

[190] Bendaoudi, H.; Cheriet, F.; Manraj, A.; Tahar, H. B.; Langlois, J. P. *Journal of Real-Time Image Processing* **2018**, *15*(1), 31–42.

[191] Marín, D.; Aquino, A.; Gegúndez-Arias, M. E.; Bravo, J. M. *IEEE transactions on medical imaging* **2010**, *30*(1), 146–158.

[192] Nugroho, H. A.; Oktoeberza, W. K.; Erasari, A.; Utami, A.; Cahyono, C. In *2017 9th International Conference on Information Technology and Electrical Engineering (ICITEE)*, pages 1–5. IEEE, 2017.

[193] Al-Bander, B.; Williams, B. M.; Al-Nuaimy, W.; Al-Taee, M. A.; Pratt, H.; Zheng, Y. *Symmetry* **2018**, *10*(4), 87.

[194] Septiarini, A.; Harjoko, A.; Pulungan, R.; Ekantini, R. *Signal, Image and Video Processing* **2017**, *11*(5), 945–952.

[195] Khalid, N. E. A.; Noor, N. M.; Ariff, N. M. *Procedia Computer Science* **2014**, *42*, 255–262.

[196] Abdullah, M.; Fraz, M. M.; Barman, S. A. *PeerJ* **2016**, *4*, e2003.

[197] Cheng, J.; Liu, J.; Xu, Y.; Yin, F.; Wong, D. W. K.; Tan, N.-M.; Tao, D.; Cheng, C.-Y.; Aung, T.; Wong, T. Y. *IEEE transactions on medical imaging* **2013**, *32*(6), 1019–1032.

[198] Ayub, J.; Ahmad, J.; Muhammad, J.; Aziz, L.; Ayub, S.; Akram, U.; Basit, I. In *2016 international conference on computing, electronic and electrical engineering (ICE Cube)*, pages 143–147. IEEE, 2016.

[199] Arumugam, G.; Nivedha, S. *International Journal of Emerging Trends & Technology in Computer Science* **2013**, *2*(6), 246–251.

[200] Sigut, J.; Nunez, O.; Fumero, F.; Gonzalez, M.; Arnay, R. *PeerJ* **2017**, *5*, e3763.

[201] Pallawala, P.; Hsu, W.; Lee, M. L.; Eong, K.-G. A. In *European conference on computer vision*, pages 139–151. Springer, 2004.

[202] Ali, R.; Sheng, B.; Li, P.; Chen, Y.; Li, H.; Yang, P.; Jung, Y.; Kim, J.; Chen, C. P. *IEEE Transactions on Industrial Informatics* **2020**, *17*(4), 2476–2487.

[203] Fu, H.; Cheng, J.; Xu, Y.; Wong, D. W. K.; Liu, J.; Cao, X. *IEEE transactions on medical imaging* **2018**, *37*(7), 1597–1605.

[204] Lin, J.-W.; Liao, X.-W.; Yu, L.; Pan, J.-S. *Journal of Computers* **2020**, *31*(3), 183–194.

[205] Sevastopolsky, A. *Pattern Recognition and Image Analysis* **2017**, *27*(3), 618–624.

[206] Bourne, R. R.; Taylor, H. R.; Flaxman, S. R.; Keeffe, J.; Leasher, J.; Naidoo, K.; Pesudovs, K.; White, R. A.; Wong, T. Y.; Resnikoff, S.; others. *PloS one* **2016**, *11*(10), e0162229.

[207] Tatham, A. J.; Weinreb, R. N.; Medeiros, F. A. *Clinical Ophthalmology (Auckland, NZ)* **2014**, *8*, 611.

[208] Fu, H.; Xu, Y.; Wong, D. W. K.; Liu, J. In *2016 IEEE 13th international symposium on biomedical imaging (ISBI)*, pages 698–701. IEEE, 2016.

[209] Maninis, K.-K.; Pont-Tuset, J.; Arbeláez, P.; Van Gool, L. In *Medical Image Computing and Computer-Assisted Intervention–MICCAI 2016: 19th International Conference, Athens, Greece, October 17-21, 2016, Proceedings, Part II 19*, pages 140–148. Springer, 2016.

[210] Gu, Z.; Cheng, J.; Fu, H.; Zhou, K.; Hao, H.; Zhao, Y.; Zhang, T.; Gao, S.; Liu, J. *IEEE transactions on medical imaging* **2019**, *38*(10), 2281–2292.

[211] Mou, L.; Chen, L.; Cheng, J.; Gu, Z.; Zhao, Y.; Liu, J. *IEEE transactions on medical imaging* **2019**, *39*(5), 1392–1403.

[212] Galdran, A.; Anjos, A.; Dolz, J.; Chakor, H.; Lombaert, H.; Ayed, I. B. *Scientific Reports* **2022**, *12*(1), 6174.

[213] Fraz, M. M.; Remagnino, P.; Hoppe, A.; Uyyanonvara, B.; Rudnicka, A. R.; Owen, C. G.; Barman, S. A. *IEEE Transactions on Biomedical Engineering* **2012**, *59*(9), 2538–2548.

[214] Karmakar, R.; Nooshabadi, S.; Eghrari, A. *Graefe's Archive for Clinical and Experimental Ophthalmology* **2022**, *260*(4), 1215–1224.

[215] Niemeijer, M.; Staal, J.; Van Ginneken, B.; Loog, M.; Abramoff, M. D. In *Medical imaging 2004: image processing*, Vol. 5370, pages 648–656. SPIE, 2004.

Appendix A

Mobile-PolypNet : Light-weight Colon Polyp Segmentation Network for Low Resources Settings

Authors: *Ranit Karmakar, Saeid Nooshabadi* [1]

[1]Karmakar, R. and Nooshabadi, S., 2022. Mobile-PolypNet: Lightweight Colon Polyp Segmentation Network for Low-Resource Settings. Journal of imaging, 8(6), p.169.

A.1 Abstract

Colon polyps, a small clumps of cells on the lining of the colon, can lead to colorectal cancer (CRC), one of the leading types of cancer globally. Hence, early detection of these polyps automatically is crucial in the prevention of CRC. The deep learning models proposed for the detection and segmentation of colorectal polyps are resource-consuming. This paper proposes a lightweight deep-learning model for colorectal polyp segmentation that achieved state-of-the-art accuracy while significantly reducing the model size and complexity. The proposed deep learning autoencoder model employs a set of state-of-the-art architectural blocks and optimization objective functions to achieve the desired efficiency. The model is trained and tested on five publicly available colorectal polyp segmentation datasets (CVC-ClinicDB, CVC-ColonDB, EndoScene, Kvasir, and ETIS). We also performed ablation testing on the model to test various aspects of the autoencoder architecture. We performed the model evaluation by using most of the common image-segmentation metrics. The backbone model achieved a DICE score of 0.935 on the Kvasir dataset and 0.945 on the CVC-ClinicDB dataset, improving the accuracy by 4.12% and 5.12%, respectively, over the current state-of-the-art network, while using 88 times fewer parameters, 40 times less storage space, and being computationally 17 times more efficient. Our ablation study showed that the addition of ConvSkip in the autoencoder slightly improves the model's performance but it was not significant (p-value = 0.815).

A.2 Introduction

Colorectal cancer (CRC) is the third leading type of cancer globally, and the second principal cause of cancer-related death in the United States [142]. Approximately 4% of the female and 4.3% of the male population in the United States [152] suffer from colorectal cancer. However, with early detection and proper treatment, 90% of the patients have an increased life span of more than five years [153].

Over the years, different traditional image processing and deep learning networks have been proposed. Although deep learning models outperformed classical image processing [2], they require high computing resources, typically expressed as a frames-per-second (FPS) processing rate (a platform-dependent metric), or the number of floating-point operations (FLOPs) that network executes in order to achieve the task.

This paper develops a deep learning model that produces highly accurate segmentation while being extremely low in resource consumption. This allows the development of image-segmentation tools that could be run on mobile devices in remote locations or in resource-limited settings for medical applications.

This paper presents a novel lightweight image-segmentation architecture that is significantly less complex, requiring a fraction of training parameters and a lower number of FLOPs. By using the bottleneck residual blocks on the U-Net [95] backbone, the

model was able to achieve a significant reduction in complexity while maintaining high accuracy. The model achieved state-of-the-art performance on the test dataset. The significance of this work is in its novel encoder–decoder architecture backbone that is lightweight and suitable for deployment on mobile devices. We adopted DICE coefficient as objective loss function, which yields more accurate results. We used the same training and testing sets as the current state-of-the-art network, PraNet [2], and performed extensive testing by using important semantic segmentation metrics for better benchmarking.

A.3 Related Work

A.3.1 Traditional image processing techniques:

Early works in polyp segmentation proposed the use of handcrafted features. These works mainly focused on two aspects of CRC polyps, shape-based features, and texture or color-based features. The works on shape-based features detection include edge detection, morphological operations, and shape curvature fitting [119, 120, 121]. The work on texture-based includes color wavelet covariance (CWC)[114], discrete wavelet transform (DWT), local binary pattern (LBP) [115], gray level co-occurrence matrix (GLCM) [116] or different combination of these as descriptors [118]. These

feature descriptors are then classified using different classification methods such as linear discriminant analysis (LDA) or support vector machine (SVM).

A.3.2 CNN based methods:

In recent years, different deep learning methods have been proposed. Based on the output labels, these networks can be classified into detection and localization type networks, and semantic segmentation type networks.

A.3.2.1 Localization of colonal polyp:

The work in [125] proposed a network that first extracts three different types of handcrafted features *viz.* color, shape and temporal. It, next, used three different convolutional networks to process features to make binary decision based on the summation of the output of these networks. Other works [124, 126] on detection and localization have explored widely used architectures such as fully convolutional network (FCN) [137], and you-only-look-once (YOLO).

A.3.2.2 Semantic segmentation of colon polyp:

Semantic segmentation has emerged as a preferred technique over localization as it provides more precise information about the polyp, such as its size and shape. Access to multiple publicly available datasets [127, 128, 129] have facilitated the related investigations. The work in [95] proposed an effective deep learning architecture for biomedical image segmentation that utilizes data augmentation to produce semantic segments. Later works such as residual UNet [132], Unet++ [131] and other network [139, 140, 141] have been proposed for semantic segmentation tasks and tested for polyp segmentation. By proposing deeper networks, these works were able to achieve higher accuracy. However, the high accuracy came at a cost – large model size and computational complexity. SFANet [134] introduced a cascade network that utilizes a single encoder block and subsequently uses separate decoder blocks for boundary and area segmentation. Finally, it uses a lighter UNet for the final output. PraNet [2], took a different approach from the encoder-decoder structure and introduced a novel architecture that first predicts the coarse region and then models the boundaries for the final segmentation. The model's performance has been tested on five different datasets and achieved good performance with high generalizability. However, the model complexity is high, especially for deployment for resource-limited mobile devices.

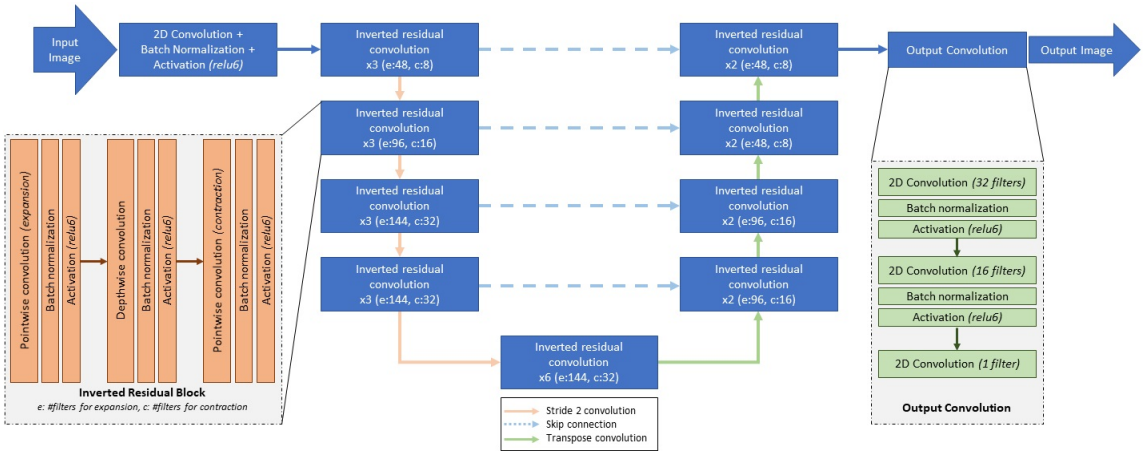

Figure A.1: Mobile-PolypNet model backbone architecture with the bottleneck residual blocks and skip connection where x, e and c in each residual block represent the number of bottleneck residual blocks in each resolution level, number of filters for expansion phase, and number of filters for the contraction phase, respectively.

A.4 Methods

A.4.1 Network architecture

Our autoencoder model, Mobile-PolypNet [2] (Figure A.1), uses a similar design philosophy as the original UNet. However, Mobile-PolypNet is significantly different from UNet in its building blocks. The original UNet, employs the traditional convolution layer as building block. Mobile-PolypNet, instead, uses bottleneck residual blocks with depthwise and pointwise separable filters [96]. The building blocks in

[2] `https://github.com/rkarmaka/Mobile-PolypNet`

Mobile-PolypNet have been architectured for the single purpose of significant reduction in computational complexity, memory footprint, while maintaining similar level of accuracy reported by the state-of-the-art networks.

A.4.1.1 Input layer

In Mobile-PolypNet, the input image is first processed using a traditional convolution layer with 32 filters followed by a depthwise convolution and a pointwise convolution. Batch normalization and Relu6 activation is used after each convolution layer except for the last pointwise convolution layer where a linear activation is used. All the depthwise convolution layers used 3×3 convolution.

A.4.1.2 Encoder

On each image resolution level Mobile-PolypNet uses three bottleneck inverted residual blocks [96] (see the insert box on the left side of Figure A.1). The inverted residual blocks contrary to the commonly used residual block, first expands the compressed feature map representation to higher dimension, filter it with efficient depthwise convolution [149], and then projects it back to a low-dimensional feature map representation. Stride-2 convolution is used on the first bottleneck residual block to reduce the image dimensions (height and width) by half. Number of expansion filters used

in five resolution levels are 48, 96, 144, 144, 144. We used a contraction factor of 6 for the first 2 levels and 4.5 for the last 3 levels. Also note that each inverted residual block has its own skip connection.

A.4.1.3 Decoder

Similar to encoder, the decoder in Mobile-PolypNet uses the bottleneck residual blocks. We use traditional transpose convolution to double the image resolution. Each resolution level contains two bottleneck residual blocks with 96 layers for bottom two levels and 48 for the top two levels. A contraction factor of 6 was used throughout the decoding path.

A.4.1.4 Output layer

The final output from the decoder has eight channels. Rather than directly reducing it down to one channel, we processed the image further using two traditional convolution layers. First we expanded the image using 32 filters and then reduced it to 16, and finally to one channel. Each convolution operation was followed by a batch normalization and activation ($ReLu6$) except for the output layer which uses sigmoid activation without batch normalization.

A.4.2 Network Training

A.4.2.1 Loss function:

Binary cross-entropy loss, used in UNet, is a standard loss function for semantic segmentation. Although it works well in certain applications, blob segmentation tasks such as polyp segmentation do not give enough global information about the segmented area, making the training difficult. Instead, we have used a negative "Dice" score to evaluate the training loss.

$$L_{Dice} = \frac{2\sum_i^N p_i g_i}{\sum_i^N p_i^2 + \sum_i^N g_i^2} \tag{A.1}$$

where p is the predicted label and g is the ground truth label.

A.4.2.2 Training setup:

All models discussed in this paper have been implemented in TensorFlow with support for graphical processing units (GPU). We have used a platform with NVIDIA GTX 1060 6GB GPU. Input and output both have a size of 224×224. We also used Adam optimizer [97] with a learning rate of $1e-3$. The batch size was limited by the

available hardware resources and was set to 8, amounting to 979 batches per epoch. After each iteration best model was stored, and the training was stopped when the validation Dice score did not improve after 25 epochs.

A.4.3 Statistical analysis

To compare the similarity and differences between the two results, we performed two-tailed *t-test*. Statistical analysis of the results was performed in Python using the SciPy library. We used $\alpha = 0.05$ as our cut-off value for significance testing.

A.5 Experiments

A.5.1 Dataset and image preparation

We used the same datasets as the current state-of-the-art model PraNet which reported a significant increase in performance compared to the other available models. Choice of datasets allowed us to do better benchmarking. The training dataset contains 1450 images, with 900 images from the Kvasir dataset and 550 from the CVC-ClinicDB. For the training, we applied data augmentation to achieve a five-fold increase in the size of the dataset; four random rotations between $-90°$ and $90°$, and

one Gaussian blurring. Test images, however, were only resized. Our final training set had 8700 images. For testing, we used hold-out test sets from Kvasir and CVC-ClinicDB, considered as seen, along with CVC-300, CVC-ColonDB, and ETIS, considered as unseen. All the images in the training set and the test set were resized to 224×224 for uniformity.

A.5.2 Settings for the training and performance metrics

For training and validation, we divided the datasets into 90% for training and 10% for validation. We used the validation set to monitor for overfitting. For the model's performance metrics, we have used the Dice coefficient, mean intersection over union (mIoU), mean absolute error (MAE), and F_β. We have avoided using frames per second (FPS) as the performance measure as it is a platform-dependent measure. Instead, we used the platform-independent measure, the number of floating-point operations (FLOPs) per image prediction, to measure the model's computational efficiency.

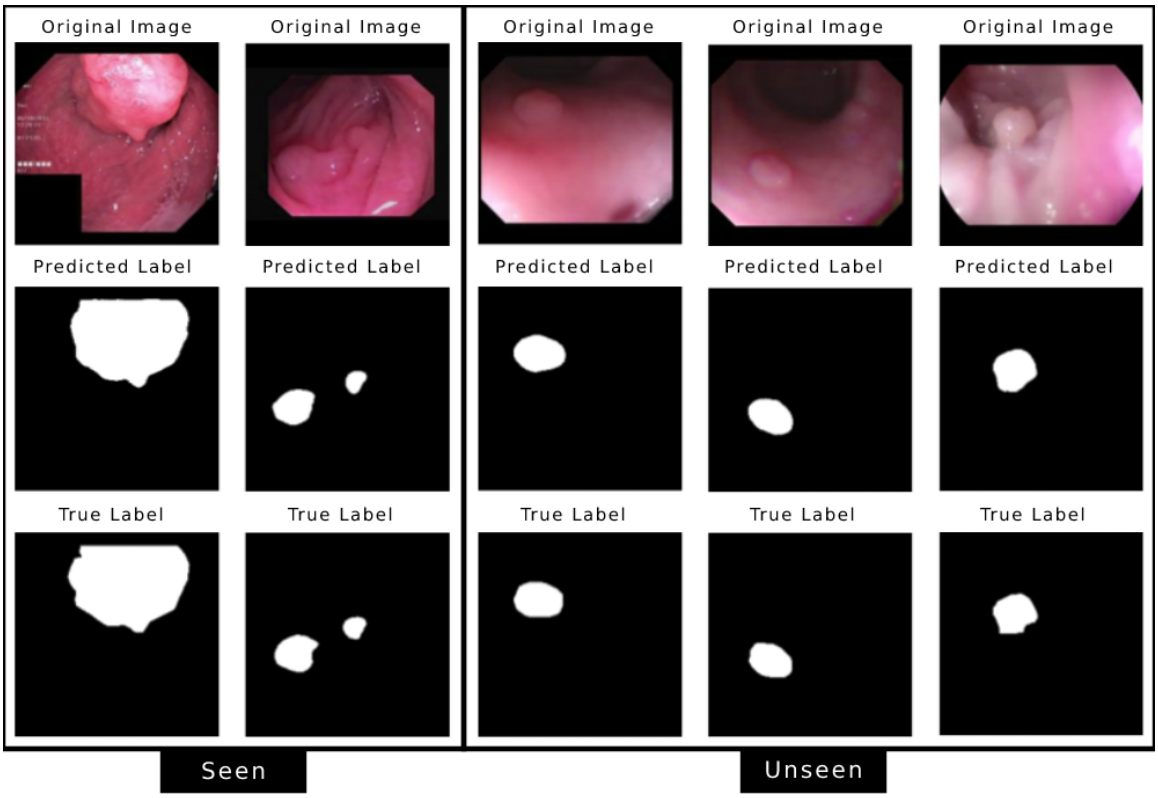

Figure A.2: Model's performance on test images from different datasets (from left) Kvasir, CVC-ClinicDB, CVC-300, Colon-DB, ETIS where first two are the seen datasets and last three are the unseen datasets.

A.6 Results

This section presents our results and the model's performance on different datasets, seen and unseen. The seen datasets are Kvasir and CVC-ClinicDB, as the model was trained using the sample images from these datasets. In contrast, the unseen datasets are CVC-300, CVC-ClinicDB, and ETIS, containing images the model has never seen. Figure A.2 shows the model's performance on sample test images from all five datasets.

A.6.1 Accuracy on individual dataset:

As the model was trained using sample images from Kvasir and CVC-ClinicDB, we can observe that the model accuracy is very high (Table A.1). Except for MAE on the Kvasir dataset, our model outperformed the current state-of-the-art in all evaluation metrics.

Table A.1
Model's performance and comparison with other models on the test dataset. Results have been reported from the *PraNet* [2] paper and have not been verified.

Dataset	Kvasir				CVC-ClinicDB			
Models	Dice	mIoU	F2	MAE	Dice	mIoU	F2	MAE
U-Net	0.818	0.746	0.794	0.055	0.823	0.755	0.811	0.019
U-Net++	0.821	0.743	0.808	0.048	0.794	0.729	0.785	0.022
ResUNet-mod	0.791	—	—	—	0.779	—	—	—
ResUNet++	0.813	0.793	—	—	0.796	0.796	—	—
SFA	0.723	0.611	0.670	0.075	0.700	0.607	0.647	0.042
PraNet	0.898	0.840	0.885	**0.030**	0.899	0.849	0.896	0.009
Proposed	**0.935**	**0.888**	**0.894**	0.031	**0.945**	**0.906**	**0.870**	**0.008**

A.6.2 Model Generalization:

Model generalization is measured by the accuracy of the model on unseen datasets (CVC-300, Colon-DB, and ETIS). Similar to the accuracy on the seen dataset, our model outperformed the state-of-the-art PraNet [2] (Table A.2). Similar to PraNet, our model achieved better performance on CVC-300 and Colon-DB compared to

ETIS. Images on the ETIS dataset are very different which causes the less accuracy.

Table A.2
Model's accuracy comparison on the unseen test dataset CVC-300, Colon-DB, and ETIS.

Dataset	CVC-300		
Models	Dice	mIoU	MAE
U-Net	0.71	0.627	0.022
U-Net++	0.707	0.624	0.018
SFA	0.467	0.329	0.065
PraNet	0.871	0.797	**0.010**
Proposed	**0.901**	**0.864**	0.016
Dataset	Colon-DB		
Models	Dice	mIoU	MAE
U-Net	0.512	0.044	0.061
U-Net++	0.483	0.41	0.064
SFA	0.469	0.347	0.094
PraNet	0.709	0.64	0.045
Proposed	**0.867**	**0.728**	**0.038**
Dataset	ETIS		
Models	Dice	mIoU	MAE
U-Net	0.398	0.335	0.036
U-Net++	0.401	0.344	0.035
SFA	0.297	0.217	0.109
PraNet	0.628	0.567	0.031
Proposed	**0.826**	**0.728**	**0.024**

A.6.3 Model's computational efficiency:

In the development of Mobile-PolypNet, major consideration was given to the model's size and computational efficiency. Table A.3 summarizes the number of parameters, disk space required, and FLOPs count, along with accuracy metrics while testing on the Kvasir dataset. The FLOPs counts for the other models have been measured

using TensorFlow with the code provided by the authors. Where the TecsorFlow code was unavailable, we tried to imitate the model using the information provided by the authors. While outperforming the current state-of-the-art on the accuracy metrics, the proposed model is approximately 83 times smaller in size and about 17 times less computationally expensive compared to PraNet (Table A.3).

PraNet model uses traditional convolution layers with a high number of filters (512, 1024, 2048), resulting in large number of trainable parameters and FLOPS count. In comparison, Mobile-PolypNet uses separable convolution and reduces the number of filters by one order of magnitude, with the highest number equal to 144 resulting in much smaller number of trainable parameters and FLOPs count.

Table A.3
Model efficiency is measured in terms of the number of parameters required by the model and the number of floating-point operations (FLOPs) performed by the model to process a single image of dimension 352×352 (this image size was only used for the FLOPs count). The FLOPs count has been tested on TensorFlow, and accuracy metrics comparison were made on the Kvasir dataset.

Models	**Number of parameters**	**Disk space**	**FLOPs count**	**Dice**	**mIoU**	**MAE**
U-Net	7.85M	30MB	52.6G	0.818	0.746	0.055
U-Net++	9.04M	34.6MB	112.6G	0.821	0.743	0.048
ResUNet-mod	7.85M	30MB	52.6G	0.791	—	—
ResUNet++	9.04M	34.6MB	112.6G	0.813	0.793	—
SFA	25.59M	97.7MB	222.4G	0.723	0.611	0.075
PraNet	20.52M	78.4MB	81.9G	0.898	0.840	**0.030**
Proposed	**246K**	**1.72MB**	**4.9G**	**0.935**	**0.888**	0.031

A.6.4 Model modification and performance (Ablation study):

To further investigate features of Mobile-PolypNet, we tried several of its variations. Table A.4 summarizes different model architectures and their performances on the Kvasir dataset. In the first variation (Mobile-Polypnet + MaxPool), in the inverted residual block, we replaced each stride-2 convolution with a stride-1 convolution followed by maxpooling. We also replaced upsampling transpose convolution with interpolated upsampling. Direct connection between the encoder and decoder in Mobile-PolypNet backbone is the simplest form of skip connection. In the next variation we replaced the skip connection with a single convolution operation (Mobile-PolypNet + ConvSkip). This extra block increased the FLOPs count. It also took longer for the model to converge. However, an improvement in the accuracy was observed. In the next variation (Mobile-PolypNet + PT), we used the MobileNetV2 [96] pre-trained with the ImageNet dataset from the Keras library as our encoder. The decoder remained the same. We observed that although the model converged quickly, it suffered from overfitting. To reduce overfitting, we inserted dropout layers in between convolution layers (Mobile-PolypNet + Dropout) in the Mobile-PolypNet backbone. Although it converges quickly, the achieved dice score was lower compared to other models.

As the average dice score for five models presented in Table A.4 is different, we did *t-tests* to measure the significance. While the addition of the convolution skip connection produced the highest accuracy, the difference is not significant (p-$value$=0.815). The use of maxpooling for dimension reduction compared to stride-2 convolution and interpolation compared to transpose convolution is highly debated in the literature [155, 156]. In our model, we observed a significant ($p - value = 0.018$) reduction in accuracy due to the use of maxpooling. The additional parameters required by the stride-2 and transpose convolution help to learn and preserve important spatial features in the network which improves the performance.

Table A.4
Computation and accuracy performance comparison of different modified models based on the same Mobile-PolypNet backbone architecture on the Kvasir dataset. FLOPs have been calculated for an image dimension of 224x224

Model	Number of trainable parameters	Number of non-trainable parameters	FLOPs count	Number of epochs to converge	Dice	MAE
Baseline	233,001	13,616	2.0G	145	0.935	0.031
Baseline + MaxPool	223,913	13,616	1.8G	217	0.900	0.047
Baseline + ConvSkip	250,601	13,616	2.2G	186	**0.938**	**0.028**
Baseline + PT	234,618	2,495,257	**1.5G**	**50**	0.912	0.037
Baseline + Dropout	233,001	13,616	2.0G	110	0.928	0.035

A.6.5 Model's limitations:

Although our model achieved state-of-the-art accuracy, we observed that it failed to properly segment the polyp in some images. It also wrongly segmented certain blobs as polyps in some images. However, we believe by processing video frames and comparing two consecutive frames, we can reduce wrong segmentation in some images.

A.7 Conclusion

In this paper, we presented a novel Mobile-PolypNet architecture for automatic segmentation of the colorectal polyp. The model has been tested on five publicly available datasets and compared with the current state-of-the-art models. The network achieved state-of-the-art accuracy with orders of magnitude reduction in the computational cost. Compared with the current state-of-the-art *Pranet*, Mobile-PolypNet requires 83 times fewer parameters and is about 17 times more computationally efficient, making it an excellent model for a segmentation backbone for deployment on resource-sensitive devices.

Appendix B

Mobile-RetinaNet : A Deep U-net for Retinal Fundus Image Segmentation for Use in Low-resource Settings

Ranit Karmakar, Saeid Nooshabadi, Allen O. Eghrari

B.1 Abstract

B.1.1 Purpose

Retinal fundus photography is used by physicians to detect and track different eye diseases such as glaucoma and diabetic retinopathy (DR). Extracting the retinal vessels and optic discs manually is time and resource-consuming. This work presents a computer-aided automatic segmentation model for the retinal blood vessels and optic disc in retinal fundus images.

B.1.2 Method

We proposed a novel and efficient deep learning image segmentation architecture fundus image with the efficient use of bottleneck residual blocks on the U-Net like encoder-decoder convolutional neural network (CNN) backbone. The model has been trained and tested on two publicly available retinal datasets with widely used parameters accuracy, sensitivity, specificity, and the area under the curve (AUC). To measure the model's computational efficiency, we used the platform-independent FLOPs count.

B.1.3 Results

This model achieved close to state-of-the-art performance with much higher computational efficiency. While our base model achieved the AUC score within 2% compared to the SA-UNet, our model requires almost half the number of parameters and is 4.5 times more efficient.

B.1.4 Conclusion

Accurate automatic detection of these image features will reduce the manual effort while producing consistent results in clinical settings instantaneously. High efficiency and low FLOPs count make it suitable for low-resource implementation.

B.2 Introduction

Retinal fundus photography is used to image the posterior segment of the eye. These images are used by clinicians to measure the health of the retina and check for diseases such as diabetic retinopathy (DR) and Glaucoma. While DR damages the blood vessels, optic disc to optic cup ratio from fundus images is used to detect and measure

glaucoma in patients. While both DR and Glaucoma can cause irreversible blindness, early detection and tracking may help prevent vision loss [207].

The first step in automatic detection of DR and glaucoma is segmenting the retinal fundus images. Manual segmentation is very strenuous and can add manual biases, affecting the measurement. Automatic segmentation can eliminate these challenges and make the segmentation quick and observer independent.

Vessel segmentation and optic disk segmentation come with different challenges. For retinal blood vessels, due to their unique and fine structure, developing a robust and automatic image segmentation technique is challenging. Over the years, different methods have been proposed, that are broadly divided into two categories; classical methods that are simple but less accurate, and deep learning techniques that are highly accurate but computationally inefficient [164]. Recently light-weight deep learning models have been proposed that provide a balance between accuracy and computational efficiency [164]. Development of models that yields to computationally efficient implementation are critical for several reasons:

1. Deep learning models generally require high power GPUs to run. Computationally efficient models have the benefit of running on low resource devices with limited computational power and memory.

2. While being accurate, efficient models can produce faster, real-time results,

necessary necessary for embedded environment.

In this work, we achieved a balance between accuracy and efficiency, proposing a novel Mobile-RetinaNet architecture that is highly computationally efficient compared to the current state-of-the-art models, making it suitable for deployment in low resource devices. Portable, handheld retinal fundus cameras are widely available in the market, that are connected to either mobile phones or similar low-power device. Our model because of it low computational and memory footprint can run on these devices and produce real-time results.

Mobile-RetinaNet has similarities to the M2U-Net [164] but is different in three significant ways.

1. Decoding path: In Mobile-RetinaNet, the bottleneck residual block is used as the fundamental building block for the network, even in the decoding path, which is a novel decoding architecture used on the U-Net backbone.

2. Untrained encoder: In Mobile-RetinaNet, we have replaced the pre-trained MobileNetV2 [96] in the encoder with our untrained encoder architecture (explained in the methods section), which is also struturally different from the M2U-Net [164] and original MobileNetV2 [96].

3. Upsampling operation in decoder: Our decoder block uses transposed convolution with trainable parameters to increase the feature resolution (height and

width) in the decoder block, instead of bilinear upsampling in M2UNet [164]. The proposed method is 4.5 times more efficient with comparable accuracy compared to the state-of-the-art model, SA-UNet [167].

B.3 Related Works

B.3.1 Medical Image Segmentation

The first reported deep learning method with significant results in biomedical image segmentation was U-Net [95]. It also showed substantial improvement even with a small dataset. Modifications of the U-Net have been employed to improve the performance in specific applications. U-Net++ [113], Residual U-Net [184], Recurrent Residual U-Net [185] Dense-UNet [186, 187], and U-Net with pre-trained encoders [188] are a few examples.

B.3.2 Retinal Vessel Segmentation

Specific to retinal vessel segmentation, there are several convolutional neural network (CNN) based architectures [208, 209, 210, 211]. Notable are Vessel-Net [162], DEUNet [161], AGNet [181], MS-NFNet [160]. They all share some similarities with U-Net.

These deep neural networks have reported a significant improvement over the previous models. However, they all suffer from large size and high complexity.

SA-UNet [167], the current state-of-the-art, achieves high accuracy with a comparatively simpler network by replacing the bottleneck layer between the encoder and decoder of a regular U-Net with a Spatial Attention Module (SAM) [189]. This model reduced the number of parameters required to 0.5 million while achieving high accuracy. However, due to the use of regular convolution blocks, SA-UNet is still reasonably computationally expensive.

Model efficiency in terms of model size and computational efficiency are important factors for deep learning models. To this end, in MobileNetV2 [96] convolution was replaced with separable depthwise convolution and pointwise filters. To take advantage, M2U-Net [164], a work for retinal vessel segmentation, replaced the encoder in U-Net with a pre-trained MobileNetV2 [96]. In the decoder part M2U-Net used a residual block with a contraction factor of 0.15 [164]. This modification of the decoder block significantly reduced the computational cost of this architecture with respect to SA-Unet [167]. However, the reduction in complexity in M2U-Net has come at the expense of a significant reduction in the model's accuracy and a small increase in the number of tunable parameters.

One more recent work (W-Net [212]) proposed a cascaded network of two minimalistic

U-Net models, W-net, for retinal vessel segmentation. The work achieves a higher accuracy compared to other related works using only 68.5 thousand parameters. While the reduction in the use of number of parameters is significant, it comes with a cost of accuracy.

Our model on the other hand while has 2.5 times fewer parameters, has no significant drop in accuracy compared with the best reported results by SA-UNet [167].

B.3.3 Retinal Optic Disc Segmentation

The unsupervised methods mostly use classical image processing techniques such as morphological processing [194, 196] to detect and segment the optic discs. Due to their unique shape, size, and brightness, optic discs are easily distinguishable from the background and the retinal vessels for morphological processing to work well. However, in the presence of unusual pathology or uneven illuminations, these methods tend to fail. There are also shape-based image segmentation techniques [197, 200] for optic disc contour detection which face similar challenges.

With the emergence of multiple supervised learning-based approaches, they have been applied to optic disc segmentation. These works are primarily divided into semi-supervised learning and fully supervised methods. The semi-supervised methods involve shape, size, color-based image features, wavelet feature selections followed

by classification. There has also been the use of superpixels [197] and pixel-wise k-means clustering [198, 199] for the semantic segmentation of the optic discs. The use of fuzzy systems such as c-means clustering methods [195], and fuzzy broad learning systems [202] have also been proposed. Although these methods perform better than the classical image processing methods, they still lack the robustness required in the clinical setting.

On the other hand, fully supervised methods, primarily use deep neural networks such as U-Net [205], fully-connected CNN [193], and modified U-Net-based models such as multi-label deep learning networks [203] and Res-UNet models [204]. Although deep neural networks can overcome the challenge of generalizability, they are highly resource-consuming.

B.4 Material and Method

B.4.1 Dataset Preparation and image augmentation

For training and testing, we used most widely used publicly available dataset, DRIVE [165] and CHASE [166]. For the vessel segmentation task, we used the same dataset as SA-UNet as they are the current state-of-the-art in terms of accuracy. This also

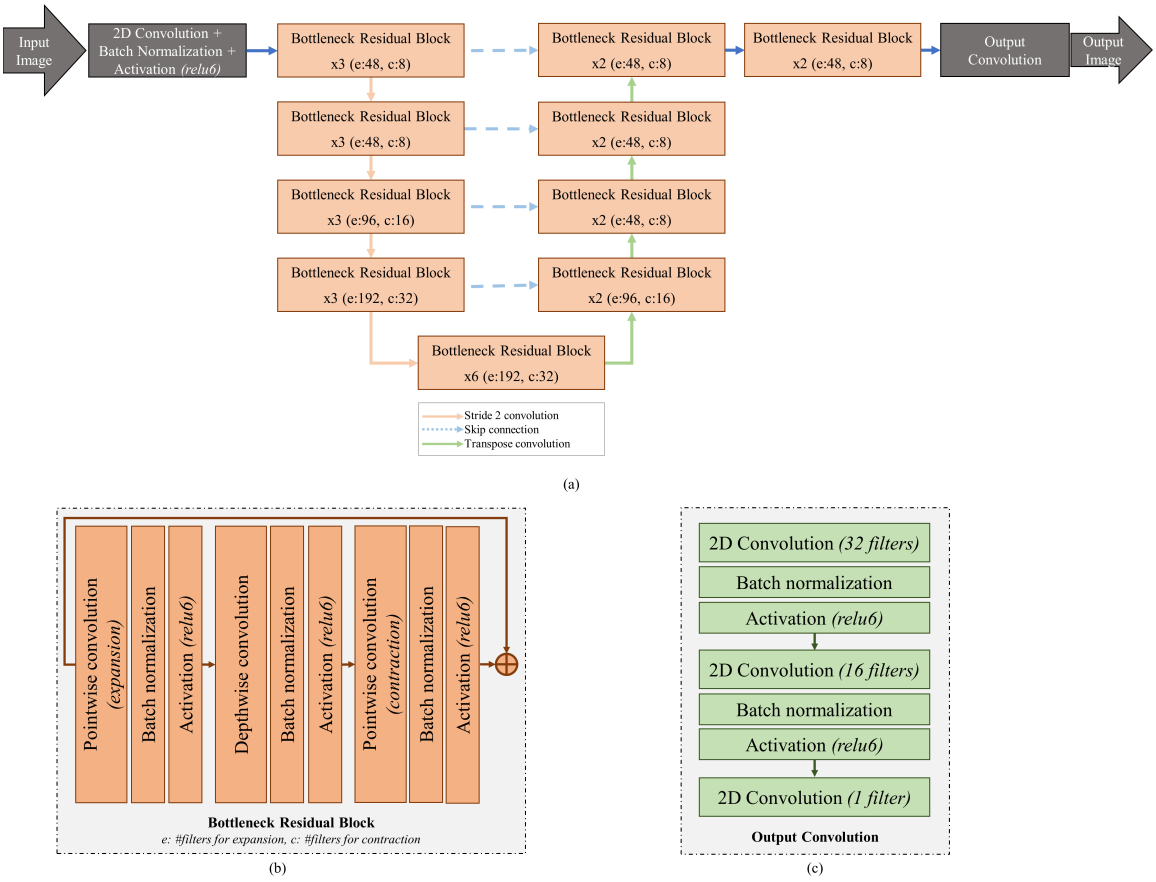

Figure B.1: (a) Mobile-RetinaNet architecture, (b) Inverted residual convolution building block, (c) Output convolution block

allowed us to make a meaningful comparison with the experimental results from SA-UNet. However, we have resized the images in both datasets to 512x512 (similar to Vessel-Net).

For the optic disc segmentation, however, we took a slightly different approach. We cropped each image around the optic disc to create patches. Next, we applied random rotation, Gaussian noise, color jittering, horizontal and vertical flip, and changed the image brightness. The ground truth labels were created under the supervision of

Table B.1
Description of the dataset based on image dimension, number of images for training, validation, testing, and the applied image augmentations.

Dataset	Original Dimension	Output Dimension	Number of training images	Number of validation images	Number of testing images
Retinal Vessels					
DRIVE[165] †	584x565	512x512	234	26	20
CHASE[166]†	999x960	512x512	247	13	8
†Vessels augmentation: Random rotation, Gaussian noise, color jittering, horizontal, vertical and diagonal flips.					
Optic Disc					
DRIVE[165] *	584x565	256x256	203	51	20
CHASE[166] *	999x960	256x256	208	52	8
*Optical disc augmentation: Random rotation, Gaussian noise, color jittering, horizontal and vertical flips, and brightness adjustment.					

an ophthalmologist. Table B.1 provides more information about the dataset size, dimension of the images, and augmentations applied.

B.4.2 Network Architecture

The model proposed in this paper uses the fundamental encoder-decoder architecture with skip connection similar to UNet (Figure B.1). However, the biggest difference between the UNet and our model is the model building blocks. While UNet used traditional convolution operations, we replaced it with bottleneck residual blocks (b in Figure B.1) with an expansion factor of 6. Details of the encoder and decoder path are given below. Each convolution operation is followed by batch normalization and

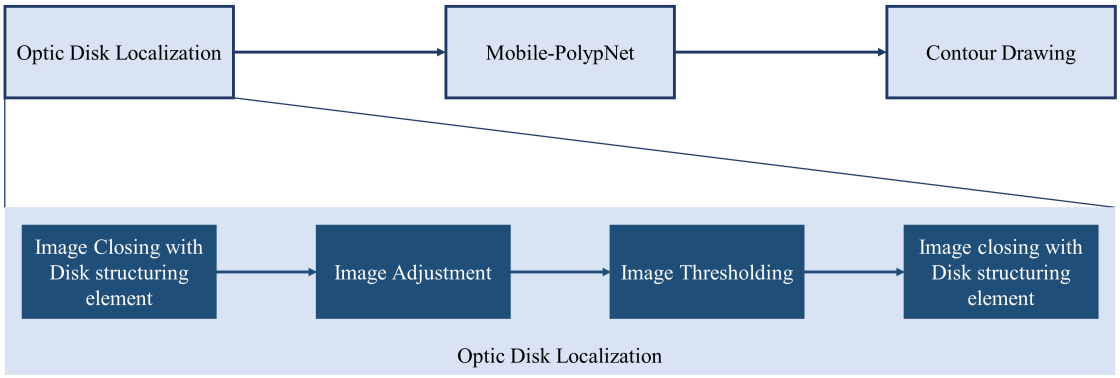

Figure B.2: Optic disc locaization workflow. The first operation is classical image processing based optic disc localization. Second block is the Mobile-RetinaNet trained with cropped images for optic disc segmentation. Third block uses the semantic segmentation and draw a elliptical contour around it.

ReLu6 activation unless otherwise noted.

B.4.2.1 Encoder path

For the encoder path, input image is first processed with a traditional convolution layer to increase the number of channels to eight while preserving the image resolution. This convolution layer was followed by a depthwise convolution and another traditional convolution with eight filters. The output from this layer was fed to a series of bottleneck residual blocks while progressively reducing the resolution (height and width) of the feature map by a factor of two. Each level has three bottleneck residual blocks where first depthwise convolution operation of the first bottleneck residual block uses stride-2 convolution to reduce the feature map resolution. Number of filters used in the contraction operation are 8, 8, 16, 32, and 32 for the encoding

path.

B.4.2.2 Decoder Path

Similar to encoder path, we used the bottleneck residual blocks for the decoder path as well. However, each level has only 2 bottleneck residual blocks. To increase the resolution of the feature map, we used traditional transposed convolution. The number of filters in the contraction operations were 16, 8, 8, and 8 with an expansion factor of 6. In the decoder path, we used additional bottleneck residual blocks twice before passing the feature map to the output convolution layer. In the output convolution (c in Figure B.1), we used traditional convolution operation twice with 8 filters and once with 1 filter. Finally, we used a sigmoid activation to get the final output.

B.4.3 Optic Disc Localization

Optic discs are circular and generally brighter than the rest of the image. Vessels, similarly, tend to be bright; however, their shapes are distinctly different from that of the optic discs. To better localize the optical disc, we developed a classical image processing algorithm to perform a localization (Figure B.2). First, we process the image with an image closing operation with a disc structuring element. This removes everything from the image except from the area with optic disc which appears as

a bright area. We then used contrast adjustment to scale the image pixel intensity between 0 and 255. After processing we observed that the center of the optic disc was brightest in the processed image. Hence, we used a threshold of 250 to localize the center of the optic disc. To avoid any micro pixels anywhere else in the image, we perform another image opening operation with the same structuring element. With that the center of the optic disc is accurately localized. We determine the centroid of that blob and crop a patch of 256x256 around the centroid.

B.4.4 Experiments

B.4.4.1 Retinal Vessel Segmentation

To test our model's accuracy, efficiency, and robustness, we compared it with all the state-of-the-art retinal vessel segmentation models. We also tested how the model size changes with the increase in the size of the image. Finally, we modified our backbone model to test its performance with different modifications. All of these experiments are elaborated in the results and discussion sections.

B.4.4.2 Optic Disc Segmentation

For optic disk segmentation, the network was trained with cropped images centered around the optic disc. For testing we performed two experiments. In the first, the test images were manually cropped before feeding it to the network to perform semantic segmentation. In the second experiment, fully-automated, we took a hybrid approach, where optical disc was first localized using the procedure in Figure B.2. Next a crop of the localized area was obtained and fed to network.

B.4.4.3 Model Refinement and Modifications

To further explore Mobile-RetinaNet in Figure B.1, we modified the model and tested it for the vessel segmentation task in three different ways. In two of the modified models, we replaced the skip connection by convolution (Mobile-RetinaNet + ConvSkip) and Spatial Attention Module (SAM) (Mobile-RetinaNet + SASkip) [189]. For the third model (Mobile-RetinaNet + PT), we used MobileNetV2 encoder block pre-trained with ImageNet dataset from Keras library.

B.4.5 Loss Function

In segmentation models, cross-entropy loss, Dice loss and Jaccard loss or sometimes their combination, are widely used as loss metrics. We chose BCE loss as our loss function for the retinal vessel segmentation, as it produces the best overall results compared to the other loss functions. for the optical disc segmentation we used Dice as the best performing loss metric.

B.4.6 Experiment Platform

We used Tensorflow with GPU support to develop our models. The floating point operations (FLOPs) count was calculated using the Keras library. The FLOPs count for the other models, we used the codes provided by the authors, if available, or implemented them ourselves. All the models were trained and tested on an NVIDIA GTX 1060 6GB GPU running on an Intel i7-8750H CPU with 16GB RAM. The dimension of input and output images was 512x512 for the vessel segmentation and 256x256 for the optic disc segmentation. We used Adam optimizer with a learning rate of 1e-3. Due to the limited hardware resources, the batch size was set to 1 for the vessel segmentation and 2 for the optic disc segmentation.

B.4.7 Training Performance Metrics

For the retinal vessel segmentation task, the area under the curve (AUC) on the validation set was monitored to track the model's performance. The best model was saved based on the validation AUC. If the validation AUC did not improve after 50 iterations, we stopped the training. For the OD segmentation, we monitored the Dice score instead and stopped the training when it did not improve after 50 iterations. The model's performance was evaluated using the significant metrics for the evaluation of a segmentation model, including sensitivity (SE), specificity (SP), accuracy (ACC), area under the curve (AUC), and Dice score/F1 score. To evaluate the model's efficiency, we used platform-independent FLOPs count. We also compared the model's size by the number of parameters and the disk space required for storing the model.

B.4.8 Statistical Analysis

To compare the performance between two models, we used two-sided t-test using Python's SciPy library. As our data came from a normal distribution p-value from t-test gave us an understanding whether the difference in performance was significant. We tested the normality using normaltest from the SciPy library. We used a cut-off of $\alpha = 0.05$ as a threshold for significance test.

Table B.2
Model efficiency compared with the current state-of-the-art models in respect of parameters, FLOPs count, number of training epochs, and the mode disk space requirement.

Model	Parameters	FLOPs (G)	Epochs	disk space
U-Net[95]	34512193	406.4	-	395.2 MB
Yan [159]	25955330	3851.1	-	297.2 MB
AG-Net [163]	9408545	116.4	-	108.0 MB
ERFNet [168]	2095841	26.9	-	24.6 MB
MS-NFN [160]	1480900	285.7	100	17.6 MB
Vessel-Net [162]	662108	86.3	150	7.8 MB
M2U-Net [164]	617013	**2.6**	300	7.7 MB
SA-Unet [167]	537707	19.7	150	6.5 MB
Mobile-RetinaNet	**197385**	4.4	**28**	**3.6 MB**

B.5 Results

B.5.1 Model Efficiency

Mobile-RetinaNet requires the lowest number of parameters (Table **??**). Compared to the current state-of-the-art, the number of parameters is reduced by half, and the FLOPs count is reduced by 4.5 times. Compared to similar M2U-Net, the parameter requirement for our model is 2.5 times less, with a small increase in the number of FLOPs. When tested on the same hardware as the training, with GPU acceleration enabled the inference time was 48.1 milliseconds. Compared to that, with GPU acceleration disabled, the inference time was 122.2 milliseconds.

Table 2 also lists the epoch count for different models. While the other models used a

Table B.3
Accuracy of Mobile-RetinaNet for the retinal vessel segmentation task on DRIVE and CHASE datasetsx compared with other state-of-the-art methods

Model	SE	SP	Acc	AUC
		DRIVE[165]		
Yan [159]	0.765	0.982	0.954	0.975
Liskowski [157]	0.781	0.981	0.954	0.979
MS-NFN [160]	0.784	0.982	0.957	0.981
Orlando [158]	0.79	0.968	0.945	0.951
DEU-Net[161]	0.794	0.982	0.957	0.977
Vessel-Net [162]	0.804	0.98	0.958	0.982
AG-Net[163]	0.81	**0.985**	0.969	0.986
M2U-Net[164]	-	-	0.963	0.974
SA-Unet[167]	0.821	0.984	**0.97**	**0.986**
Mobile-RetinaNet	**0.822**	0.974	0.955	0.968
		CHASE[166]		
Yan [159]	0.763	0.981	0.961	0.978
Liskowski[157]	0.782	0.984	0.963	0.982
MS-NFN [160]	0.754	0.985	0.964	0.983
Orlando[158]	0.728	0.971	0.946	0.952
DEU-Net [161]	0.807	0.982	0.966	0.981
Vessel-Net[162]	0.813	0.981	0.966	0.986
AG-Net [163]	0.817	**0.985**	0.974	0.986
M2U-Net[164]	-	-	0.97	0.967
SA-Unet[167]	0.857	0.984	**0.976**	**0.991**
Mobile-RetinaNet	**0.877**	0.976	0.97	0.985

fixed number of epochs for training, we made it flexible by monitoring the performance on the validation set. As we can observe, our model also converges rapidly and does not require a great deal of training. Although the training time is not always a significant concern, it impacts the overall time during the development.

B.5.2 Model Accuracy

B.5.2.1 Retinal Vessel Segmentation

Mobile-RetinaNet yields the highest sensitivity the CHASE and DRIVE datasets (Table B.3). On all the other metrics, the results achieved for Mobile-RetinaNet are very close to the other models. A random set of sample output from the model is presented in Figure B.3.

B.5.2.2 Retinal Optic Disc Segmentation

Optical disc is localized in small neighborhood in the overall image, training the model with patches make the training very efficient. For all the test images, our fully-automatic localization algorithm was able to localize the optical disc. After which Mobile-RetinaNet was used to successfully segment the optical disc. Both fully-automatic and semi-automatic methods were able to produce high quality segmentation (Table B.5) close to the true labels. Figure B.4 presents the sample outputs from both the methods used.

We did not observe any significant difference between the semi-automatic and fully-automatic methods proving the effectiveness of the workflow. By performing t-test

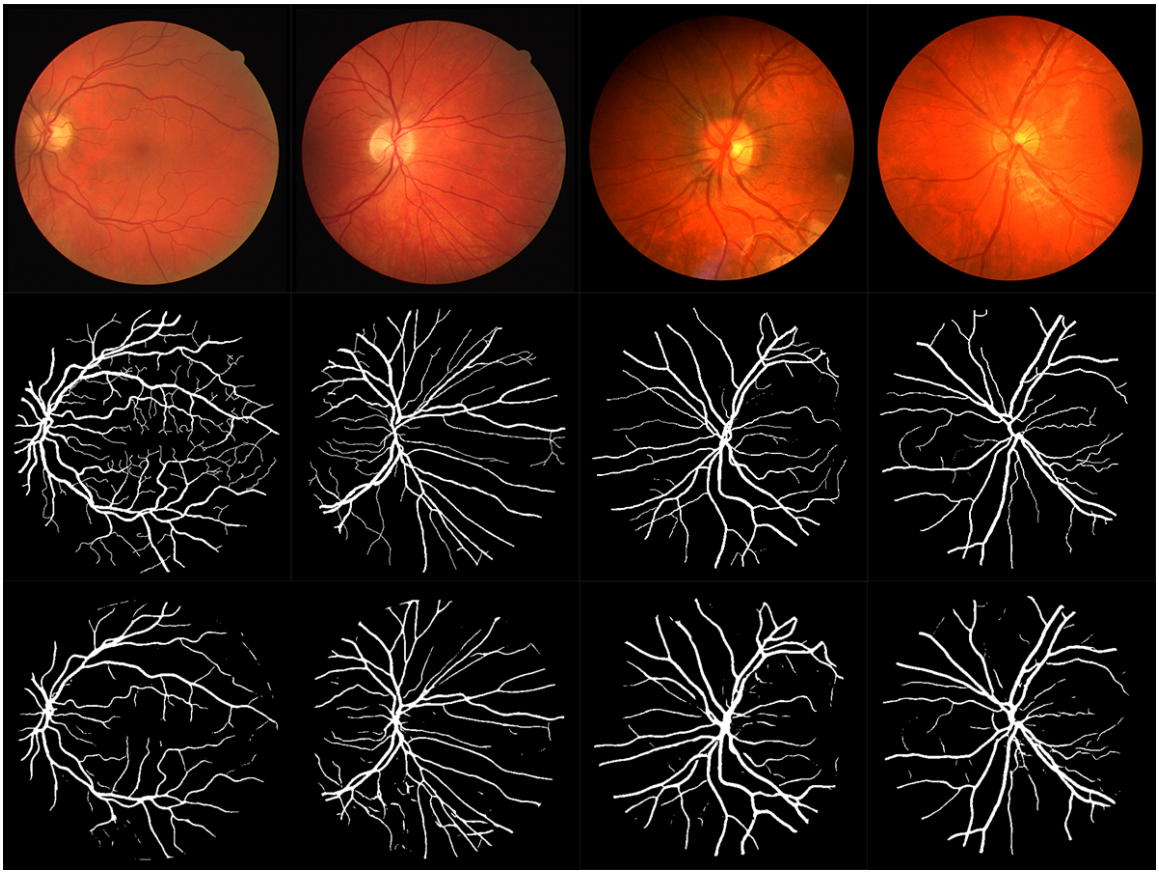

Figure B.3: Comparison of models accuracy on different images with the true label. Second row is true label and third row is the output. First two images are from the DRIVE dataset and last two images are from the CHASE dataset.

between the results from these two methods (Table B.5), we found no significant difference ($p-value = 0.8$) proving the efficacy of the fully automated hybrid approach.

B.5.2.3 Loss Function Evaluation

Table **??** summarizes Mobile-RetinaNet's performance on different loss functions. For the mixed loss, we used the average of Dice and Jaccard losses. Experimentally, we

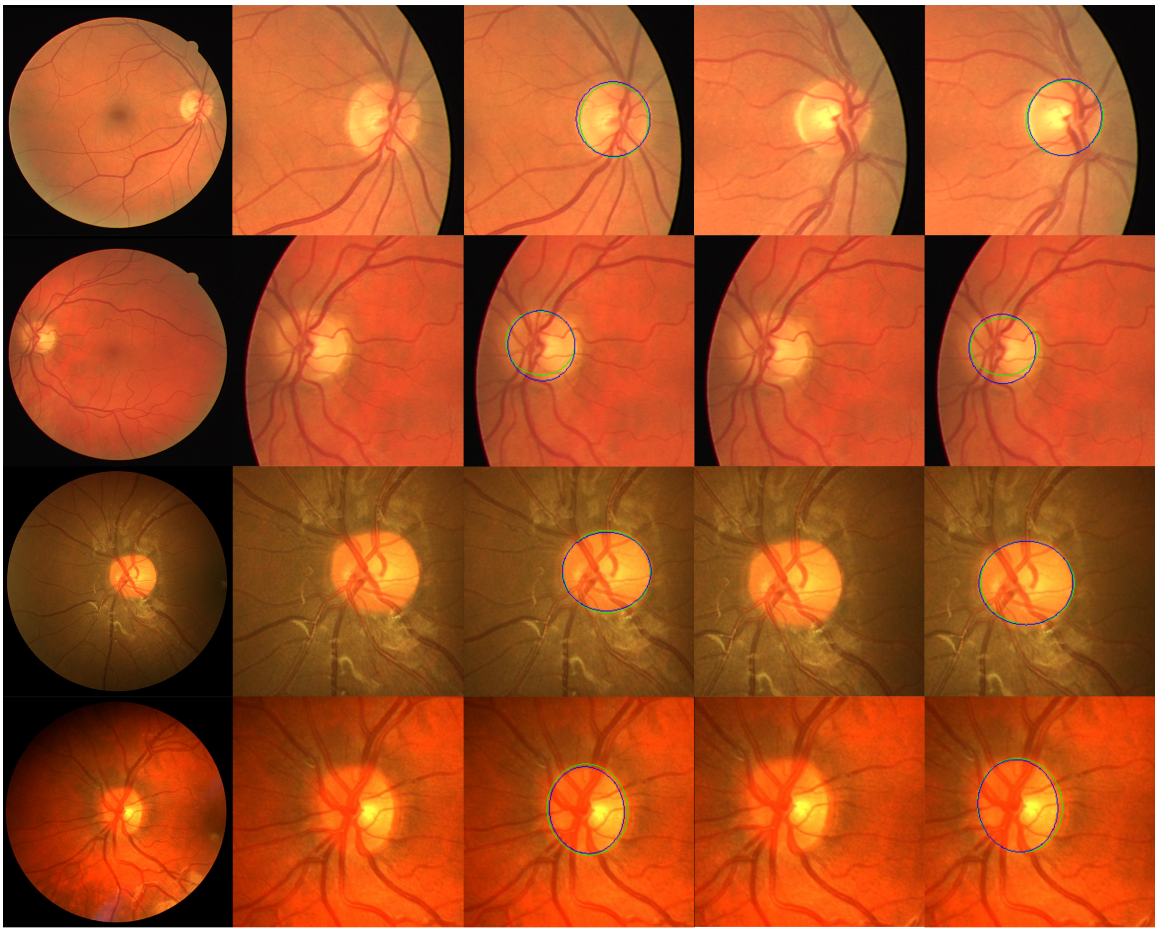

Figure B.4: Sample output using semi-automatic and fully-automatic optic disc segmentation. (a) original image, (b) manual localization, (c) optic disc segmentation on the manually localized image, (d) automatic optic disc localization, (e) optic disc segmentation on the automatic localized image. Blue ring shows the true label and green ring shows the predicted label.

found BCE loss produced the best results for the retinal vessel segmentation, and Dice for the optical disc segmentation. Figure B.5 provides a side-by-side comparison of the true segments and predicted segments for several loss functions.

Table B.4
Mobile-RetinaNet model's performance comparison with different loss functions

Loss function	SE	SP	Acc	AUC	F1
DRIVE[165]					
BCE loss	0.822	**0.974**	**0.955**	**0.968**	**0.818**
Dice loss	**0.862**	0.964	0.949	0.929	0.806
Jaccard loss	0.837	0.910	0.901	0.915	0.675
Mixed loss	0.830	0.972	0.954	0.918	0.817
CHASE[166]					
BCE loss	**0.877**	**0.976**	**0.970**	**0.985**	**0.776**
Dice loss	0.869	0.971	0.965	0.932	0.749
Jaccard loss	0.852	0.965	0.958	0.920	0.713
Mixed loss	0.836	0.975	0.967	0.916	0.749

Table B.5
Comparison of segmentation accuracy between fully-automatic and semi-automatic workflow for optical disc segmentation task.

	SE	SP	Acc	AUC	F1
DRIVE [165]					
Semi-auto	0.891	0.984	0.975	0.948	0.858
Fully-auto	0.898	0.984	0.975	0.950	0.862
CHASE [166]					
Semi-auto	0.989	0.967	0.970	0.986	0.859
Fully-auto	0.966	0.970	0.969	0.981	0.866

B.5.3 Model Refinement

From Table B.6 it can be seen that out of the four models, Mobile-RetinaNet + PT was quickest to converge and produced the best F1 score but the diskspace required, FLOPs count, and the number of parameters were the highest. However, the FLOPs requirement for Mobile-RetinaNet + PT was still lower than the SA-UNet. Mobile-RetinaNet + PT was also produced state-of-the-art results, better than SA-UNet,

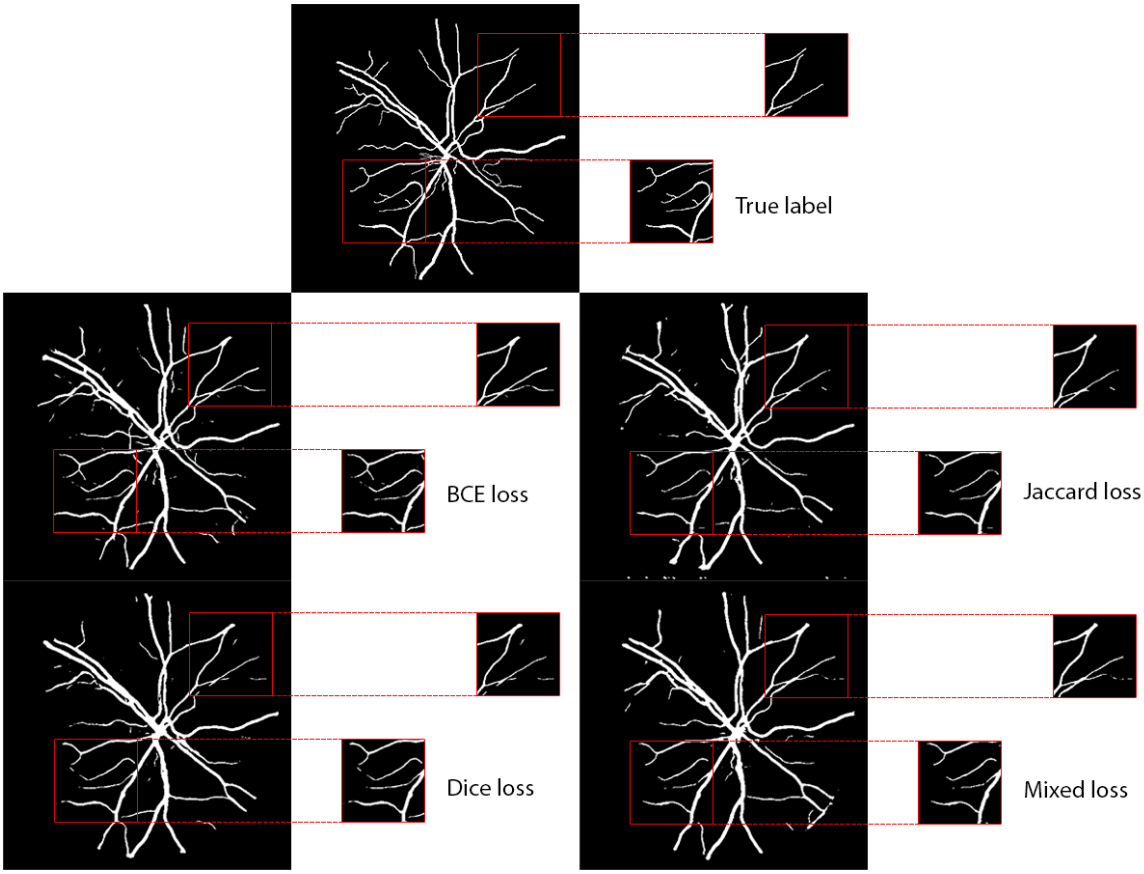

Figure B.5: Side-by-side comparison of the Mobile-RetinaNet model's segmentation with different loss functions. It can be observed that with BCE, we were able to detect tiny vessels with high resolution than other loss functions

on the CHASE dataset. For the DRIVE dataset, F1 score is only 0.2% lower than SA-UNet.

B.6 Discussion

Depending on the model and the task in hand, different loss functions produce different results. Hence, choosing the right loss function is very crucial for the training of a

Table B.6
Accuracy and efficiency comparison between the modified models with two state-of-the-arts M2U-Net and SA-UNet

Modified models	Efficiency			
	Trainable Parameters	Epochs	FLOPs	Disk Space
DRIVE[165]				
Mobile-RetinaNet	**197385**	28	4.4 G	**3.6 MB**
Mobile-RetinaNet + ConvSkip	210377	49	4.6 G	3.8 MB
Mobile-RetinaNet + SASkip	197385	39	4.5 G	3.7 MB
Mobile-RetinaNet + PT	449041	**7**	6.4 G	14.8 MB
M2U-Net [164]	617013	300	**2.6 G**	7.7 MB
SA-UNet	537707	150	19.7 G	6.5 MB
CHASE[166]				
Mobile-RetinaNet	**197385**	12	4.4 G	**3.6 MB**
Mobile-RetinaNet + ConvSkip	210377	34	4.6 G	3.8 MB
Mobile-RetinaNet + SASkip	197385	**7**	4.5 G	3.7 MB
Mobile-RetinaNet + PT	449041	51	6.4 G	14.8 MB
M2U-Net	617013	300	**2.6 G**	7.7 MB
SA-UNet [167]	537707	150	19.7 G	6.5 MB

Modified models	Accuracy				
	SE	SP	Acc	AUC	F1
DRIVE[165]					
Mobile-RetinaNet	0.822	0.974	0.955	0.968	0.818
Mobile-RetinaNet + ConvSkip	**0.827**	0.973	0.954	0.967	0.816
Mobile-RetinaNet + SASkip	0.798	0.978	0.956	0.959	0.816
Mobile-RetinaNet + PT	0.815	0.978	0.957	0.970	0.824
M2U-Net [164]	-	-	0.963	0.974	0.809
SA-UNet	0.821	**0.984**	**0.970**	**0.986**	**0.826**
CHASE[166]					
Mobile-RetinaNet	0.877	0.976	0.970	0.985	0.776
Mobile-RetinaNet + ConvSkip	0.807	0.978	0.966	0.970	0.768
Mobile-RetinaNet + SASkip	0.827	0.973	0.963	0.975	0.761
Mobile-RetinaNet + PT	**0.940**	**0.987**	**0.983**	**0.996**	**0.883**
M2U-Net	-	-	0.970	0.967	0.801
SA-UNet [167]	0.857	0.984	0.976	0.991	0.815

deep learning model. For the vessel segmentation using Mobile-RetinaNet, we found (Table B.4) BCE loss produced the best result. The AUC was found to be highest for

the BCE loss and by performing t-test, we observed that the difference is significant ($p - value \leq 0.0001$).

The Dice and Jaccard losses are more useful in blob segmentation tasks such as optical disc where the global neighborhood information is as much relevant as the local neighborhood. For vessel segmentation, however, local neighborhood information is more important which can be better represented using BCE loss. That said mixed loss (average of Dice and Jaccard) achieved the second-best performance for F1 score after BCE. In Figure B.5, we can observe the BCE loss was able to track and extract fine vessel features better compared to other loss functions.

For the blob type optical disc segmentation, on the other hand, because global information was relevant, we used negative Dice loss to train the model and achieved high accuracy.

In this work, developing an efficient image segmentation model while maintaining high accuracy was our utmost priority. By using the bottleneck residual blocks, we brought the FLOPs count down to 4.4G for the original model. Although this was slightly higher compared to M2U-Net, which has the smallest FLOPs count, proposed model is smallest is size and produced better accuracy performance (Table B.2 and Table B.3). Figure B.6 is visual illustration of Mobile-RetinaNet in comparison with other related works. We achieved better efficiency compared to any of the previous models proposed, closest to the state-of-the-art SA-UNet, while computationally

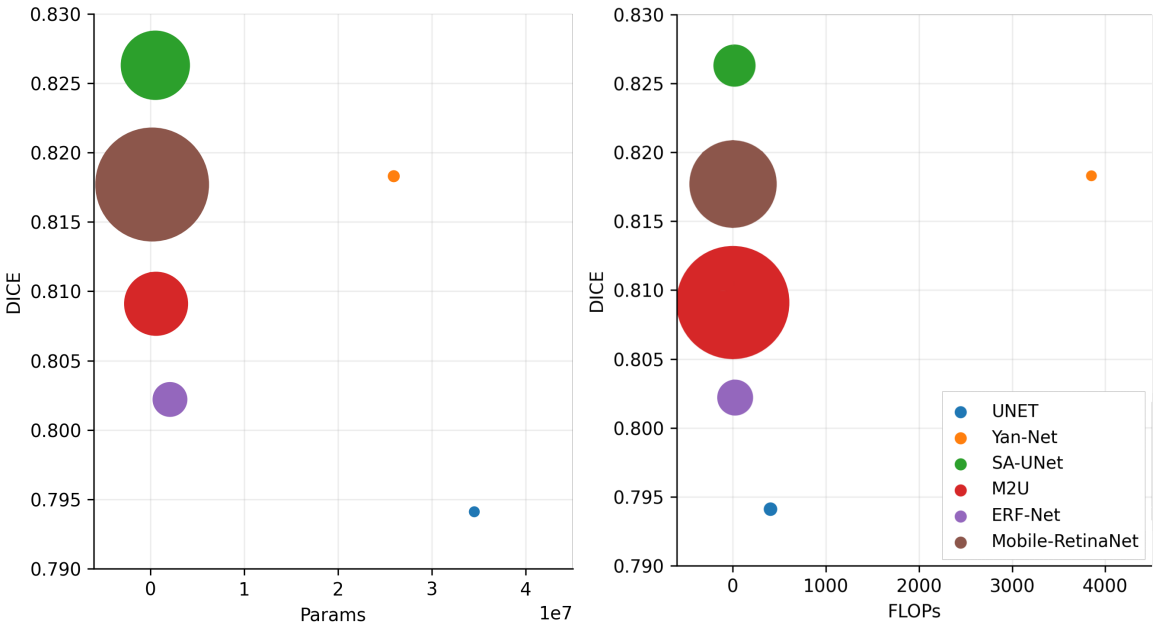

Figure B.6: (Left) Dice score comparison between models with respect to the FLOPs count. The size of the circles is evaluated by taking a ratio of Dice score and FLOPs count. (Right) Dice score comparison between models with respect to the number of parameters. The size of the circles is evaluated by taking a ratio of the Dice score and the number of parameters. Bigger the circle better the performance.

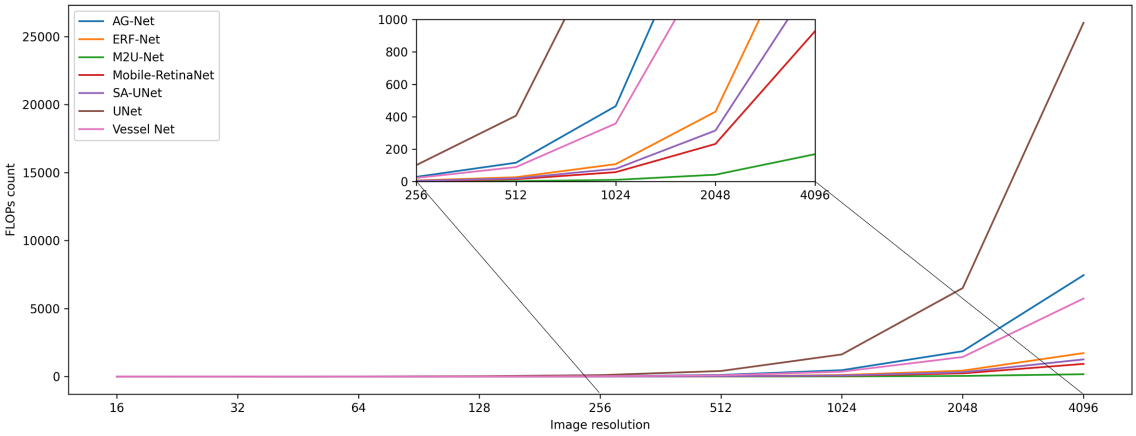

Figure B.7: Increase in FLOPs count for increased image resolution

highly efficient, closest to the most efficient model M2U-Net.

Figure B.7 compares how the input image resolution affects the FLOPs count for

different models. Although the difference is hardly noticeable for the image resolution below 256, for the images above that resolution, the FLOPs increased in a quadratic fashion. For fundus imaging, detection of tiny retinal vessels is important and hence high image resolution can provide richer information. However, that increases the computation time significantly if the network is not efficient. In the zoomed in portion of the plot in Figure B.7, we can observe how the image dimension affects model's efficiency. For higher resolutions (2048x2048 or 4096x4096), the difference between SA-UNet and Mobile-RetinaNet is clearly significant, however, the difference between M2U-Net and Mobile-RetinaNet is not that high.

We emphasize the fact that our models were trained and tested on two small datasets. Increasing the diversity of the population for obtaining the images, and the change in the imaging system for capturing retinal fundus images, might impact the model's performance.

B.7 Conclusion

This work presented the development of a highly efficient deep learning model that produces segmentation for the retinal vessel and optic disc from the retinal fundus images. With the use of bottleneck residual blocks on a U-Net type architecture, we were able to produce results with accuracy very close to the state-of-the-art SA-UNet

while highly computationally efficient. This high efficiency allows the deployment of this model on mobile devices such as smartphones.

The models were trained and tested on two publicly available fundus datasets, DRIVE and CHASE. The proposed models achieved highest sensitivity score for both the datasets with a loss in AUC score of 1.8% and 0.6% for DRIVE and CHASE, respectively. Despite this minimal reduction in loss, our model required 4.5 times less number of floating point operations and 2.5 times less number of parameters.

Quick and automatic detection of blood vessels and optic disc can help with the diagnosis for diabetic retinopathy and Glaucoma from retinal fundus images when resources are limited. As diabetic retinopathy causes the shrinkage of retinal blood, through automatic segmentation of the blood vessels, we have an objective means to track identify the presence and progression of diabetic retinopathy. For Glaucoma, in addition to the segmentation of optical disc, we also need segmentation of the optic cup. In our future work, as labelled data becomes available, we intend to extent the work to test the model's performance in segmentation of optic cup and measure Glaucoma.

While our model accurately detects major vessels, it still fails to detect tiny vessels (evident in sample images in Figure B.3) from the fundus images. As the images in the DRIVE dataset had more fine and tiny vessels compared to the CHASE dataset, the accuracy is higher in CHASE compared to DRIVE. This is a limitation of our

model that needs to be addressed in future work.

Appendix C

Mobile-RetinaNet : A Computationally Efficient DeepNet for Retinal Fundus Image Segmentation for Use in Low-resource Settings

Authors: *Ranit Karmakar, Saeid Nooshabadi, Allen Eghrari* [1]

[1]Karmakar, R., Nooshabadi, S. and Eghrari, A., 2022. Mobile-RetinaNet : A Computationally Efficient DeepNet for Retinal Fundus Image Segmentation for Use in Low-resource Settings. Invest. Ophthalmol. Vis. Sci.;63(7):2064 – F0053.

C.1 Abstract

C.1.1 Purpose:

Retinal fundus photography is used by physicians to detect and track different eye diseases such as glaucoma and diabetic retinopathy (DR). Manual segmentation is time-consuming and may introduce observational bias. This work presents a computer-aided automatic segmentation model for the retinal blood vessels and optic disc in retinal fundus images. Accurate automatic detection of these image features will reduce the manual effort while producing consistent results in clinical settings instantaneously.

C.1.2 Methods:

The efficient use of bottleneck residual blocks on the U-Net like encoder-decoder convolutional neural network (CNN) architecture requires a significantly lesser number of floating-point operations (FLOPs) to achieve the desired accuracy. The model has been trained and tested on two publicly available retinal datasets, digital retinal images for vessel extraction (DRIVE) and child heart and health study in England (CHASE). The model's performance is compared with the prior art using widely used

accuracy, sensitivity, specificity, and the area under the curve (AUC). For the OD segmentation, we proposed a fully automatic segmentation that uses classical image processing to localize the OD and then our network to do the semantic segmentation.

C.1.3 Results:

For retinal vessel segmentation, we achieved an AUC score of 0.968 for the DRIVE dataset and 0.985 for the CHASE dataset which for the state-of-the-art is 0.986 and 0.991 respectively. With this small degradation in performance, our model needs 2.5 times a lesser number of parameters and 4.5 times fewer FLOPs. For OD segmentation, we achieved an AUC score of 0.950 and 0.981 for the DRIVE and CHASE datasets respectively.

C.1.4 Conclusions:

While deep learning models can be high resource-consuming, successfully developed a model that achieves very high efficiency for medical image segmentation task without loosing much accuracy.

Appendix D

Understanding the effects of medical conditions on the corneal endothelial cell density using eye bank data

Authors: *Ranit Karmakar, Saeid Nooshabadi, Allen Eghrari* [1]

[1]Presented as a poster at World Cornea Congress VIII

D.1 Abstract

D.1.1 Purpose:

In eye banking, measuring the quality of the corneal endothelial tissue is important for transplant. This measurement is performed using specular microscopes. Alongside the image analysis, the donor's medical history was also looked at. In this study, we assessed the association of different medical conditions with the health of corneal endothelium.

D.1.2 Methods:

We have used the data from 10,322 eyes from a total of 5,624 unique donors collected over 5 years at an eye bank. All the images underwent imaging with a Konan CellChek D specular microscope and then analyzed using standard methods by certified technicians to measure the cell density, hexagonality, and coefficient variance. The donor's medical history and demographic information were associated with each tissue. Using this data, we used multivariate regression to assess the association of different medical conditions with corneal health.

D.1.3 Results:

Our analysis showed while measured together, alcohol abuse, tobacco abuse, diabetes, hypertension, and anemia had a negative effect on the corneal endothelial cell density. Depression, sleep apnea, post-traumatic stress disorder, and obesity did not have any effect. While measured in individual models, the same effects were noticed.

D.1.4 Conclusions:

This study helps to identify the effects of common medical conditions on the health of corneal endothelial cell density.

Appendix E

Effects of Systemic Medical Conditions and Previous Cataract Surgery on Corneal Endothelium Density– A Big Data Analysis

Authors: *Ranit Karmakar, John B. Lohmeier, Staci L. Terrin, Elizabeth Fout, William B. Buras Sr., Saeid Nooshabadi, Allen O Eghrari, Ellen H. Koo* [1]

[1]Accepted as an oral presentation at American Society of Cataract and Refractive Surgery (ASCRS) 2023 Annual Meeting

E.1 Abstract

E.1.1 Purpose:

To elucidate the effects of diabetes mellitus, hypertension, alcohol and drug abuse, as well as previous cataract surgery on the corneal endothelium density.

E.1.2 Methods:

Data from 2 eye banks were obtained. Quantitative and qualitative analysis of donor corneal endothelium was performed manually using the Konan CellChek D specular microscope. Donors' medical history was reviewed for the presence of diabetes, hypertension, alcohol and drug abuse (specifically, methamphetamine and cocaine), as well as history of previous cataract surgery, to elucidate their effects on the health of the corneal endothelium. Multivariate regression analysis was used to determine the association between these factors and corneal endothelial cell density. All the models were adjusted with respect to age and pseudophakia.

E.1.3 Results:

Donors' history of diabetes mellitus and hypertension were not associated with negative effects on the endothelial cell density (ECD), with respective p-values of 0.231 and 0.352. Donors with a history of cocaine and methamphetamine abuse had on average 54 fewer cells per mm^2 with a p-value 0.018. Donors with alcohol abuse history, the endothelial cell density was lower by 61 cells with a p-value < 0.0001. Donors with previous cataract surgery had on average 89 fewer cells per mm^2 with a p-value of < 0.0001.

E.1.4 Conclusions:

This study helps to identify the effects of common medical conditions on the health of corneal endothelial cell density.

Appendix F

An Analysis of Demographic and Medical Information of Eye Bank Donors: Utilizing Big Data from the Florida Lions Eye Bank

Authors: *Ranit Karmakar, Elizabeth Fout, William Buras, Allen Eghrari, Ellen Koo*

[1]

[1]Submitted as an Abstract at Eye Bank Association of America (EBAA) 2023 Annual Meeting

F.1 Abstract

F.1.1 Purpose:

The purpose of this study is to analyze the demographic and medical characteristics of eye bank donors at the Florida Lions Eye Bank using big data techniques, with the aim of improving eye donation and transplantation outcomes.

F.1.2 Methods:

This study utilized big data from the Florida Lions Eye Bank, which included demographic data such as age, gender, and race, as well as medical data such as cause of death, medical history, and tissue suitability. Descriptive statistics were used to summarize the data, while inferential statistics were used to identify any significant relationships between the variables.

F.1.3 Results:

A total of 7,168 donor records from January 2015 to December 2022 were analyzed. The results revealed that 67% of the donors were male, while only 33% were female. The average age of the donors at the time of death was 59 years. We also observed that EtOH abuse had a negative effect on the endothelial cell density.

F.1.4 Conclusions:

This study provides important insights into the characteristics of eye bank donors, which can inform the development of strategies to improve donor outreach and tissue screening processes. Our findings suggest that the proportion of male donors in eye donation is higher than in organ donation, which warrants further investigation. The study emphasizes the need for increased public awareness and education about the benefits of eye donation.